UNIVERSITY OF CALIFORNIA,
IRVINE

Investigation of gamma-crystallin biophysical properties and aggregation pathways relevant to cataract formation

DISSERTATION

submitted in partial satisfaction of the requirements
for the degree of

DOCTOR OF PHILOSOPHY

in Chemistry

by

Kyle Roskamp

Dissertation Committee:
Professor Rachel W. Martin, Chair
Professor Gregory A. Weiss
Professor Douglas J. Tobias
Professor Carter T. Butts

2019

DEDICATION

To mom and dad, for nurturing my intellectual curiosity.

TABLE OF CONTENTS

LIST OF FIGURES

LIST OF TABLES

ACKNOWLEDGMENTS

Graduate research is seldom an individual pursuit. There are numerous people, from the professors to the department staff to the custodial teams, that are necessary in for graduate students to develop as scientists. I am especially grateful that the UCI chemistry department has been composed of individuals ready and willing to help in any way they can. I would like to thank some of the people who have helped me the most throughout my time at UCI.

Rachel Martin – for allowing me to pursue the projects that I found interesting, enabling me to work with collaborators across the globe, and helping me through the graduate school process wherever necessary.

Carter Butts – for helping me think critically about research problems, allowing me to explore computational research projects, and for continual research support.

Dmitry Fishman – for the many hours spent helping me in the laser lab and you advising on countless occasions.

Domarin Khago – for your mentorship, the conversations about anything but science, and for making the lab a enjoyable place to work.

Jan Bierma – for teaching me most of what I know about molecular biology, the all too rare conversations about the progress of our science, and general scientific guidance.

Marc and Brenna – for your constant positivity, being great lab mates to work with, and taking on all of my projects after I have gone.

Christian and Ashley – for being the best undergraduates researchers a graduate student could hope for.

Mackenzie Turvey – for making the daily grind bearable, your enthusiasm for life, and constant entertainment in and outside of lab.

Paige Lin – for being my rock during the hard times, the cause of so many good times, and my biggest supporter all of the time.

Karl, Sean, Brian, and Claudette – for everything.

The research presented herein was supported by National Institutes of Health Grants 1R01-EY021514 and 1R01-EY025328, and National Science Foundation Grants DMR-1410415, DMS-1361425, and DGE-1633631. Thank you to labs of Gregory Weiss, Jennifer Prescher, James Nowick, Andrej Luptak, Joe Patterson, Elizabeth Jarvo, Stephen White, Celia Goulding, Kenneth Shea, Alan Heyduk, Chang Liu, Thomas Poulos, R. J. Dwayne Miller, Martin Weik, Songi Han, Andor Kiss, and Liliana Quintanar for your time and access to instruments and resources.

CURRICULUM VITAE

Kyle Roskamp

EDUCATION

Doctor of Philosophy in Chemistry **2019**
University of California, Irvine *Irvine, CA*

Bachelor of Arts in Chemistry, Mathematics **2014**
Pomona College *Claremont, CA*

RESEARCH EXPERIENCE

Graduate Research Assistant **2014–2019**
University of California, Irvine *Irvine, CA*

Undergraduate Research Assistant **2014–2019**
Pomona College *Claremont, CA*

TEACHING EXPERIENCE

Teaching Assistant **2014–2017**
University of California, Irvine *Irvine, CA*

REFEREED JOURNAL PUBLICATIONS

Bierma, J.C., **Roskamp, K.W.**, Ledray, A., and Martin, R.W. "Controlling liquid-liquid phase separation in cold-adapted crystallin protein from the antarctic toothfish" *Journal of Molecular Biology* 430, no. 24 (2018): 5151.

Khago, D., Bierma, J.C., **Roskamp, K.W.**, Kozlyuk, N., and Martin, R.W. "Protein refractive index increment is determined by conformation as well as composition" *Journal of Physics Condensed Matter* 30, no. 43 (2018): 435101.

Roskamp, K.W., Montelongo, D.M., Anorma, C., Bandak, D., Chua, J., Malecha, K.T., and Martin, R.W. "Multiple aggregation pathways in human γS-crystallin and its aggregation-prone G18V variant." *Investigative Ophthalmology & Visual Science* 58, no. 4 (2017): 2397-2405.

Kim, J.K., Liu, J., Hu, X., Yu, C., **Roskamp, K.W.**, Sankaran, B., Huang, L., Komives, E.A., and Qiao, F. "Structural basis for shelterin bridge assembly." *Molecular Cell* 68, no. 4 (2017): 698-714.

Butts, C.T., Zhang, X., Kelly, J.E., **Roskamp, K.W.**, Unhelkar, M.H., Freites, J.A., Tahir, S., and Martin, R.W. "Sequence comparison, molecular modeling, and network analysis predict structural diversity in cysteine proteases from the Cape sundew, Drosera capensis." *Computational and Structural Biotechnology Journal* 14 (2016): 271-282.

Huang, K., Kingsley, C.N., Sheil, R., Cheng, C., Bierma, J.C., **Roskamp, K.W.**, Khago, D., Martin, R.W., and Han, S. "Stability of protein-specific hydration shell on crowding." *Journal of the American Chemical Society* 138, no. 16 (2016): 5392-5402.

ABSTRACT OF THE DISSERTATION

Investigation of gamma-crystallin biophysical properties and aggregation pathways relevant to cataract formation

By

Kyle Roskamp

Doctor of Philosophy in Chemistry

University of California, Irvine, 2019

Professor Rachel W. Martin, Chair

This thesis examines the biophysical properties of $\beta\gamma$-crystallin proteins with a specific focus on how exogenous factors such as UV and divalent cations drive the aggregation of eye lens γS-crystallin. $\beta\gamma$-crystallin superfamily proteins are found in archaeal, bacterial, and eukaryotic species, with varying functionalities that represent evolutionary adaptation. In this work the eye lens γS-crystallin is shown to have orthogonal behavior to *Ciona intestinalis* $\beta\gamma$-crystallin (Ci-$\beta\gamma$) – a Ca^{2+} binding protein – in the presence of various divalent cations. Ci-$\beta\gamma$ coordinates divalent cations at the same site, increasing its thermal stability, whereas cystine coordination to some transition metal divalent cations induces aggregation in γS-crystallin. Unlike other transitional metals, Cu^{2+} induced aggregation of γS is buffered by the presence of free, solvent accessible cysteines. Cu^{2+}-driven aggregation differs from other underlying causes such as UV or missense point mutations and may be attributed to a combination of different factors. Notably, Cu^{2+} is able to catalyze intermolecular disulfide bond formation as well as facilitate radical crosslinking. Reductions in β-sheet content also occur in aggregated species, further suggesting that hydrophobic interactions may drive aggregation. Another physiologically relevant underlying mechanism, UV radiation, was used to induced aggregates for comparative measurements with acid-induced fibrils that exhibit amyloid character. The two groups are distinct in their biophysical characterization. High

levels of turbidity but low thioflavin T binding for UV-induced aggregates while acid-induced fibrils exhibit the opposite characteristics. In both cases, it is notable that mutations compromising stability exacerbate the observable characterization. These results suggest that γ-crystallin aggregates resulting from accumulated UV exposure are unlikely to contain fibrillar character.

Chapter 1

Introduction

1.1 The Lens Crystallins

1.1.1 Lens Development and Function

The lens is a transparent organ that aides in the refraction of light onto the retina. The development of the vertebrate lens occurs through the maturation of surface ectoderm cells into lens progenitor cells. The resulting embryonic structures defines the morphological structure by folding back onto itself to form a cavity, forming the lens vesicle.[1, 2] The cells at the anterior of the vesicle develop into lens epithelial cells while the cells at the posterior cells develop into primary lens fiber cells. In the final stage of development, secondary lens fiber cells are formed through terminal differentiation of the lens epithelial cells. As the forming secondary lens fiber cells develop from the epithelial cells at the sides of the lens, the primary lens fiber cells are encapsulated as the lens nucleus. During their differentiation, fiber cells elongate and enucleate. The resulting mature fiber cells are void of sub-cellular organelles, including the nucleus, and contain exceptional levels of crystallin protein. Nearly

90% of the dry weight of the human lens is composed of these crystallins, although the expression level of different crystallins are regulated in a spatiotemporal manner during the maturation of the lens.[3, 4]

The differential expression of crystallins in lens fiber cells creates a gradient of refractive power across the lens. In the vertebrate lens, this gradient – in conjunction with changes in the lens shape due to the ciliary muscles attached to the top and bottom – enable changes in optical depth-of-focus. Despite their consistent exposure to light, lens fiber cells generated during and after development are never replaced and must function over an organism's lifetime. Similarly, the degradation of cellular machinery during development means that lens proteins must remain functional, as protein turnover is negligible. For the lens crystallins, their function to focus light onto the retina is seemingly risky, as photo-induced damage is irreversible given their necessary longevity.

1.1.2 α-crystallins

The α-crystallins are one of the two families of crystallin proteins found in the lens and compose roughly 40 % of human lens protein.[5] Two different α-crystallin proteins exist, αA and αB. In the lens, the αA:αB ratio is roughly 3:1. α-crystallins are also found in the heart, brain, and kidney where they function as holdase chaperones[6]. The two proteins are highly similar in sequence (54 % identity for human αA and αB via SIM[7]) and structure, and both contain $\sim$175 residues with a molecular weight of $\sim$20 kDa. Structurally, α-crystallins are composed of primarily unstructured N- and C-terminal domains with a 90-residue immunoglobulin-like "α-crystallin domain" in the middle. Monomers come together to form hetero- and homo-dimers, which serve as the building blocks for high molecular weight complexes ranging up to 48-mers, with mean sizes of 24-mers[8, 9].

Unlike other heat shock family proteins, the molecular mechanism enabling substrate recog-

nition for α-crystallins and heat shock family 20 (Hsp20) members is poorly understood. In general, exposed hydrophobic surface of the client proteins is thought to enable a binding interaction. The exact binding sequence from the α-crystallins and the oligomerization state enabling binding, have not been definitively proven. Attempts to identify this site has shown that residues in the α-crystallin core of the protein interact with hydrophobic polypeptides including melittin[10] and insulin B chain[11]. Subsequent analysis and characterization of these peptide sequences – named mini-αA/B crystallin (MαAC/MαBC) – *in vitro* has shown that they retain chaperone activity[**?**].

1.1.3 $\beta\gamma$-crystallins

The lens β- and γ-crystallins are structurally homologous proteins that belong to the $\beta\gamma$-crystallin superfamily. Members of this family contain a domain composed of a double Greek key motif. The resulting β-sandwich contains two sheets of four antiparallel strands, packing hydrophobic residues internally. Superfamily members contain at least one such "$\beta\gamma$-crystallin domain", with the lens β- and γ-crystallins containing two. Independent of other structural features, many $\beta\gamma$-crystallins are observed to be calcium-binding proteins.

The capacity of a $\beta\gamma$-crystallin for calcium-binding can be readily assessed by the two loop sequences that link the third and fourth strand of each Greek key. A conserved (N/D)-(N/D)-x-x-(T/S)-S sequence is conserved in each of the two loops in calcium-binding $\beta\gamma$-crystallins, whereas only the final serine is strictly conserved otherwise. In the lens β- and γ-crystallins positively charged residues are often found at the other positions. A conserved feature of the $\beta\gamma$-crystallin superfamily is a (F/Y/W)-x-x-x-x-(F/Y)-x-G sequence found across the first β-hairpin of each Greek key. The aromatics of this motif participate in π-stacking interactions, while the glycine is capable of adopting unconventional backbone torsional angles.

1.1.4 Lens β-crystallins

The lens β- and γ-crystallins are each composed of several different protein species. β-crystallins are subdivided by their net charge; four are acidic β-crystallins (βA1, βA2, βA3, and βA4), and three are basic β-crystallins (βB1, βB2, and βB3)[12]. In one case, βA1 and βA3, the proteins are isoforms with differing N-terminal extension lengths[13]. The extensions, unstructured sequences at the N- and C-termini with varying lengths up to 65 residues, play an important role in oligomerization.[14] These, in addition to sufficiently long interdomain linker sequences, enable the β-crystallins to form domain-swapped dimers. β-crystallin dimers coordinate into oligomers up to 200 kDa,[15, 12] assays, supporting the idea that the monomeric species are less energetically favorable. Both hetero- and homo-oligomeric species have been observed using recombinantly expressed β-crystallins and are assumed to be present *in vivo*.[16, 17]

1.1.5 Lens γ-crystallins

In contrast to the lens β-crystallins, the γ-crystallins are natively monomeric. The eight γ-crystallin genes (γA, γB, γC, γD, γE, γF, γS, and γN) are conserved in most mammals, although γE, γF, and γN are often unexpressed pseudogenes[18]. The interdomain linker sequences of the γ-crystallins are shorter than their β-crystallin cousins, and likewise lack N- and C-terminal extensions. The exceptions are the γS and γN-crystallins. While not expressed in the human lens, γN has been observed in the brain[19] and lenses[20] of rodents. It is the most divergent of the γ-crystallins, as evidenced by its hybrid β- and γ-crystallin gene structure and low sequence identity and is thought to represent an evolutionary hybrid between the lens β- and γ-crystallin families.

The other exception in the γ-crystallin family is γS. γS-crystallins are highly conserved across and contains an extra four N-terminal and two interdomain linker residues with two

fewer C-terminal residues. While the exact function of the short N-terminal tail is unknown, the increased linker length is considered significant as γS is the only γ-crystallin that has been shown to capable of forming domain-swapped dimers. Of the highly expressed lens γ-crystallins, only γS is cortical while γC and γD are found in the lens nucleus. The function of the γ-crystallins as highly soluble, long-lived, monomeric structural proteins has made them idea subjects for investigating the molecular mechanisms underlying cataract formation. In the research presented here, γS-crystallin has been examined extensively.

1.2 Biophysical Properties of γ-crystallins

1.2.1 Stability *in vivo*

The timescale of protein turnover is variable, with half-life times as short as minutes for ornithine decarboxylase[21] or up to a month for some immunoglobulins[22]. The need for the lens crystallins to function over an organism's lifetime without replacement places them in a unique class known as extremely long-lived proteins (ELLPs). Well known members of this class are the structural proteins of the extracellular matrix, collagen and elastin, that form a crosslinked polymeric structure.[23] Others, such as the scaffold proteins of the nuclear pore complex, exist within massive cellular machinery structures. Unlike other ELLPs, the lens α- and β-crystallin oligomers are minuscule, while the γ-crystallins are idiosyncratic due to their monomeric nature.

As monomers, the intermolecular interactions of the γ-crystallins are likely imperative to their structural stability. Hydrophobic residues are almost exclusively packed into the core of the β-sandwich in each domain and at the interdomain interface. Externally, the γ-crystallin surface a patchwork of acidic, basic, and neutrally charged residues that form a highly interconnected network of hydrogen bonds and salt-bridges. Interspersed internally

and externally are pairs and collections of aromatic residues that form π-π-stacking interactions. Systematic removal of these residues has shown that each contributes to protein stability, however, modifications of N-terminal residues result in greater destabilization.[24] This observation, that the N-terminal domain of the γ-crystallins is less stable – and often unfolds under extreme conditions – is consistent with the observation 30/35 known cataractous point mutations in human and mice are found in the N-terminal domain (Appendix A: Table A1, Figure A1).

1.2.2 Fluorescence Quenching and Intradomain Förster Resonance Energy Transfer (FRET)

An omnipresent feature of lens β- and γ-crystallins, but one considerably less conserved in non-lens $\beta\gamma$-crystallins, is a pair of buried tryptophans in each domain. These residues function as a FRET pair and help to quench fluorescence. In vertebrate γ-crystallins, these four tryptophans are remarkably conserved and almost always the only tryptophans, whereas β-crystallins contain additional solvent-exposed tryptophans. The ability of these pairs to quench fluorescence and the location of the β- and γ-crystallins in the lens suggests that these lens proteins have been evolved to act as a sort of photo-protectant.

Extensive fluorescence characterization by the lab of Jonathan King has shown that intradomain FRET occurs between the donor tryptophan of the first Greek key and the acceptor tryptophan of the second Greek key[25], with no interdomain FRET[26]. The conserved structure surrounding the buried donor tryptophan is thought to help enable the ultrafast quenching. Analysis of known crystal structures suggests two water molecules are proximal for hydrogen bonding to the indole ring and backbone of the tryptophan. Further, the face of the tryptophan ring is adjacent to the n - 3 residue backbone carbonyl with the tryptophan CG always $\sim$3.5 Å from the carbonyl oxygen. This arrangement is proposed to stabilize

charge transfer events to enable excited state quenching, as similar mechanisms have been proposed for other systems[27].

1.2.3 Refractive Index Increment (dn/dc)

The refractive index is defined as the ratio of the velocity of light in a vacuum to its velocity in a given isotropic medium. When entering a new material, the extent to which light is bent is a function of the refractive index and can be readily determined using Snell's Law. The lens, which aids in focusing incident light onto the retina, contains a radial gradient of refraction that is attributable to the concentration and content of the corresponding fiber cells. The crystallin proteins of the lens are therefore suspected to have be evolved to further increase the refractive power of the lens.

The change in refractive index with concentration for solute is known as the refractive index increment (dn/dc). Conventionally, a value of 0.185 is used for proteins in spectroscopic measurements for convenience, as few proteins have measured dn/dc values in any solvent. Predictions of protein dn/dc based solely on primary sequence indicate that the γ-crystallins are far more refractive ($\sim$0.199)[28] than the proteomic mean (0.1899 ± 0.003)[29]. These values are in line with the observed values for extracted lens crystallins which show the γ-crystallins are the most refractive, followed β-crystallins and finally α-crystallins[30]. Experimental dc/dc measurements of recombinant γ-crystallins evidence that strictly sequence based models underestimate total protein refractivity. More accurate predictions of protein dn/dc are observed by accounting for the number, distance, and type of aromatic interactions in protein structure[31]; however, the further research is required to fully understand all factors governing protein refractivity.

1.3 Aggregation Pathways of γ-crystallins

The advent of recombinant protein expression has dramatically shifted the investigation of lens protein aggregation from extracted homogenates to individual, highly purified lens proteins. An array of mechanisms leading to aggregation have been proposed, with evidence supporting each. Given the various phenotypes of cataract, genetic and environmental factors, and complexity of the lens fiber cell protein makeup, it is likely that cataract can occur through a variety of pathways. Due to the intrinsically stable nature of the lens proteins, many studies of protein destabilization leading to cataract have been conducted using confirmed cataractous point mutants. While these systems have provided insight into possible avenues to protein aggregation, an array of other pathways are also possible.

1.3.1 Fibrillization

Fibrillar aggregates are observed in diseases such as Alzheimer's, Huntington's and Parkinson's disease, and have become a source of significant research interest. In particular, the amyloid fibrils characterized by cross-β structures with spacings of 4.7 Å and 10 Å are insoluble, contain some heterogeneity, and can be formed from a range of proteins. These assemblies form long, unbranched chains that represent a seemingly irreversibly low energy state of protein folding. Experimentally, however, limited evidence supports the hypothesis that lens aggregates are fibrillar. While 2-dimensional infrared spectroscopy of whole lenses show cross-sectional peaks similar to those observed from amyloid fibrils[32], searches for insoluble amyloids have been unsuccessful. α-, β-, and γ-crystallins have been shown to form fibrils *in vitro* under highly acidic conditions at elevated temperatures; however, biophysical characterizations have evidenced that they bear little resemblance to aggregates formed through ultraviolet (UV) damage and other physiologically relevant pathways[33].

1.3.2 Unfolding and Domain Swapping

Comparisons of the N- and C-terminal domains of γ-crystallins have shown that when expressed individually, the N-terminal domain (NTD) is more susceptible to chemical and thermal denaturation than the C-terminal domain (CTD). Numerous γ-crystallin point mutants also exhibit three state unfolding, with mutations in the NTD suspected to increase its unfolding susceptibility. Similarly, the accumulation of PTMs has been proposed to sufficiently destabilize the NTD. PTM's of tryptophan of are particular interest due to their location in the hydrophobic core; oxidation of tryptophan may facilitate unfolding from the inside of the protein. Exactly how unfolding may initiate aggregation is unknown. Transient structures of partially unfolded protein may become more frequent with PTMs or other exogenous factors that shift structural equilibrium. In this case, the probability of aggregation through intermolecular hydrophobic interactions increases as accumulated PTMs reduce protein stability.

Domain swapping is another type of structural change that may occur to γ-crystallins. In this event, the N-terminal of one protein associates with the C-terminal of another protein using the residues that normally contribute to intramolecular interdomain interactions. PTMs near the interdomain interface have been proposed to result in a dissociation of the two domains by reducing the specific stabilizing interactions. This phenomenon is a well-characterized feature of β-crystallins – resulting in hetero- and homo-dimer formation – but unobserved in γ-crystallins. Recent work has shown domain swapping is possible for γS-crystallin, the γ-crystallin with the longest interdomain linker. For γS, domain swapping is proposed to be catalyzed by a combination of intramolecular and intermolecular disulfide formation. As outlined by Serebryany et. al.[34], domain swapping may play a role in initiating a daisy chain-like polymerization, which may become exacerbated though interactions with damaged proteins capable of unfolding.

1.3.3 Bridging and Cross-linking

The high density and monomeric nature of the γ-crystallins in the lens has led to investigations of short range ordering interactions that may aid in their longevity. The water surrounding γ-crystallins is dynamic and remains largely unchanged at high concentrations. In contrast, the hydration layer of γS-crystallin G18V is highly susceptible to concentration, particularly when approaching physiological conditions in excess of 100 mg/mL.[35] Beyond differences in structure, covalent crosslinking post-translational modifications are another mechanism that may facilitate destabilizing interactions, and are observed to result from UV exposure.[36] Disulfide bonds have garnered the most addition as potentially deleterious cross-linkings, as no native disulfides are observed in the γ-crystallins. Prominently, intermolecular disulfides have been observed in the formation of domain-swapped γS-crystallin dimers while intra-molecular disulfides have been shown to trap non-native confirmations. Other crosslinkings are possible through dityrosines formed though UV or ROS mediated pathways and lysine glycation[37]. More recently, transition metals have been observed induce aggregation of lens γ-crystallins. Assayed metals include zinc, copper, and mercury, with some to all of the intermolecular bridging being reversible through metal chelation.[38, 39]

1.3.4 Protein Condensation

In addition to the aforementioned mechanisms, protein insolubilization and aggregation are possible though alternative pathways that may be relevant to cataract. The common method of ammonium sulfate precipitation is one example, where water becomes exuded from the protein's surface in the presence of excess salt until the solubility is compromised. In this case, the protein structure is often uncompromised, an observation similarly observed in the solid-state NMR (ssNMR) of aggregates from γD-P23T.[40] High levels of light scattering without

structural changes also occur in cold-cataract. Following a sufficient drop in temperature, protein solutions become opaque and separate into high and low density phases – a process known as liquid-liquid phase separation (LLPS). This separation is reversible upon warming, and the temperature at which LLPS occurs for a protein has been shown to be dependent on the specific charged residues located on the proteins surface.[41] The unifying feature of these methods, an absence of structural changes, suggests that the surface network of the γ-crystallins is equally as important in regulating solubility as any other biophysical characteristic.

Chapter 2

Divalent cations and the divergence of $\beta\gamma$-crystallin function

2.1 Introduction

The vertebrate β- and γ-crystallins are structural proteins that make up the refractive tissue of the eye lens, where they compose up to 50% of the dry weight. Their extraordinary solubility enables them to pack at concentrations of more than 350 mg/mL in the lenses of humans and 750 mg/mL in those of fish. These strongly conserved proteins contain two or more $\beta\gamma$-crystallin domains, a β-sandwich structure comprising two sequential Greek key motifs, and are thought to share a common ancestor with the Ca^{2+}-binding $\beta\gamma$-crystallins found in microbes and invertebrates. Microbial $\beta\gamma$-crystallins contain a characteristic double clamp Ca^{2+}-binding motif in which the loops situated atop the protein contribute binding residues to both sites. The idea that vertebrate lens crystallins evolved from calcium-binding $\beta\gamma$-crystallins, based on structural homology, is well attested in the literature on lens protein evolution.[42, 43] The *Ci*-$\beta\gamma$ crystallin from the tunicate *Ciona intestinalis* appears to

bridge both crystallin functions: it is expressed in the papillae as well as the sensory vesicle, a structure found in ascidians that contains the gravity-sensing otolith and the light-sensitive ocellus.[44] A tunicate begins life as a free-swimming larva resembling a tadpole. During this larval stage, the animal navigates its environment using sensory inputs from the otolith and the ocellus.[45] Once it reaches the appropriate developmental stage, the tunicate attaches to a suitable substrate location via an adhesive secreted by the papillae.[46] The expression of *Ci*-$\beta\gamma$ in both of these organs (and nowhere else) [47] underscores the significance of its dual role, representing a transition between the microbial calcium-binding crystallins and the vertebrate lens crystallins. *Ci*-$\beta\gamma$ contains two functional double clamp Ca^{2+}-binding sites and is also more highly refractive than its amino acid composition alone would suggest (although to a lesser extent than vertebrate lens proteins),[31] further suggesting dual functionality.

Despite their similar ancestry [48, 3], many of the vertebrate $\beta\gamma$-crystallins appear to have eschewed calcium binding activity [49], possibly as a result of their evolution to the more stable two domain structures, or simply through genetic drift.[50] Some reports have suggested that the lens β- and γ-crystallins weakly interact with calcium;[51, 52] however, NMR chemical shift perturbation suggests no structural changes upon addition of Ca^{2+} for human γS-crystallin.[53] Moonlighting is seemingly omnipresent for vertebrate taxon-specific crystallins, including δ- (argininosuccinate lyase) [54], ϵ- (lactate dehydrogenase) [55], ζ- (quinone reductase) [56], λ- (3-hydroxyacyl-CoA dehydrogenase) [57], and τ- (α-enolase) [58], as a variety of small, soluble proteins were recruited to the lens via gene duplication, raising the possibility that the ubiquitous vertebrate $\beta\gamma$-crystallins may have also retained cation-binding functionality.

The interactions of $\beta\gamma$-crystallins with divalent cations have important implications for lens homeostasis and cataractogenesis. For example, copper and zinc ions increase the chaperone activity of the lens α-crystallins, but become displaced upon substrate binding [59].

Incubation of free zinc and copper with γD-crystallin results in the formation of light scattering aggregates,[39, 60] thus a positive feedback cycle could exacerbate cataract fromation. Moreover, elemental analysis of cataract and diabetic lenses has shown that elevated levels of copper are present [61, 62]. Likewise, elevated levels of cadmium, iron, zinc and other metals have been reported in cataract by several groups.[63, 64, 65] Increased metal ion concentration in the lens could promote γ-crystallin aggregation directly [38] or indirectly through the displacement of copper from α-crystallins. In prion and other protein aggregation diseases, the displacement of copper alters protein-protein interactions and inhibits protein function.[66]

In contrast to the vertebrate γ-crystallins, which appear not to have significant cation interactions in the healthy lens, the cation-binding $\beta\gamma$-crystallins such as M-crystallin [67], clostrillin [68], rhodollin [68], spherulin [69], and protein S [70] exhibit dramatically increased thermal and chemical stability in the presence of calcium ions. These changes are often concomitant with binding-induced structural changes. The $\beta\gamma$-crystallin from *Ciona intestinalis* (*Ci*-$\beta\gamma$), is primarily found in the calcium carbonate-rich matrix of the otolith located above the photoreceptive ocellus. In addition to its location in a lens-like organ, the *Ci*-$\beta\gamma$-crystallin gene promoter is functional in transgenic vertebrate assays, suggesting that it is a close homolog of the lens $\beta\gamma$-crystallins [71]. Unlike many other cation-binding $\beta\gamma$-crystallin domains, which are found within a higher molecular weight protein, *Ci*-$\beta\gamma$ has only a single domain. For these reasons, *Ci*-$\beta\gamma$ is an ideal candidate for investigating stability differences between the lens γ-crystallins and cation-binding $\beta\gamma$-crystallins.

In the Ca^{2+}-binding EF-hand motif of calmodulin [72] and ion channels [73, 74], other divalent cations may compete with Ca^{2+} at its binding site. In fish otolith and lenses, environmentally common cations such as Sr^{2+} and Fe^{2+} are present in addition to trace metals including Mn^{2+}, Co^{2+}, and Pb^{2+}[75]. The effect of non-calcium cation binding on these proteins' structure and stability, however, remains incompletely characterized. Simi-

larly, limited research has been conducted on the effect of non-oxidizing cations on lens $\beta\gamma$-crystallin interactions and stability. Understanding the similarities and differences between these crystallin subgroups beyond their overall structural fold is paramount to understanding the evolutionary development of lens protein stability. Moreover, a comparative analysis is also necessary for elucidating how exogenous factors influence $\beta\gamma$-crystallin behavior and to characterize the functional range of the crystallin double-clamp binding motif. In order to address these questions, we have investigated the effect of the divalent cations of magnesium, calcium, strontium, manganese, cobalt, nickel, zinc, and copper on the stability of human γS-crystallin (HγS) and *Ciona intestinalis* $\beta\gamma$-crystallin (*Ci*-$\beta\gamma$). We have also performed structural and sequence analysis of lens and cation-binding $\beta\gamma$-crystallins to place these experimental observations in an evolutionary context.

2.2 Materials and methods

2.2.1 Amino acid composition analysis

The DNA sequences of lens γ-crystallins were collected from NCBI (https://www.ncbi.nlm.nih.gov/protein) searches using the keywords "gamma crystallin", "beta crystallin S", "beta gamma crystallin", "betagamma crystallin" and filtered for 'Animals' and sequences between 170 and 185 residues. Low-quality, crystallin-like, homolog, related, point mutant, partial, and incomplete sequences were removed by manual review of each entry. Leading methionine residues were removed from applicable sequences. To avoid overweighting, only one paralog of polymorphic γ-crystallins was used in the final data set. To maintain similarity to the experimentally characterized human γS-crystallin, only γ-crystallin sequences from terrestrial vertebrates were analyzed. The final data set was composed of 50 γA-, 78 γB-, 62 γC-, 55 γD- and 62 γS-crystallins. Additionally, the DNA sequences corresponding to the 7 $\beta\gamma$-

crystallin proteins for which PDB structures confirm cation-binding coordination through the double clamp binding motif (PDBID: 1HDF [76], PDBID: 1NPS [70], PDBID: 2BV2 [47], PDBID: 3HZB [68], PDBID: 3HZ2 [68], PDBID: 3I9H [68], and PDBID: 4IAU [77]) were collected from the NCBI database. γE-, γF-, and γN-crystallins were excluded from this study because they are either not expressed or are pseudogenes in humans.

2.2.2 Sequence alignments and selection analysis

The alignments for all DNA and protein sequences were generated using MEGA7 [78]. Protein sequences were aligned using MUSCLE with default gap penalties and the UPGMB clustering matrix.[79] Trees for each alignment were then constructed from the DNA of the aligned protein sequences using the neighbor-joining method. Preliminary dN/dS calculations for selection at each codon were subsequently calculated using Felsenstein 1981 (F1981), General Time Reversible (GTR), Hasegawa-Kishino-Yano (HKY), and Tamura-Nei (TN) methods from MEGA7. Further codon selection analysis was also calculated using the Single-Likelihood Ancestor Counting (SLAC) and Fixed Effects Likelihood (FEL) methods using the program HyPhy, [80] which produced identical results.

2.2.3 Solvent-exposed surface area

The side chain solvent-accessible surface area (SASA) for cysteine residues was calculated using VADAR (http://vadar.wishartlab.com/)[81]. Structures from the Protein Data Bank were used for γB (PDBID: 2JDF [82]), γC (PDBID: 2NBR [83]), γD (PDBID: 1HK0 [84]), and γS (PDBID: 2M3T[85]), whereas an ITASSER model [86] was generated for γA, for which no experimental structure was available.

2.2.4 Protein Expression and Purification

Expression and purification of natural abundance and uniformly ^{15}N-labeled tunicate $\beta\gamma$-crystallin and human γS-crystallin were performed as previously described [53]. Briefly, the genes encoding each protein were cloned into a pET28a(+) vector (Novagen, Darmstadt, Germany) and overexpressed in a Rosetta *E. coli* cell line (DE3) using Studier's autoinduction protocol [87]. Tunicate $\beta\gamma$-crystallin lysate was purified via anion exchange and two runs of size-exclusion chromatography. Human γS-crystallin[1] with an N-terminal 6× His tag and a TEV cleavage sequence (ENLFQG) was purified via nickel affinity chromatography, digestion with TEV protease (produced in-house), subsequent nickel affinity chromatography, and finally, two size exclusion chromatography (SEC) runs. The monomeric and dimeric species were collected separately from the first SEC purification and then subjected to SEC a second time. All samples were dialyzed into metal-free 10 mM HEPES, 0.05 % NaN_3, pH 7.1 unless otherwise stated. Similarly, all samples were reduced via incubation with 5 mM dithiothreitol (DTT) (made fresh) for 30 minutes at RT, dialyzed overnight to remove DTT, and used for measurements immediately thereafter. This procedure was used to prevent the spontaneous dimer formation that can occur at higher concentration in the absence of reducing agent.[88]

2.2.5 Turbidity (Light Scattering)

A Spark TECAN plate reader (Tecan Trading AG, Switzerland) was used to measure light scattering (405 nm) of *Ci*-$\beta\gamma$, HγS-WT and HγS variants in the presence of Cu^{2+} and Zn^{2+} at 30 °C, and Co^{2+} and Ni^{2+} at 42 °C. 200 μL of protein at 50 μM (10 mM HEPES, 50 mM NaCl, pH 7.1) was placed in a 96-well plate and treated with variable equivalents of divalent

[1]Amino acid indices referenced in this paper include the glycine at the first position which is left after TEV cleavage. This glycine is in the position where a start methionine would be, and is often not included in the sequence numbering. The numbering used here therefore differ from some other γS-crystallins references by 1.

cation after a 5 minute baseline period. In Zn^{2+} measurements, after two hours, 2, 10, or 20 equivalents (10 μL) of ethylenediaminetetraacetic acid (EDTA) were added to the solution to chelate available cations. Measurements were recorded every 60 seconds with 5 seconds of shaking before readings. The reported measurements were determined by subtracting the absorbance of the buffer measured in parallel. The light scattering observed for the protein-only solution was identical to the buffer-only samples and is omitted for clarity. To minimize potential instrumental bias, the locations of all samples on a plate were assigned at random.

2.2.6 Tryptophan fluorescence

Thermal denaturation was detected via intrinsic tryptophan fluorescence for *Ci*-$\beta\gamma$ and HγS-WT. 5 μM protein solutions with 50 μM divalent cation ($CaCl_2$, $CoCl_2$, $MgCl_2$, $MnCl_2$, $NiCl_2$, $SrCl_2$, or $ZnCl_2$) or EDTA added were assayed incrementally over a 17-99 °C temperature range. Measurements were acquired using a Varian Cary Eclipse fluorescence spectrophotometer with an excitation wavelength of 280 nm and a 5 nm excitation slit. The sample temperatures were controlled using a Quantum Northwest TC 1 temperature controller (Quantum Northwest, Inc.) with a two minute equilibration at each 1 °C temperature increment. The fraction unfolded was calculated from the 360/320 fluorescence ratio and fit to a two-state equilibrium unfolding model to determine the denaturation midpoint temperature (T_m) of each sample. Fluorescence changes at 330 nm were calculated by subtracting the native protein fluorescence of each sample from the fluorescence following divalent cation addition. Samples were allowed to thermally equilibrate to within instrument sensitivity at 20 °C for two minutes before measurements were made.

The change in intrinsic tryptophan fluorescence was measured for each aforementioned divalent cation. A 1000 μL sample containing 5 μM protein was measured prior to and following the addition of 10 μL of 5 mM divalent cation. Measurements were repeated six times for

each divalent cation.

2.2.7 Dynamic light scattering

Thermal gradient dynamic light scattering (DLS) measurements were performed using a Malvern Zetasizer NS for *Ci*-$\beta\gamma$ measurements and a Malvern Zetasizer μV for HγS measurements. Each sample was composed of 150 μM protein with 975 μM divalent cation. Experiments were performed at 1 °C increments from 20 to 92 °C with two minute equilibrations before measurements and 1 °C/min temperature ramping between measurements. 10 second correlations were measured six times and repeated three times for each temperature step.

2.2.8 Mass Spectrometry

The insoluble aggregates of HγS-WT and HγS-C_0 with 10 equivalent of $CuCl_2$ were prepared via incubation at 30 °C for 12 hours and collected via centrifugation. Pellets were washed four times with double deionized water, once with 20 equivalents of EDTA, once with 10 mM DTT, and twice more with double deionized water. The samples were then dialyzed into double deionized water to remove urea. 0.5 mg/mL samples of both proteins were digested using MS Grade Pierce Trypsin Protease (ThermoFischer Scientific, Rockford, IL, USA) with or without DTT at 37 °C overnight. A Waters Synapt G2 mass spectrometer was used to detect the resulting peptide fragments with a 30 minute separation on a Waters I-Class UPLC column. The resulting MS and MSMS data was analyzed using BioPharmaLynx for peptide and post-translational modification identification. HγS-WT and HγS-C_1 digests were only analyzed for cysteine oxidation products. HγS-C_0 and *Ci*-$\beta\gamma$ were probed for PTMs. The following PTMs were searched for based on previously observed modifications in aged and cataractous lenses[89, 90] and known radical oxidative products[91, 92] : -18 Da

(dehydration/succinimide - S,T/N,D), +1 Da (deamidation - N,D or 2-amino-3-oxo-butanoic acid - T), +4 Da (kynurenine - W), +16 Da (oxidation/hydroxylation - M,C,H,W,F,Y,N,D), +28 Da (carbonylation - S,H,K), +32 Da (dioxidation - C, M), +55 Da (R). Missed trypsin cleavages were required for modified arginine or lysine residues. Only peptides in which at least 35% of b and y ions were observed and for the parent and modified fragments were considered.

2.2.9 Isothermal titration calorimetry

ITC measurements were performed using a MicroCal PEAQ-ITC (Malvern Instruments, Northampton, MA, USA). Each titration consisted of 1.5 μL injections of 2 mM (Ca_2, $SrCl_2$) or 5 mM (Mg_2, Mn_2, Co_2, Ni_2, Zn_2) cation solution to a 200 μM protein sample in 10 mM HEPES (pH 7). Injections were made every 180 seconds for $CaCl_2$ and $SrCl_2$. The remaining samples had the initial 10 injections made every 300 seconds and every 200 seconds for the remaining injection In total, 25 titrations were performed. To control for the heat of dilution, 10 mM divalent cation was titrated into 10 mM HEPES and the resulting data were subtracted from the raw protein data. The ITC data were initially analyzed using Mathematica as previously described[53] to obtain reasonable initial values and then fit to a two-state binding model using MicroCal PEAQ-ITC Analysis Software. The reported fit parameters are the mean of two trials, while the error bars represent one standard deviation.

2.2.10 Solution-state NMR spectroscopy

Experiments were performed at 25 °C on a Varian ^{Unity}INOVA system operating at 800 MHz proton Larmor frequency and equipped with a $^{1}H/^{13}C/^{15}N$ 5 mm tri-axis PFG triple-resonance probe. ^{15}N-^{1}H HSQC experiments were acquired with 4 scans in the direct dimension and 64 scans in the indirect dimension at protein concentrations of 1.7 mM in the

presence of 1, 2, and 6.5 equivalents of $MgCl_2$, $NiCl_2$, $ZnCl_2$, or $SrCl_2$.

Chemical shift perturbations (CSP) were calculated using the following equation: $\Delta\delta_{avg} = \sqrt{\frac{(\Delta\delta_N/5)^2+(\Delta\delta_H)^2}{2}}$. Chemical shift perturbation thresholds for strong (CSP $\geq$ 0.2 ppm) and moderate (0.2 $<$ CSP $\geq$ 0.06 ppm) were based on the chemical shift perturbation reported previously for *Ci*-$\beta\gamma$ interactions with Ca^{2+}.[53] CSP less than 0.06 ppm was classified as unperturbed.

2.2.11 Far-UV circular dichroism

The far-UV circular dichroism (CD) spectra of 5 μM HγS were measured on a J-810 spectropolarimeter (JASCO, Easton, MD). Spectra were recorded from 250 nm to 195 nm using a 1 nm bandwidth and 4 s response.

2.3 Results and Discussion

2.3.1 Vertebrate lens and cation-binding $\beta\gamma$-crystallins differ in amino acid composition

Irrespective of function, all $\beta\gamma$-crystallins are topologically similar. One important conserved feature is an (F/Y/W)xxxx(F/Y)xG motif in the first two β-strands of each Greek key (Figure 2.1). Additionally, disabled versions of the (N/D)(N/D)xx(T/S)S Ca^{2+}-sequence characteristic of cation-binding $\beta\gamma$-crystallins are readily evident in vertebrate lens γ-crystallins. Point mutations in either motif can compromise protein solubility and result in cataract [93, 94, 95, 96, 97]. In particular, reintroduction of Ca^{2+} binding ability in lens γ-crystallins reduces protein stability, [98, 43, 99] raising questions about how vertebrate lens proteins evolved from their metal-binding ancestors. In order to assess the conservation of residues

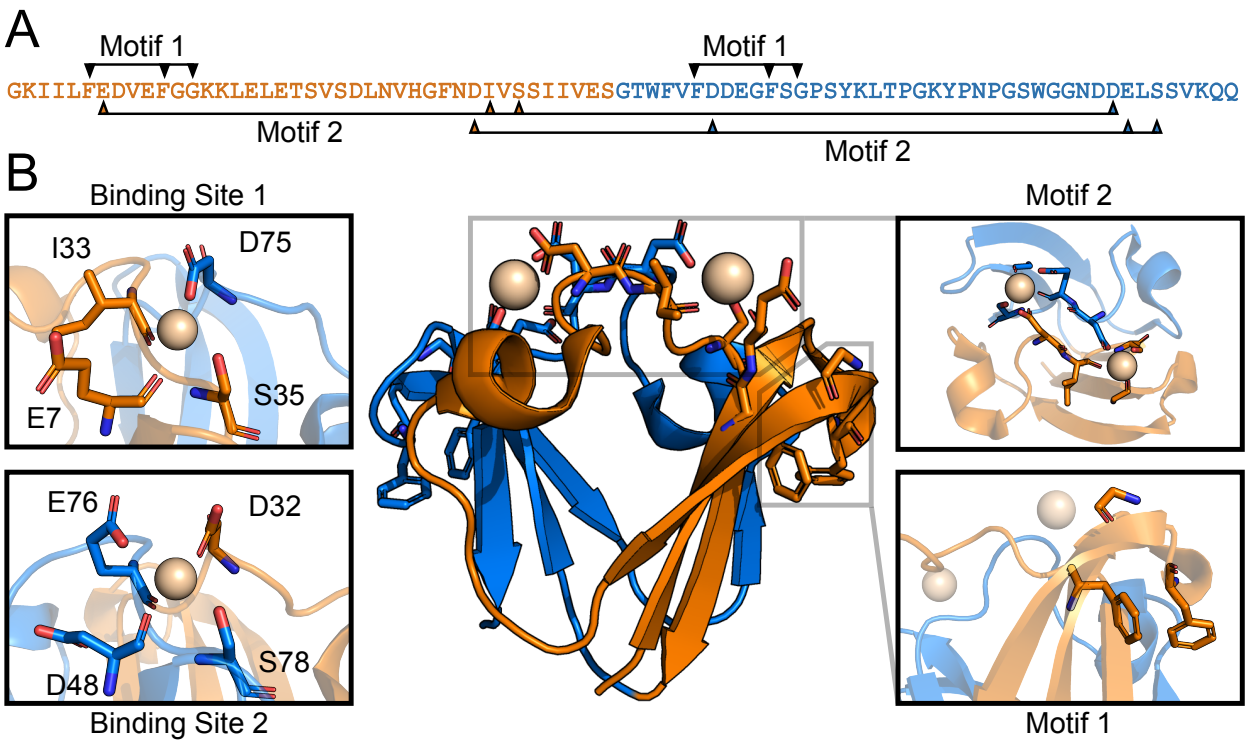

Figure 2.1: (A) The sequence of *Ci*-$\beta\gamma$-crystallin annotated with the residues comprising the (F/Y/W)xxxx(F/Y)xG (motif 1) and cation-binding site (motif 2). The residues of the first Greek key are colored orange; those of the second Greek key are colored blue. (B) Both motifs are visualized within the calcium-bound X-ray crystal structure of *Ci*-$\beta\gamma$ (PDBID: 2BV2).[47] Secondary images are displayed on the right for clarity. The residues comprising the first and second binding site are displayed to the left. The first binding site is made up of the D75 sidechain carboxylate, S35 sidechain hydroxyl, E7 backbone carbonyl, and I33 backbone carbonyl. The second binding site is made up of the D32 sidechain acid, S78 sidechain hydroxyl, E48 backbone carbonyl, E76 backbone carbonyl and E76 sidechain carboxylate.

associated with divalent cation binding during crystallin evolution, the amino acid sequences of cation-binding $\beta\gamma$-crystallins were compared to those of terrestrial vertebrate lens γA-, B-, C-, D-, and S-crystallins. For this analysis, γA-D crystallins were clustered together based on known similarities in gene structure, conservation, and sequence [100, 18], while γS-crystallins were analyzed separately.

One notable difference between the lens and cation-binding $\beta\gamma$-crystallins is in the numbers of positively and negatively charged residues. Cation-binding $\beta\gamma$-crystallins have a net negative charge to aid in the sequestration of cations. In particular, *Ci*-$\beta\gamma$ lacks positively

charged residues in the vicinity of the Ca^{2+} binding sites; however, this feature is not strongly conserved among other cation-binding $\beta\gamma$-crystallins. The lens γ-crystallins contain similar levels of positively and negatively charged residues, with charged residues evenly dispersed across the protein's surface. On average, lens γ-crystallins contain similar total levels of arginine and lysine (γA-D: 12.9 $\pm$ 0.8%, γS: 12.4 $\pm$ 0.8%), histidine (γA-D: 3.2 $\pm$ 1.0%, γS: 3.2 $\pm$ 0.8%), and acidic residues (γA-D: 12.8 $\pm$ 0.6%, γS: 13.5 $\pm$ 0.4%) (Figure 2.2, Supplementary Table S1). Cation-binding $\beta\gamma$-crystallins contain comparable levels of negatively charged residues ($\beta\gamma$: 11.5 $\pm$ 2.6%) but lower levels of arginine and lysine residues ($\beta\gamma$: 8.2 $\pm$ 2.5%). Similarly, low levels of histidine (0.7 $\pm$ 0.6%), cysteine (0.5 $\pm$ 0.9%), and methionine (0.6 $\pm$ 0.9%) are found in the cation-binding crystallins. This observation is unsurprising, as cysteine and histidine are the most commonly observed residues in protein metal binding sites and are therefore expected to be localized to the binding sites and hence rare overall.[101] Furthermore, cysteine and methionine are readily oxidizable: post-translational modifications at these sites could result in structural changes, either reducing the stability of the *apo-* form or the binding affinity in the *holo-* form. Despite their similar net charges, the γA-D and γS-crystallins differ substantially in the distribution of positively-charged residues between lysine and arginine. On average, γA-D-crystallins have a 17:2 arginine to lysine ratio compared to the 3:2 ratio observed in the γS-crystallins. This difference may be driven in part by the higher refractivity of arginine, as γA-D-crystallins are located in the more highly refractive lens nucleus, while γS-crystallins are more abundant in the cortex.[102]

2.3.2 Solvent-exposed cysteines are strongly conserved in lens crystallins but not calcium-binding crystallins

Methionine, cysteine, and histidine are more common in lens γ-crystallins than calcium-binding crystallins, consistent with their high refractivity. Methionine is particularly abun-

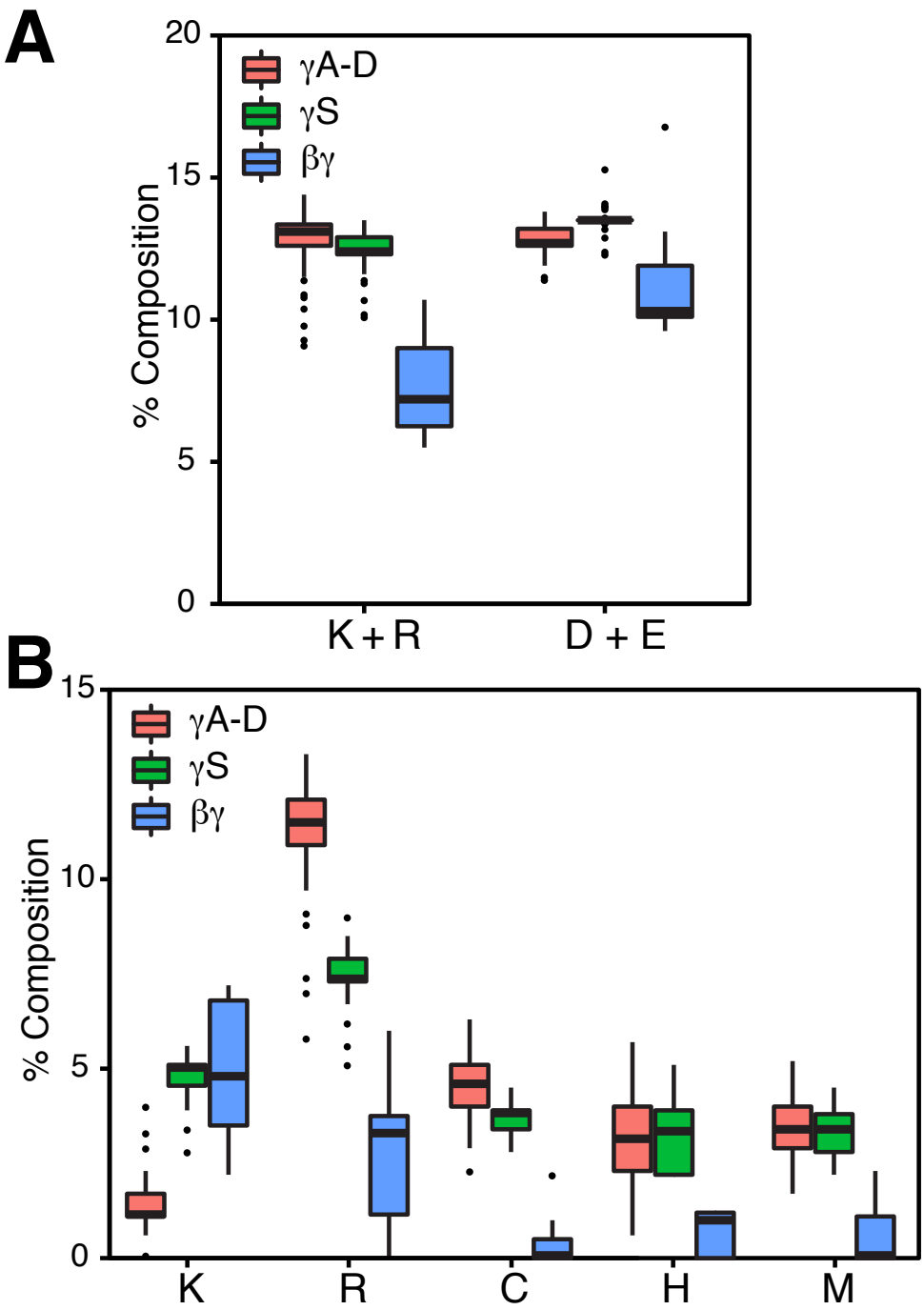

Figure 2.2: Combined and individual amino acid sequence percentages of lens γA-D (red), lens γS (green), and cation-binding $\beta\gamma$-crystallins (blue). Each box covers the 25th to 75th percentiles and whiskers extend to 1.5 times the largest value in the respective quartile range. (**A**) Percentages of positively charged (lysine and arginine) and negatively charged (aspartate and glutamate) residues. (**B**) Lysine, arginine, cysteine, histidine, and methionine sequence percentage of each group.

dant in fish γM-crystallins, many of which contain up to 15% methionine.[103] Overall, the refractive function of lens proteins leads to their being enriched in polarizable amino acids.[29] Here, both groups of lens γ-crystallins are enriched in highly refractive amino acids relative to their metal-binding counterparts (Supplementary Figure S1), consistent with the measured difference in dn/dc values for human γS (0.2073) and *Ci*-βγ (0.1985). [31] Relative to side-chain size, cysteine is the most refractive whereas alanine is the least of any amino acid (Supplementary Figure S2), leading to the hypothesis that cysteine plays a critical functional role in the highly refractive lens crystallins. This idea is supported by the sequence data, which indicate that many cysteine residues found in lens γ-crystallins are replaced by other residues in cation-binding crystallins (Supplementary Table S2.) In contrast to cation-binding βγ-crystallins, where the few cysteines present are usually found in disulfide bonds, lens proteins have free, solvent-exposed cysteines (Supplementary Table S3-S4) whose function is not fully understood. Although serine is the most common alternate residue at consensus cysteine positions, a variety of amino acids are observed at the homologous positions in other γ-crystallins (Supplementary Table S2).

In lens γ-crystallins, several conserved cysteine positions are found, predominately in the N-terminal domain (Supplementary Table S5). For both domains, the cysteines closest to one another in space are located in and around the third β-strand. The most concentrated locus of conserved cysteines is found in the N-terminal domain of HγS. C23 and C27 are the closest cysteine pair in this region, and are both spatially adjacent to C25 and C83 (Figure 2.3). The location of C23, C25, C27 across the second and third β-strands of the first Greek key results in high solvent accessibility—21%, 77%, and 40% respectively—for each side chain. Both of these features, close proximity and high solvent accessibility, were noted by Thorn et al. as factors enabling this triad to drive the formation of domain-swapped dimers [88]. Across the lens γA-D crystallins, the homologous positions to C23 and C83 are similarly occupied by cysteines. The position homologous to C27 is the most conserved position across both domains of the lens γ-crystallins, and is replaced by a histidine only in

the N-terminal domain of γD, while the C25 position is unique to the γS-crystallins.

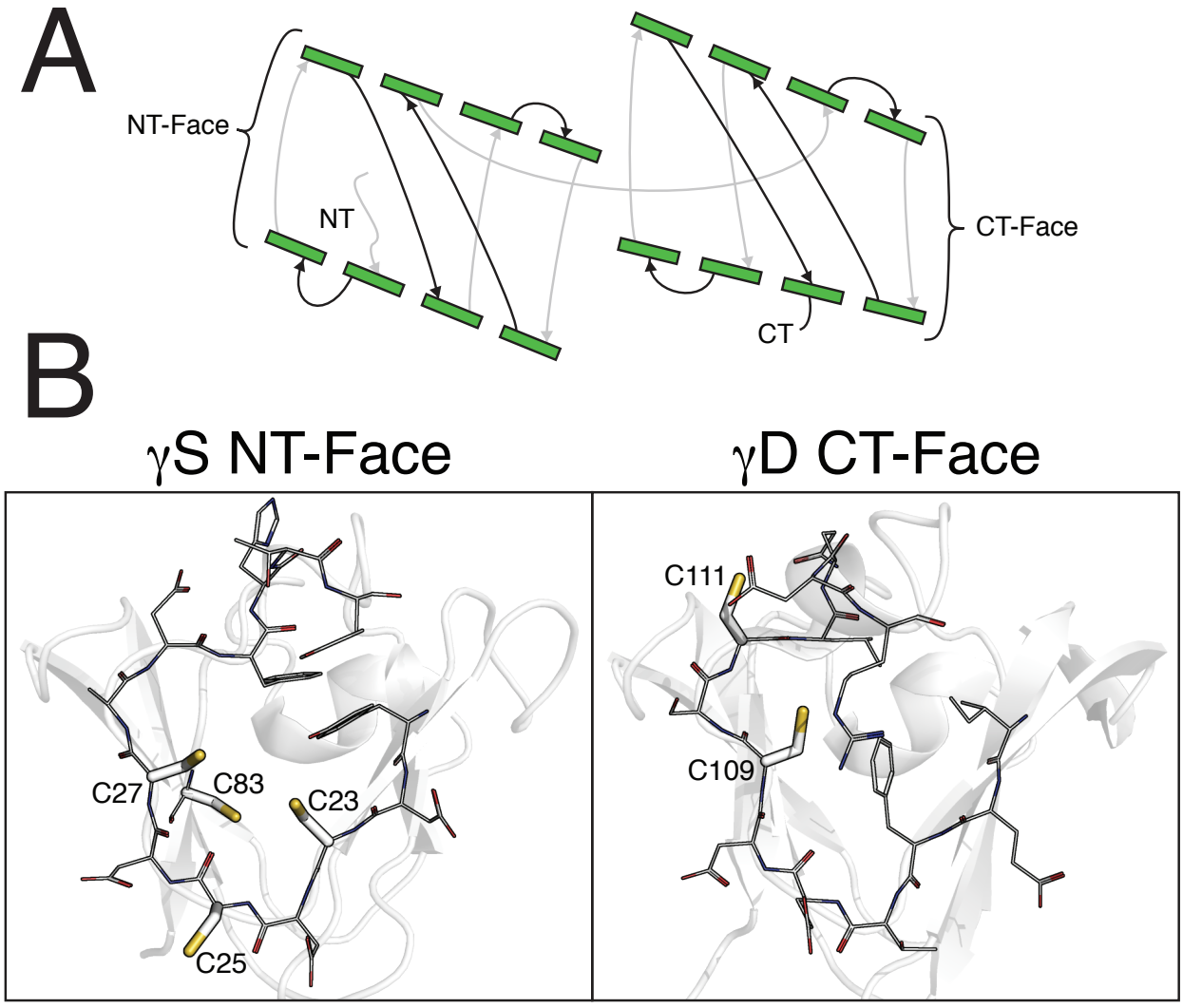

Figure 2.3: (A) A schematic of the γ-crystallin structure showing the location of the external β-sandwich faces of the N-terminal and C-terminal domains. The β-strands of the protein are shown as green rectangles lines drawn between them to illustrate the relative strand connectivity (black - top, gray - bottom). (B) The ribbon structure of N-terminal face of γS (PDBID: 2M3T [85]) and and C-terminal face of γD-crystallin (PDBID: 1HK0 [84]) are shown overlaid with line renderings of relevant residues. The cysteines of both faces are shown as sticks. γS-C83 is depicted in γS-NT face due to its proximity despite being located one β-strand behind the N-terminal face.

The apparent functional significance of these conserved cysteine residues raises questions about the underlying selection process. Although these residues are highly refractive, they are also capable of non-native intermolecular disulfide bond formation that can lead to aggregation, complicating their utility in an environment where solubility is just as critical as refractivity. Disulfide exchange in human lens γ-crystallins has recently been proposed to help regulate the local redox potential of the lens [104], however, inter- and intramolecular disulfide bonding has also been shown to facilitate domain swapping in γS-crystallin, providing a possible nucleation site for the formation of deleterious aggregates [88]. Cysteines from each γ-crystallin have also been identified as sites for post-translational modifications in aged lenses [89, 105], while the more solvent-exposed cysteines of γD-crystallin have been shown to be the primary contributors to copper-mediated aggregation [60].

For all conserved cysteine positions we calculated the non-synonymous and synonymous codon substitutions to investigate potential selective pressure. For each γ sequence alignment, a maximum-likelihood phylogenetic reconstruction was performed to enable calculation of the nonsynonymous and synonymous substitution rates via SLAC (Single-Likelihood Ancestor Counting) and FEL (Fixed Effects Likelihood) [106]. No positions exhibit evidence of positive (diversifying) selection, while numerous cysteines, particularly in γS-crystallin, exhibit evidence of strong negative (purifying) selection. Compared to the α- and β-crystallins, the γ-crystallins are the most enriched in cysteine. Moreover, in the six human β-crystallins a cysteine is observed at the position homologous to C27 in HγS, with only 15 total cysteines elsewhere. Notably, no substitutions were observed for the codons of γA-C78, γC-C108 (human γD numbering convention), and γS-C83 (human γS numbering convention). No evidence of positive selection was observed for any of the sites examined across all lens γ-crystallins. Each of the seven conserved cysteines of the γS-crystallins appear to experience strong negative selection ($p \leq 0.05$), while $\sim$20% of γA-D crystallins experience similar selection (Supplementary Table S6).

The strong conservation of cysteines in all γ-crystallin sequences and the mutual proximity of the cysteines in the N-terminal domain of γS-crystallin led us to design variants that remove one or more prominently exposed Cys residues in HγS. We hypothesize that if divalent cation interactions are relevant to protein stability or lens homeostasis, mutating C23, C25, and/or C27 would alter cation-binding activity. Therefore, variants with two (HγS-C_2 = γS-C23S/C27S), one, (HγS-C_1 = γS-C23S/C25S/C27S) or zero (HγS-C_0 = γS-C23S/C25S/C27S/C115S) solvent-accessible cysteines were produced. For each mutation we chose serine, as oppose to alanine, as a replacement due to its similar size and the observation that it is the most common alternative residue at these sites. The resulting variants also enabled us to more directly compare the behavior of human γS-crystallin and *Ci*-$\beta\gamma$ crystallin, which does not contain cysteine, in the presence of various divalent cations. The results of these experiments are described in subsequent sections.

2.3.3 *Ci*-$\beta\gamma$ can accommodate a wide range of divalent cations

Unlike better-characterized Ca^{2+} motifs, such as the EF-hand [107, 108] or C2-domain [109], the double clamp motif of $\beta\gamma$-crystallins has not yet been throughly tested for non-Ca^{2+} divalent cation interactions. Previous research has shown Protein S binds Mg^{2+} with one order of magnitude lower affinity [110], and M-crystallin has been crystallized in the presence of Mg^{2+} (PDBID: 5HT9), however, neither domain of *Yersinia* crystallin interacts with Mg^{2+} [111]. *Ci*-$\beta\gamma$ is a useful $\beta\gamma$-crystallin to investigate non-Ca^{2+} divalent cation binding, due to its high Ca^{2+} affinity, native monomeric form, and the minor asymmetry between its binding sites. Moreover, its native location in a light-sensing organ makes it the best cation-binding $\beta\gamma$-crystallin for comparative analysis with lens γ-crystallins. *Ci*-$\beta\gamma$ binds Ca^{2+} via two-site sequential binding, with high affinity at both sites relative to other $\beta\gamma$-crystallins [99, 53].

Here we used isothermal titration calorimetry (ITC) to investigate the thermodynamics

Table 2.1: Thermodynamic parameters for binding of Ca^{2+} and Sr^{2+} to *Ci*-$\beta\gamma$.

	K (M^{-1})	ΔH (kJ/mol)	ΔG (kJ/mol)	-TΔS (kJ/mol)
Ca^{2+} Site 1	3.5 x 10^8±2.2 x 10^8	-26.6±6.5	-48.5±1.7	-21.9±8.7
Ca^{2+} Site 2	5.9 x 10^7±1.2 x 10^7	-21.9±0.8	-44.4±0.5	-22.5±0.3
Sr^{2+} Site 1	1.2 x 10^8±1.8 x 10^7	-31.6±2.3	-46.0±0.4	-14.4±2.5
Sr^{2+} Site 2	5.6 x 10^6±3.2 x 10^6	-18.5±1.7	-38.3±1.6	-19.8±3.3

of interactions between *Ci*-$\beta\gamma$ and a variety of divalent cations. The binding isotherms of *Ci*-$\beta\gamma$ to Ca^{2+} and Sr^{2+} were exothermic, while the rest exhibited biphasic behavior. Similar results have been previously reproted for other systems, e.g. [112, 113, 114] The extent of exothermic character of the biphasic isotherms was $Mg^{2+} > Mn^{2+} > Co^{2+} > Ni^{2+} > Zn^{2+}$ (Supplementary Figure S3). The isotherm produced by Sr^{2+} was highly similar to that of Ca^{2+}; the observed data for both cases could be fit to same exothermic two-state model previously reported[53] (Supplementary Figure S4). The binding constants and parameters calculated show slightly stronger binding than we previously reported for *Ci*-$\beta\gamma$ to Ca^{2+} in Tris buffer. The overall dissociation constant [$K_d = 1/\sqrt{(K_1K_2)}$] for Ca^{2+} was found to be 0.004 μM and 0.039 μM for Sr^{2+} (Table A.3)[53]. The identities of the binding sites corresponding to the high and lower affinity binding of Ca^{2+} and Sr^{2+} are not yet known, however we suspect the higher-affinity binding of both cations occurs at the 5-coordinate site and the lower affinity binding occurs at the 4-coordinate site. The two sites are nearly identical, differing only in their third residues. In the first binding site, I33 coordinates cations via its backbone carbonyl whereas the homologous E76 at the second site also coordinates through its sidechain (Figure 2.1). The sidechain coordination from the third residue of the second binding site in *Ci*-$\beta\gamma$ is not observed in any other cation-binding $\beta\gamma$-crystallin, which may explain the remarkably high Ca^{2+} affinity of this protein.

Ci-$\beta\gamma$ and M-crystallin (36.6%, identity 67.1% similarity via LALIGN[7]) both exhibit similar structural changes upon Ca^{2+} binding, contain two octahedral binding sites, and bind via two-site sequential binding with one order of magnitude difference between sites [67]. A comparison of M-crystallin crystal structures bound to Ca^{2+} (PDBID: 3HZ2 [68]) and

Mg^{2+} (PDBID: 5HT9) shows that the ligand-cation distances are shorter for Mg^{2+} binding (Supplementary Table S7). The tetrahedral volume between binding site ligands decreases more at the second site from Ca^{2+} and Mg^{2+} binding. The greater reduction in ligand space suggests a greater flexibility at the second binding site. We hypothesize that the second site of *Ci*-$\beta\gamma$ is similarly flexible, and would therefore bind with a higher affinity.

Residue-specific interactions of Sr^{2+}, Mg^{2+}, Ni^{2+}, and Zn^{2+} with *Ci*-$\beta\gamma$ were investigated using solution-state NMR. ^{1}H-^{15}N HSQC [115] chemical shift perturbations (CSPs) were measured to identify the residues involved in divalent cation interactions (Supplementary Figures S5-S6). Classification of CSP strength was done according to standard threshold levels: (strong ≥ 0.2, moderate ≥ 0.06). Strong and moderate CSPs from the addition of 6.5 equivalents of divalent cation are shown mapped onto the X-ray crystal structures of the Ca^{2+}-bound protein (PDBID: 2BV2) [47] in Figure 2.4. The regions corresponding to strong CSPs and absent peaks resulting from Sr^{2+}, Mg^{2+}, Ni^{2+}, and Zn^{2+} interactions exhibited distributions that strongly resemble the CSP profile of Ca^{2+}-bound *Ci*-$\beta\gamma$.

For all the divalent cation interactions, strong CSPs were concentrated in the loop regions (31-36 and 72-79) containing three of the four binding moieties for each site (Site 1: I33-O, S35-OG, D75-OD1; Site 2: D32-OD1, E76-O/OE1, S78-OG). The residues completing the binding site motifs (Site 1: E7-O/OE1; Site2: D42-O), located before the β-hairpins, also displayed moderate to strong CSPs. Minor CSPs were also observed along the β-strands of the Greek keys and in other solvent-exposed surfaces away from the two binding sites for all divalent cations. Notably, above 3 equivalents of metal cation, Ni^{2+} binding resulted in the disappearance of chemical shifts from residues at and adjacent to the calcuim binding site, presumably due to paramagnetic relaxation enhancement, whereas Zn^{2+}, and to a lesser extent Mg^{2+}, yielded fewer assignable chemical shifts, possibly due to a transition into the intermediate exchange dynamic regime. In general, each tested metal cation interacts strongly with residues composing and adjacent to the Ca^{2+} binding site. Although the abil-

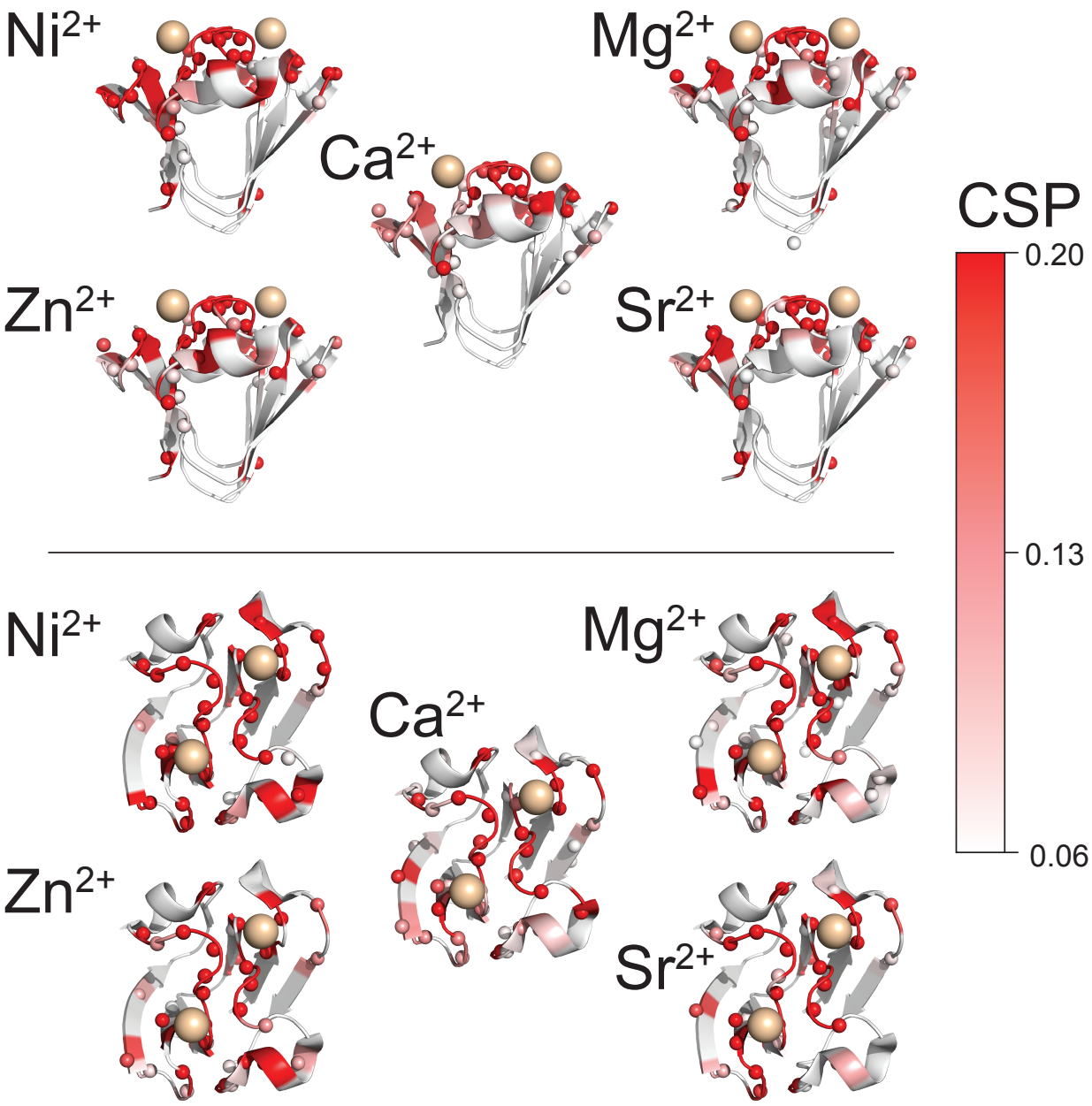

Figure 2.4: ^{1}H-^{15}N-HSQC CSPs of *Ci*-$\beta\gamma$ resulting from the addition of 6.5 equivalents of Ca^{2+}, Sr^{2+}, Mg^{2+}, Ni^{2+}, and Zn^{2+} were mapped onto the structure of *Ci*-$\beta\gamma$ (PDBID: 2BV2). Weak CSPs (≤ 0.06) are colored white, strong CSPs (≥ 0.2) are colored red, and moderate CSPs are colored using a red to white gradient. The color gradient is projected onto the cartoon backbone and the spheres representing backbone amide nitrogens. Ca^{2+} ions found in the crystal structure are represented as tan spheres.

ity of Mg^{2+}, Sr^{2+} and various transition metals to coordinate to Ca^{2+} binding sites has been reported for other Ca^{2+}-binding proteins such as calmodulin [116, 117, 118], calcium- and integrin-binding protein [119, 120], and parvalbumin [121], this represents the first demonstration of a $\beta\gamma$-crystallin coordinating a wide range of non-Ca^{2+} cations.

2.3.4 Divalent cations increase the thermal stability of *Ci*-$\beta\gamma$, but not HγS

Biophysical characterization was performed for *Ci*-$\beta\gamma$ and HγS in the presence of a variety of divalent cations to further investigate how the observed composition differences impact protein stability. Thermal unfolding curves were measured for both proteins via the 360/320 nm ratio of tryptophan fluorescence intensities. Tryptophan side-chains in non-polar environments have a peak fluorescence near 320 nm, while those in highly polar environments, e.g. aqueous solution, fluoresce at 360 nm. All tryptophans in the folded structures of *Ci*-$\beta\gamma$ and HγS are buried in the hydrophobic core of the protein, therefore, the ratio of fluorescence intensity at 360/320 as a function of temperature is a sensitive marker of protein unfolding, as previously demonstrated for $\beta\gamma$-crystallins.[122, 123]

As previously reported, the Ca^{2+}-bound form of *Ci*-$\beta\gamma$ has a greatly increased thermal unfolding midpoint (T_m) over the *apo*-form, with a dramatic increase from 46 °C to 94 °C [53] (Figure 2.5A). A similar stabilization was observed in the presence of Sr^{2+}, yielding a T_m of 91 °C. Of the tested divalent metal cations, the next greatest T_m was observed for Mn^{2+} (84 °C) followed by Mg^{2+} (71 °C), Co^{2+} (70 °C), Ni^{2+} (61 °C), and Zn^{2+} (53 °C) ((Figure 2.5B). For the tested cations, a higher T_m was observed to correlate with sharper unfolding transition. The exception to this trend was Zn^{2+}, where the *Ci*-$\beta\gamma$ unfolding temperature range is similar to that of the Sr^{2+} and Ca^{2+}-bound forms. The presence of Ca^{2+} did not alter the T_m of HγS ((Figures 2.5C, 1D), consistent with its previously observed weak binding

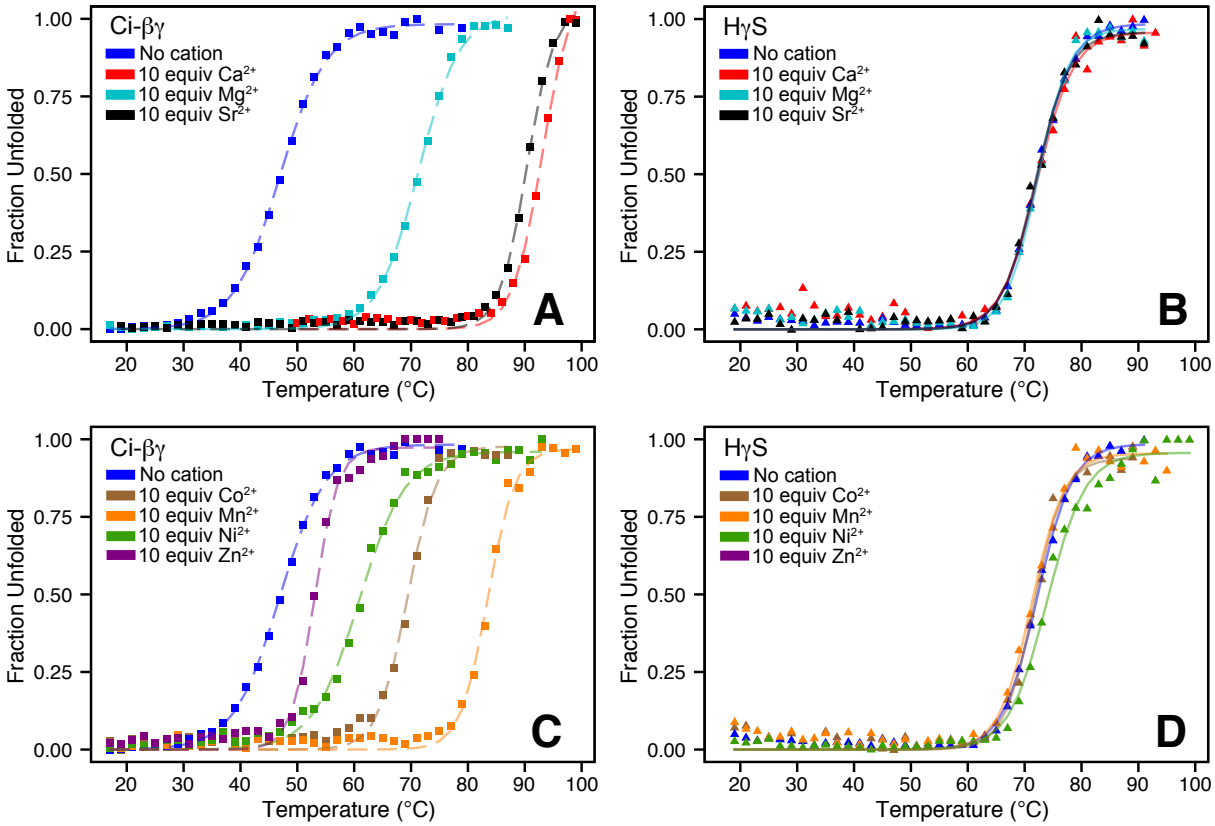

Figure 2.5: Protein thermal unfolding in the presence of 10 equivalents of divalent cation. (**A**) *Ci-βγ* in the presence of Ca^{2+} (red), Mg^{2+} (aqua), Sr^{2+} (black), or no cation (blue). (**B**) HγS in the presence of Ca^{2+} (red), Mg^{2+} (aqua), Sr^{2+} (black), or no cation (blue). (**C**) *Ci-βγ* in the presence of Co^{2+} (brown), Mn^{2+} (orange), Ni^{2+} (green), Zn^{2+} (purple), or no cation (blue). (**D**) HγS in the presence of Co^{2+} (brown), Mn^{2+} (orange), Ni^{2+} (green), or no cation (blue).

Table 2.2: Divalent cations classification and effect on *Ci*-$\beta\gamma$ unfolding.

	$\mathbf{T}_m$[2]	$\mathbf{T}_i$[3]	**Ionic radius**[4]	**Classification**[5]	**MESPUES CN**[6]	**CSD CN**[7]
Ca^{2+}	94°C	82°C	100 pm	Hard	6-8	6, 7
Sr^{2+}	91°C	79°C	118 pm	Hard	-	6, 8
Mn^{2+}	84°C	72°C	83 pm[8]	Borderline	6	6
Mg^{2+}	71°C	58°C	72 pm	Hard	6	6
Co^{2+}	70°C	55°C	74.5pm[9]	Borderline	6	4, 6
Ni^{2+}	61°C	50°C	69 pm	Borderline	4	4, 6
Zn^{2+}	53°C	40°C	74 pm	Borderline	4[10]	4
Apo	46°C	60°C	-	-	-	

and lack of changes to NMR chemical shifts upon cation addition [53]. None of the tested divalent cations alter the thermal unfolding behavior of HγS: the T_m was ~72 °C for all samples, consistent with previous literature reports.[124, 125, 126]

The wide range of effects on thermal stability of the divalent cations on *Ci*-$\beta\gamma$ warrants some discussion of metal ion properties, given that all of these ions have a charge of +2 and are similar in size. Notably, the thermal stabilization from Mn^{2+} is 12-13 °C greater than that due to Mg^{2+}. Examination of different metal ion properties indicates that stabilization *Ci*-$\beta\gamma$ correlates most strongly with coordination number, followed by ionic radius (Table 2.2). In other proteins, the native binding sites of Mn^{2+} and Mg^{2+} are most often BCH and BCB motifs, where binding is predominately coordinated via acid residues.[127] The reduced affinity binding of Mn^{2+} and Mg^{2+} to Ca^{2+} coordination sites has been suggested to stem primarily from differences in ionic radius.[107] A small radius may alter the cation's interaction with some bidentate ligands. A similar argument can be made for Sr^{2+} over Mn^{2+}, despite limited experimental data on Sr^{2+} binding in proteins. Although its ionic radius is slightly larger than that of Ca^{2+}, Sr^{2+} binding results in the same structural changes, with small reductions in ligand-cation coordination. Any minor changes in backbone coordination may then be accommodated by the flexibility of the aspartate and glutamate residues in the binding site.

2.3.5 Divalent cations alter thermal aggregation in both *Ci*-$\beta\gamma$ and HγS

Thermal gradient DLS was used to probe divalent cation-mediated changes in protein-protein interactions leading to the formation of soluble oligomers and insoluble aggregates. In DLS, a translational diffusion coefficient is measured via scattering correlation times, providing a sensitive tool for the detection of oligomer formation. γ-crystallin aggregation under thermal stress often proceeds via a step function in which a sudden onset of oligomerization occurs directly from the monomeric population. We use the notation T_i to refer to the initial temperature at which oligomers or aggregates form from the starting solution of monomers. These early-stage soluble oligomers formed are one to two orders of magnitude larger in size than the monomers or dimers they were derived from. These particles grow in size until they precipitate from solution, resulting in a decrease in scattering intensity, at which point the measurement was terminated.

Thermal unfolding data for *Ci*-$\beta\gamma$, in the apo form and bound to a variety of divalent cations, are shown in Figure 2.6 A-C. The T_i of *apo-Ci*-$\beta\gamma$ occurs near 60 °C, resulting in 20 nm-diameter oligomers. The oligomers remain soluble and increase in diameter to 50 nm at 92 °C. Ca^{2+}- and Sr^{2+}-bound *Ci*-$\beta\gamma$ exhibit T_i values of 82 °C and 79 °C, respectively, above which the oligomer diameter immediately exceeds 100 nm. The addition of Mg^{2+} to *Ci*-$\beta\gamma$ does not alter the T_i (58 °C) relative to the *apo*-form, but yields 35 nm diameter oligomers. The soluble oligomers increase in size with increasing temperature, with 50 nm oligomers forming at 70 °C. Of the tested transition metal cations, only Mn^{2+} significantly increased

[2]Thermal denaturation midpoint (T_m) determined via intrinsic fluorescence.
[3]Initial temperature of aggregation (T_i) determined via DLS.
[4]All ionic radius values are taken from Shannon *et al* [128] using the 6-coordinate, 2+ charge state.
[5]From Pearson's classification of hard and soft acids and bases. [129]
[6]Coordination number (CN) collected from MESPEUS 10 and Hsin *et al* [130]
[7]Coordination number (CN) taken from Dudev *et al*[131], Tables 1, 2, and 3 for frequencies $\geq$ 33 %.
[8]High-spin ionic radius.
[9]High-spin ionic radius.
[10]Taken form Harding *et al*[132], Table 5.

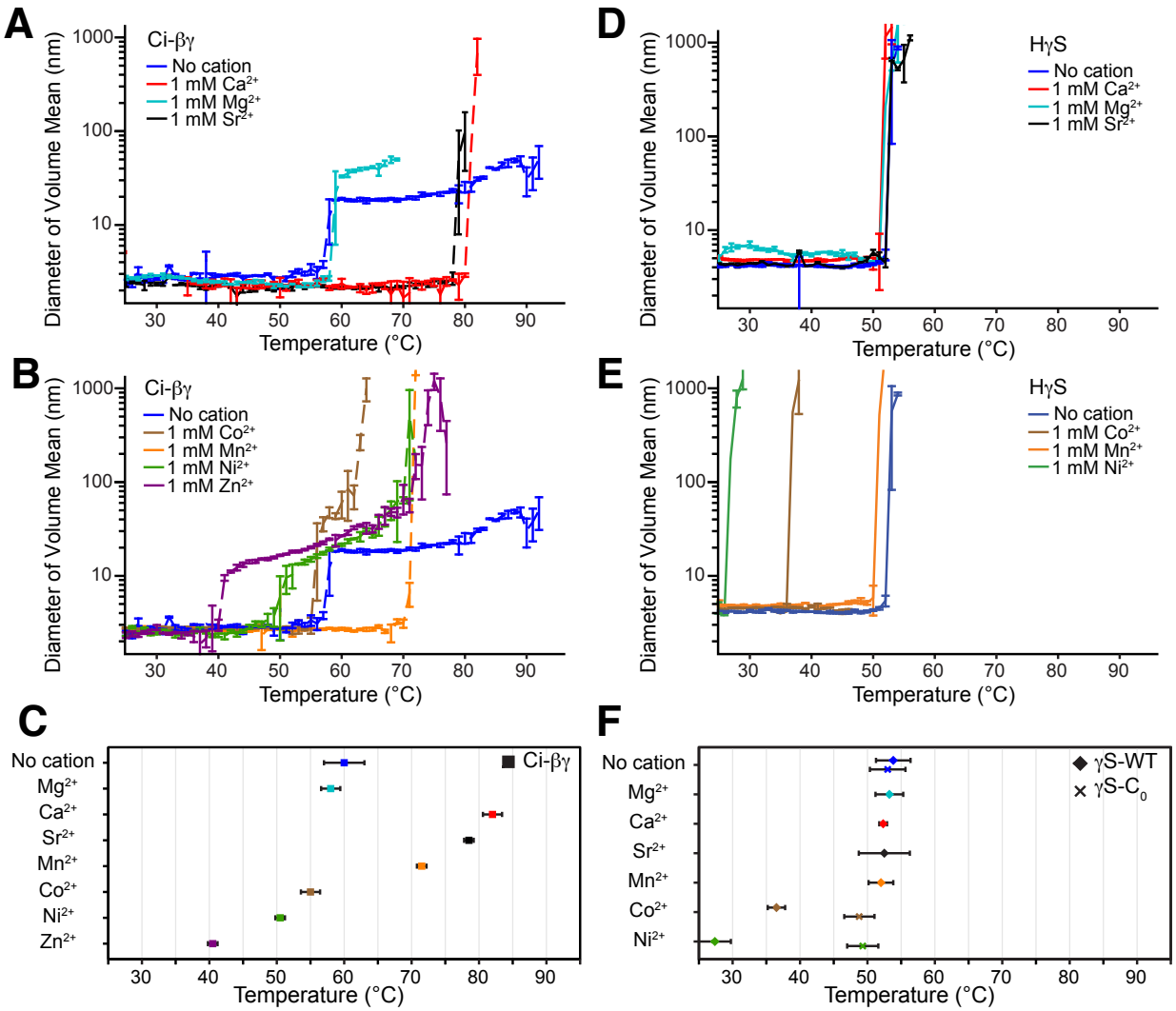

Figure 2.6: DLS was used to monitor the diameter of protein monomers and oligomers to access the temperature of aggregate formation under thermal stress and in the presence of 10 equivalents of divalent cation. (**A**) DLS measurements for *Ci-βγ* in the presence of Ca^{2+} (red), Mg^{2+} (aqua), Sr^{2+} (black), or no cation (blue). (**B**) DLS of *Ci-βγ* in the presence of Co^{2+} (brown), Mn^{2+} (orange), Ni^{2+} (green), Zn^{2+} (purple), or no cation (blue). Each measurement trace reflects one representative measurement, where error bars correspond to one standard deviation collected from triplicate sampling at each temperature. (**C**) The initial temperature of oligomer formation (T_i) for *Ci-βγ* under thermal stress measured via DLS. The T_i refers to the lowest temperature at which species larger than the native monomers are observed. This plot is derived from the data shown in Panels (**A**) and (**B**); this alternative visualization facilitates comparison of the aggregation onset temperatures and allows more straightforward presentation of the measurement error. Error bars represent one standard deviation. (**D**) DLS for HγS in the presence of Ca^{2+} (red), Mg^{2+} (aqua), Sr^{2+} (black), or no cation (blue). (**E**) DLS of HγS in the presence of Co^{2+} (brown), Mn^{2+} (orange), Ni^{2+} (green), or no cation (blue). *Ci-βγ* (top), were measured (**E**) The initial temperature of oligomer formation (T_i) for HγS (diamonds), and HγS-C_0 (Xs), presented as in Panel (**C**)

the T_i of *Ci*-$\beta\gamma$. As observed for Ca^{2+} and Sr^{2+}, oligomers formed at the T_i (70 °C) rapidly exceed the observable size. The addition of Co^{2+}, Ni^{2+}, or Zn^{2+} reduces the T_i of *Ci*-$\beta\gamma$. Co^{2+} reduces the T_i from 60 °C to 55 °C. The oligomers initially formed in the presence of Co^{2+} are 30 nm in diameter and grow to 70 nm by 65 °C, above which the scattering signal is saturated. The T_i values for Ni^{2+} and Zn^{2+} are 50 °C and 40 °C, respectively, where both form relatively small oligomers between 10 nm and 20 nm, with slow growth producing 50 nm oligomers at 70 °C. More rapid increases are observed at higher temperatures.

The analogous data for HγS are presented in Figure 2.6 D-F. In the absence of divalent cations, HγS rapidly forms insoluble aggregates around 53 °C, consistent with prior studies of HγS alone [125]. The T_i of HγS does not change in the presence of Ca^{2+}, Sr^{2+}, or Mg^{2+}; immediate formation of aggregates is observed in the presence of each of these cations. The transition metal divalent cations Co^{2+} and Ni^{2+} reduced the T_i of HγS, to 50 °C and 46 °C, respectively, whereas Mn^{2+} did not alter the T_i. For all HγS measurements, the aggregate size rapidly exceeded 100 nm. The addition of Zn^{2+} immediately produced large aggregates that precipitated out of solution, therefore, no DLS data are reported for treatment of HγS with this cation. Although *Ci*-$\beta\gamma$-crystallin resists Cu^{2+}-induced aggregation more effectively than γS-WT, upward of six equivalents results in light scattering (Supplementary Figure S7). In comparison, Zn^{2+} similarly aggregates γS-WT, whereas the presence of up to 10-fold Zn^{2+} does not reduce the solubility of *Ci*-$\beta\gamma$. For the variant HγS-C_0, which does not contain solvent-accessible cysteines, the T_i in the presence of Co^{2+} and Ni^{2+} are both around 49 °C.

2.3.6 Zn^{2+}-driven aggregation of HγS proceeds through cysteine coordination, whereas Cu^{2+}-driven aggregation results from methionine oxidation

In the healthy eye lens, γ-crystallins undergo only weak and transient interactions. Previous studies measuring γ-crystallin interaction with exogenous peptides,[133] small molecules,[134] and cations[39] have highlighted the ability of the lens γ-crystallins to tolerate potentially destabilizing interactions to a certain extent; however this capacity is limited and aggregation results from excessive intermolecular contacts. We therefore focused on changes to protein solubility as a practical approach to determine the potential effects of divalent cations on γ-crystallin behavior. The addition of excess Ca^{2+}, Sr^{2+}, Mg^{2+}, and Mn^{2+} did not alter the fluorescence or thermal unfolding of HγS, consistent with previous research demonstrating that HγD-crystallin does not aggregate upon addition of Mn^{2+}, Fe^{2+}, or Ca^{2+},[39, 135] and that γB and γS-crystallins do not interact with Ca^{2+}.[53, 97] Co^{2+} and Ni^{2+} did not alter the thermal unfolding of HγS, but when present in excess (6.5 fold), produced soluble aggregates under thermal stress, and detectable light scattering after 2 hours at 42 °C (Supplementary Figure S8). The addition of Zn^{2+} results in appreciable aggregation without thermal stress in low excess; therefore, further light scattering measurements were performed on the Cys to Ser variants HγS-C_2, HγS-C_1, and HγS-C_0, which were designed to test the hypothesis that solvent-exposed cysteines are responsible for aggregation-promoting interactions with metal cations in HγS.

At room temperature, aggregates of HγS readily form following the addition of 5 equivalents of Zn^{2+} or 1 equivalent of Cu^{2+}. Characterization of metal-induced aggregation was therefore measured via light scattering at 405 nm. Zinc-induced aggregation of HγS was measured for both the monomeric and dimeric forms (Figure 2.7). 1 equivalent of Zn^{2+} produced limited aggregation of monomeric HγS, while 5 and 10 equivalents induced elevated levels

of light scattering. Upon addition of 10, but not 5, equivalents of Zn^{2+}, a small increase in light scattering of HγS dimers was observed. Similar measurements were performed using monomeric HγS-C_2, HγS-C_1, and HγS-C_0. Similar to HγS-WT, each of the Cys-to-Ser variants produced negligible aggregation in the presence of 1 equivalent of Zn^{2+}. Appreciable γS-C_2 aggregation was observed for the addition of 10 equivalents of Zn^{2+}, while 5 equivalents produced slightly less aggregation. 10 and 5 equivalents of Zn^{2+} yielded similarly low levels of aggregation for γS-C_1, while detectable aggregation of γS-C_0 was only observable at two hours with 10 equivalents. For all proteins and zinc ion equivalents, the addition of EDTA reduced the light scattering intensity to background levels (Figure 2.7).

The removal of surface-exposed cysteines in HγS-C_0 abrogated Zn^{2+}-mediated aggregation (Figure 2.7A) as well as Ni^{2+} and Co^{2+}-induced aggregation under mild thermal stress. For all proteins tested, Zn^{2+} aggregation was reversible upon addition of EDTA (Figure 2.7B), supporting our hypothesis that zinc ions coordinate to HγS via solvent-accessible cysteines and cause intermolecular bridging. Dimerization of HγS, presumably via C25 disulfide bond formation, limits cysteine solvent accessibility. The dramatically reduced aggregation in HγS dimer-only solutions further supports the idea that cysteine solvent accessibility regulates Zn^{2+}-mediated intermolecular bridging aggregation. Dominguez et al. previously reported that Zn^{2+} induces trace aggregation of HγS, but did not specify the extent of dimerization.[135] Therefore, we suspect that dimerization is responsible for the discrepancy between our results and those reported in this prior study.

Although Hγ-WT aggregates to a greater total extent than HγS-C_2 and HγS-C_1, it does so more slowly. We hypothesize that Zn^{2+} may interact with the more buried C23 (21% SASA) or C27 (40% SASA), resulting in a lesser solvent-accessible surface area for the zinc ion. In this case, the clustered cysteines may serve as a weak buffer against intermolecular bridging. In HγS-C_2 and HγS-C_1, where the remaining solvent-exposed cysteines are not spatially proximal to each other, most of the increase in light scattering occurs immediately.

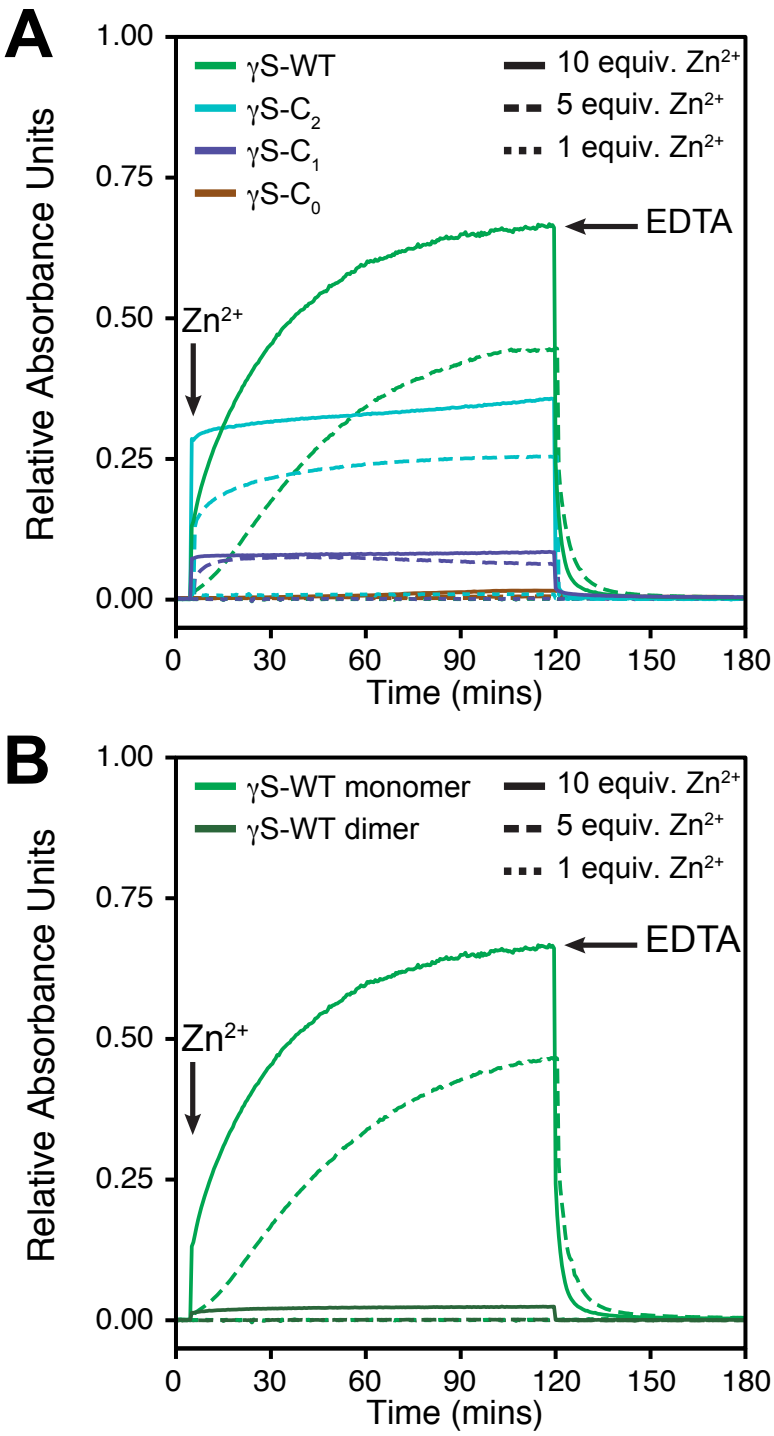

Figure 2.7: Treatment of human γS-crystallin and its cysteine-to-serine variants with 1 (small dashed lines), 5 (long dashed lines) or 10 (solid lines) equivalents of Zn^{2+}. (A) Light scattering of monomeric HγS wild-type (green), HγS-C_2 (cyan), HγS-C_1 (purple), and HγS-C_0 (brown). (B) Light scattering of monomeric HγS (green) and dimeric HγS (dark green). The HγS wild-type dimer was collected from the protein purification process without further modification.

For these two variants, the extent of aggregation is considerably reduced despite a higher ratio of Zn^{2+} to solvent-accessible cysteines.

In addition to Zn^{2+}, we also observed Cu^{2+}-induced aggregation of HγS. The addition of 1 equivalent of Cu^{2+} produced considerable levels of aggregation for HγS-WT and each Cys-to-Ser variant (Supplementary Figure S9), to the extent that precipitation occurred. The dimer of HγS-WT exhibited similar total aggregation under the same conditions. Prior investigations of γD-crystallin have shown that the solvent-accessible residues C109 and C111 are primarily responsible for Cu^{2+}-induced aggregation, which can be blocked using GSSG. [60] ^{1}H-^{15}N HSQC peak intensity disappearances in HγD prepared with Cu2+ provide further evidence that the strongest interactions occur at the solvent accessible-cysteines.[39] We felt confident that the removal of the solvent-accessible cysteines in γS-crystallin, which we observed led to decreased Zn^{2+}-induced aggregation, would have a similar effect for Cu^{2+}. However, this hypothesis proved to be incorrect. In contrast to Zn^{2+}, the removal or reduction of solvent-accessible cysteine side chains does not strongly impact Cu^{2+}-induced aggregation, although the scattering intensity of all samples is decreased upon EDTA addition, suggesting that superficial cross-linking is partially responsible. No changes in protein structure are evident upon the addition of either Cu^{2+} or Zn^{2+} for HγS-WT based on far-UV circular dichroism (Supplementary Figure S10).

To further investigate the mechanism of Cu^{2+}-induced aggregation, we digested the insoluble aggregates of HγS-WT and HγS-C_0 with trypsin to search for oxidative PTMs or modifications observed in aged lenses via mass spectrometry (Supplementary Table S8, Supplementary Figure 11).The light-scattering samples of HγS and HγS-C_0 incubated with 10 equivalents of Cu^{2+} were analyzed via mass spectrometry to determine if post-translational modifications (PTMs) were present. Trypsin digests were performed using the HγS-WT and HγS-C_0 pellets collected via centrifugation with MSMS mapping to confirm PTMs. Mass shifts of +16 Da and +32 Da (corresponding to cysteine oxidation) for peptides containing

C23, C25, C27, and C115 were the only modifications investigated from the HγS-WT digest. Across several measurements, MSMS mapping of modification showed C25 was the most consistently modified of the C23-C25-C27 triad. Digests of γS-C_0 produced fewer detectable mass shifted peptides. The observed shifts of +16 Da were observed for 2 peptides, corresponding to oxidation of M59 and M124. Why these two methionines are more readily oxidized than M74, M108 or M119 is yet unclear, given that the latter residues all have a larger solvent accessible surface area. We speculate that local electrostatics are involved, however, further investigation is required.

Functional characterization of the interactions of *Ci*-$\beta\gamma$ is highly relevant to understanding its role in the tunicate sensory vesicle. This structure, which contains both the ocellus and the otolith, is highly enriched in several metal cations, including Ca^{2+} and Zn^{2+} as a means of controlling its specific gravity.[45] We previously reported that the fluorescence intensity of *Ci*-$\beta\gamma$ changes in response to Ca^{2+} binding, therefore, a preliminary analysis of fluorescence intensity changes was performed using Mg^{2+}, Sr^{2+}, Mn^{2+}, Co^{2+}, Ni^{2+}, and Zn^{2+} (Supplementary Figure S12). The changes in *Ci*-$\beta\gamma$ fluorescence intensity were comparable to those observed upon binding Ca^{2+}, prompting us to continue with thermal unfolding and aggregation measurements. Interestingly, thermal aggregates of *apo-Ci*-$\beta\gamma$ do not form until 60 °C, despite its thermal unfolding midpoint of 46 °C. The addition of divalent cations reverses this trend, resulting in a 10-15 °C lower T_m than T_i (Figure 2.5, Table 2.2). The persistence of this trend, independent of the degree of thermal stabilization, suggests that the underlying interactions of *Ci*-$\beta\gamma$ with different divalent cations are highly similar. Further, the difference in aggregate size between *apo-Ci*-$\beta\gamma$ ($<$ 50 nm) and cation bound *Ci*-$\beta\gamma$ ($>$1000 nm) suggests that increased structural rigidity may alter the aggregation pathway.

2.4 Conclusion

The double clamp motif of the $\beta\gamma$-crystallin domain is capable of binding to a broad range of divalent cations beyond Ca^{2+}. This functionality is aided by the absence of readily oxidizable and cation-coordinating residues such as cysteine, histidine and methionine. In contrast, vertebrate lens γ-crystallins, which mostly do not bind divalent metal cations, are structurally similar but compositionally different. Notably the amino acid composition of the lens γ-crystallins favor more refractive residues, and their sequences were apparently not shaped by selective pressure against cysteines. In human γS-crystallin, solvent-exposed cysteine residues increase susceptibility to Zn^{2+}-induced aggregation through cross-linking, whereas Cu^{2+}-induced aggregation is driven by methionine oxidation.

Chapter 3

Copper-induced aggregation of human γS-crystallin involves multiple mechanisms

3.1 Introduction

The eye lens is a unique organ due to its optical transparency and minimal metabolic activity. In addition to a thin exterior layer of epithelial cells, the lens is made of elongated fiber cells which enucleate and lose their cellular organelles during maturation in order to eliminate light scattering. This process removes the cellular machinery necessary for protein turnover, thus, lens proteins are not replaced during an organism's lifetime. In human lens fiber cells, protein concentrations range to upwards of 400 mg/mL [136]. 90 % of lens proteins belong to the α-, β-, and γ-crystallin families. The α-crystallins are small heat-shock proteins that function as holdase chaperones. The β- and γ-crystallins are structural proteins evolved for high refractivity and fluorescence quenching. Both β- and γ-crystallins contain two

domains connected via a linker sequence and a hydrophobic interface. Each domain contains a double Greek-key motif in which two sets of four antiparallel β-strands create a β-sandwich structure.

The lens crystallins are extremely long lived proteins (ELLPs) that are consistently exposed to ultraviolet radiation, which can cause structural damage. Consequently, the β- and γ-crystallins have evolved efficient fluorescence quenching capacity through conserved structural features and FRET interactions between the two highly conserved, buried tryptophans in each domain [25, 137, 26]. The lens environment also contains high levels of glutathione and other antioxidants that serve as redox buffers [138]. Despite these features, post-translational modifications (PTMs) accumulate over time [89, 90]. An array of PTMs are observed in both the soluble and insoluble fractions of aged lenses and are suspected to facilitate protein aggregation [139, 140].

In many cases, the molecular-level details of how PTMs enable aggregation remains unclear. Two modifications of significant interest are deamidation and oxidation. Deamidation is the most commonly observed modification and may occur in parallel racemization or isomerization [90, 141, 142]. Oxidation is arguably the second most common PTM and is thought to accumulate with age as lens antioxidant levels decrease. Mass spectrometric identification of aged lens γ-crystallin has evidenced oxidative damage to numerous residues, focally methionine, histidine, tryptophan and cysteine [89, 143]. Although the lens is regularly exposed to UVA (0.116 – 0.99 mW cm^{-1}) and UVB (1.2×10^{-4} – 4.4×10^{-4} mW cm^{-1}) radiation [144] [1], the formation of reactive oxygen species (ROS) may also be catalyzed by metal ions found in the lens.

Copper and zinc ions in the lens serve as cofactors for the chaperone α-crystallins but are released upon substrate binding [59]. Whether this release contributes to a negative feedback

[1] Ranges represent 2% – 17% impingement of solar radiation in summer at 40°N applied to data for UVB (295 – 315 nm) and UVA (315 – 400 nm) light.

cycle is currently unknown; however, elevated of Cu^{2+} concentrations have been reported in cataract lenses [63, 145, 146]. This may also be a feature of diabetes[62] and smoking[147] but is difficult to directly measure. Although the concentration of lens Zn^{2+} is several times higher than Cu^{2+} [148], copper ions readily produce ROS and induce γ-crystallin aggregation at lower equivalencies [149]. The molecular mechanisms of aggregation due to copper and associated ROS are poorly understood but are also possibly relevant in other protein aggregation diseases such as Alzheimer's, Parkinson's, and Huntington's [150, 151]. The specific interactions with copper ions depend on the structure and function of the protein. Some disease-related proteins like α-synuclein [152, 153], β-amyloid[154, 155], and ubiquitin[156] aggregate in the presence of copper, whereas in prion [157] and tau [158], aggregation is inhibited.

Previous solution-state nuclear magnetic resonance (NMR) studies of γD-crystallin suggest that the strongest copper interactions occur at sites where with at least two proximal cysteines or histidines [39]. We previously reported that divalent cations of zinc, nickel, and cobalt drive γS-crystallin aggregation through intermolecular bridging via cysteines, whereas copper-induced aggregation occurs even in the absence of solvent-accessible cysteines [149]. Investigating the mechanistic pathways of Cu^{2+}-mediated aggregation of γS-crystallin is of particular interest for multiple reasons. γS is highly expressed in the lens epithelial and cortical fiber cells[159], while γC and γD – the other highly expressed γ-crystallins – are primarily concentrated in the lens nucleus[160, 161]. The accumulation of copper in the lens may therefore impact γS before other γ-crystallins, leading to protein damage and cataract. Further, γS-crystallins contain a unique cysteine tetrad. Three of the cysteines, C23, C25, and C27, are highly solvent accessible and within disulfide bonding distance of one another. The fourth cysteine, C83, is located on an adjacent β-strand, within hydrogen-bonding distance of C27. Although no function is known for this tetrad, γ-crystallins have been observed to have an oxidoreductase-like property where intramolecular disulfides are transferred between proteins [104]. It has been proposed that continual transfers amongst

the highly concentrated γ-crystallins may act as a final redox buffer. Since the cysteines of γS are the most solvent exposed and highest density cysteines in the γ-crystallin, they may serve as a sink for any disulfide transfer mechanism in the lens.

In order to better understand the aggregation pathways of γS-crystallin, we have investigated Cu^{2+}-mediated aggregation alongside UV-induced aggregation and amino acid point mutations implicated in hereditary cataract. UV irradiation drives ROS formation, but the extent to which oxidative modifications from UV- and copper-induced aggregation are similar is unknown. In contrast, genetic mutations that cause aggregation may or may not proceed through similar mechanistic pathways than copper-induced aggregation. Comparative measurements can therefore provide insight into how copper-induced aggregates may resemble or differ from cases in which the underlying cause of aggregation is known. Here we show that Cu^{2+}-induces aggregation through intermolecular bridging, disulfide bond formation, and covalent crosslinking. These aggregates are distinct from UV-induced and cataractous point mutants with respect to their biophysical stability. Copper binding occurs at two or more sites, with cysteine coordination buffering the effects of Cu^{2+}-induced aggregation.

3.2 Materials and methods

3.2.1 Protein Expression and Purification

The human γS-crystallin variants γS-G18V, γS-D26G, and γS-V42M, and γS-C23S-C25S-C27S-C115S (γS-$_0$) were made using site-directed mutagenesis of the wild-type (γS-WT) construct containing an N-terminal 6$\times$ His tag and a TEV cleavage sequence (ENLFQG) which leaves a glycine in place of the start methionine. The genes encoding each protein were cloned into a pET28a(+) vector (Novagen, Darmstadt, Germany) and overexpressed in a Rosetta *E. coli* cell line (DE3) using Studier's autoinduction protocol [87]. Cell pellets

were collected via centrifugation at 4,000 rpm for 30 minutes, resuspended, lysed, and respun at 14,000 rpm for 60 minutes. Each protein was purified via nickel affinity chromatography, digestion with TEV protease (produced in-house), subsequent nickel affinity chromatography, and finally, two separate size exclusion chromatography (SEC) runs on a GE Superdex 75 10/300 (GE Healthcare, Pittsburgh, PA) to ensure pure monomeric protein. All samples were dialyzed into 10 mM HEPES, 50 mM NaCl, pH 7 unless otherwise stated. Prior to measurement, proteins were reduced using 5 mM fresh dithiothreitol (DTT) and dialyzed. Analytical size exclusion Cu^{2+}-treated samples were measured using a GE Superdex 75 Increase 10/300 GL (GE Healthcare, Pittsburgh, PA).

3.2.2 UV-A Induced Aggregation

Protein solutions at 6 mg/mL (2.5 mL) or 100 mg/mL (1.5 mL) were irradiated with 355 nm light generated using a 10 Hz Nd:YAG laser (Continuum Surelite II; Surelite, San Jose, CA, USA) coupled to a Surelite Separation Package (SSP) 2A (Surelite) to change the pump laser wavelength (1064 nm) via third harmonic generation (laser flux was 29 mJ/cm^2 at 10 Hz). The solutions were continuously stirred and kept between 22 °C and 24 °C using a Quantum Northwest Luma 40/Eclipse with a Peltier element and recirculator (Quantum Northwest Inc., Liberty Lake, WA, USA). Samples were irradiated for 180 minutes.

3.2.3 UV-B Induced Aggregation

Aggregation of 6 mg/mL or 100 mg/mL γS-crystallins via 278 nm UVB radiation was accomplished using two 70mW light emitting diodes (LEUVA66H70HF00, Seoul, Korea) at 5 mm distances (120 degree view angle) yielding a mean power density of 58 mW/cm^2. Samples used for TEM and FTIR measurements irradiated for 30 minutes. Mass spectrometry and resolubilization assays were irradiated for 90 minutes.

3.2.4 Absorbance

Resolubilization assays were performed by adding 200 μL of copper (II) chloride stock solutions to 200 μL of protein to achieve final solutions of 50 μM protein varying molar equivalents of Cu^{2+}. Samples were incubated at 25 °C for 8 hours and then left at 4 °C overnight prior to measurement. Samples were then spun at 6000 rpm for 20 minutes, and the supernatant was carefully removed so as to not disrupt any pelleted aggregates. Aggregates were resuspended in 400 uL of buffer with 10 mM ethylenediaminetetraacetic acid (EDTA), vortexed, incubated at 37 °C for 30 minutes, sonicated for 15 minutes, and respun at 6000 rpm. This procedure was then repeated with the addition of dithiothreitol (DTT) for a final concentration of 5 mM (2 μL of 1 M DTT). EDTA and DTT treatments were also applied to the initial soluble samples following measurements. Absorbances were measured using a NanoDrop2000. Three samples were prepared for each concentration and each sample was measured in triplicate. Final absorbance values were corrected for dilution.

3.2.5 Fluorescence

All fluorescence measurements were performed using a Varian Cary Eclipse fluorescence spectrophotometer. Changes in the intrinsic fluorescence were measured for 1000 μL of 50 μM protein samples by adding 10 μL of a copper (II) chloride stock solution. Samples were excited at 280 nm and emission spectra collected from 300 nm to 400 nm. Absorbance spectra were measured after each Cu^{2+} addition to ensure that observed differences were not due to protein deposition.

The tryptophan fluorescence was measured for γS-WT and γS-C_0 by using a 295 nm excitation to minimize tyrosine and phenylalanine absorbance. The samples were collected from the aggregation recovery and diluted to a concentration of 5 μM with emission measured from 310 nm to 500 nm. Each sample was also tested for dityrosine fluorescence using a 320

nm excitation and 330 nm to 500 nm emission.

Hydrophobic surface exposure was measured using μM 8-Anilinonaphthalene-1-sulfonic acid (ANS). Samples were prepared at final concentration of 50 μM with 750 μM ANS (based on previous work [134]) and allowed to incubate at room temperature for one hour. Fluorescence spectra were measured from 450 nm to 600 nm with an excitation of 390 nm, using 20 nm slit widths.

3.2.6 Fourier-transform infrared spectroscopy (FTIR)

Aggregates of γS-G18V, γS-D26G, and γS-V42M were collected from samples stored at 5 mg/mL at 4 °C for several weeks. All aggregates and soluble protein were separated via centrifugation and lyophilized. Samples were then resuspended in D_2O for 24 hrs and lyophilized again. Measurements of all powders were made using a Jasco FT/IR-4700-ATR-PRO ONE (JASCO, Easton, MD) over the 400-4000 cm^{-1} range with 4^{-1} resolution. Data from 1700 cm^{-1} to 1475 cm^{-1} normalized to peak amide I band absorbance.

3.2.7 Mass Spectrometry

Irradiated samples of γS-WT were centrifuged at 13000 x g for 15 minutes and the insoluble portion was redissolved in 50 μL of 8 M urea, 1 M ammonium bicarbonate. A control samples of unexposed γS-WT was prepared identically and concentrated to reach 12 mg/mL. All samples were sonicated for 5 minutes in pulses of 20 seconds on and 10 seconds off. The samples were then diluted to 0.5 mg/mL protein concentration and to a buffer concentration of 1.6 M urea, 1 M ammonium bicarbonate. The intact protein mass was collected to confirm that any observed post-translational modifications did not arise from the denaturation procedure. 3 μg of trypsin was then added, and samples were incubated overnight at 37 °C.

The samples were then diluted to 0.2 mg/mL with water, treated with 10 μL of 100 mM DTT, and heated to 80 °C for 3 minutes. Mass spectra were collected on a Waters Xevo XS-QTOF over 30 minutes on a C4 column with a 0 – 100 gradient solvent B (solvent A: 100% 0.1% formic acid in water, solvent B: acetonitrile). The data analysis was performed in BioPharmaLynx. Native and modified peptides were confirmed with MS/MS spectra and quantified by ion count. For each sample, (unexposed, UVA-exposed, and UVB-exposed), the experiment was performed in triplicate.

3.2.8 SDS-PAGE

γS-WT (200 μL total volume, 150 μM) was aggregated using 0.1, 0.2, 0.4, 0.6, 0.8, 1, 1.5, 2, 3, or 5 equivalents of Cu^{2+} at 25 °C for 4 hours and then left at 4 °C overnight. The samples were then centrifuged, and the supernatant was removed without disturbing the pellet. Prior to loading, 10 μL of protein was mixed with 10μ of loading dye (62.5 mM Tris-HCl, 2% sodium dodecyl sulfate, 25% glycerol, 0.01% bromophenol blue, pH 6.8), 1 μL 2-mercaptoethanol, 1 μL of EDTA (final concentration 1 mM) and heated at 70 °C for 90 seconds. Samples were run on 12% Mini-Protean TGX gel at 115 V for 85 minutes and stained using Coomassie blue. Each gel was run at least twice to ensure reproducibility.

3.2.9 Transmission electron microscopy

The morphology of the γS-crystallin aggregates formed subject to acidic buffer, UV irradiation, and metal ion treatment were investigated by transmission electron microscopy (TEM). Negatively stained samples for TEM were prepared on commercial Carbon-coated 400 mesh Copper grids (Plano GmbH, Wetzlar, Germany). The grids were made hydrophilic by glow discharge treatment, whereupon 2 μL of sample solution was applied and allowed to soak for 45 seconds before blotting. The grids were then rinsed twice with 50 μL deionized water,

followed by blotting. Negative staining was performed by applying 4 μL of a 1 percent uranyl acetate solution, followed by immediate blotting. Application of 4 μL of uranyl acetate was then repeated; this time being allowed to soak for 20 seconds before a final blotting step. TEM micrographs were then recorded in a JEOL JEM 2100 instrument with an accelerating voltage setting of 120 kV.

3.3 Results and Discussion

3.3.1 Cu^{2+}-damaged γS-crystallin aggregates differ from point variant and UV-induced aggregates

Crystallin aggregates taken from cataract lenses are characterized as amorphous, indicating a lack of identifiable structure. Likewise, the extent to which whole lens aggregates exemplify the underlying cause of aggregation is unknown. Here we investigated aggregates from γS-crystallin *in vitro* using several different methods in order to probe for potential characteristic features. We began our investigation by comparing the morphology of γS-crystallin aggregates resulting from point mutations, UV-irradiation, and Cu^{2+} treatment. Transmission electron microscopy was used to image aggregates of γS-G18V, γS-D26G, and γS-V42M formed by allowing them to incubate for several months at 4 °C (Figure 3.1A-C). For each variant, larger aggregates are composed of smaller, globular particles roughly 20 nm in diameter on average (SI Figure 1). The clustering of smaller, component aggregates observable in each case is similar to that observed for γD-P23T [162]. The similarity observed here does not explicitly inform the us about underlying mechanism of aggregation for each mutation but is interesting nonetheless as the D26G mutation – in which the only major change is a surface salt bridge [163] – is considerably different from G18V and V42M, both of which cause more substantial structural changes[164, 85].

Micrographs of γS-crystallin were taken following UVA and UVB irradiation (Figure 3.1D-E). While UVA and UVB are both capable of ROS formation, UVB is more effectively absorbed by aromatic residues, focally tryptophan, which acts to help quench fluorescence in the γ-crystallins[137]. Irradiation at both wavelengths produces aggregates that are similar in size to point mutant aggregates and lack a well-defined morphology. To ensure that the UV aggregates were representative, we varied the concentration and irradiation times of the samples to assess potential differences. In all cases, once formed, the size and morphology of the aggregates did not appear to exhibit any clear differences (SI Figures 2-3). Likewise, photodamaged point mutants also show distinct, small component aggregates of the same size even when densely clustered (SI Figure 4).

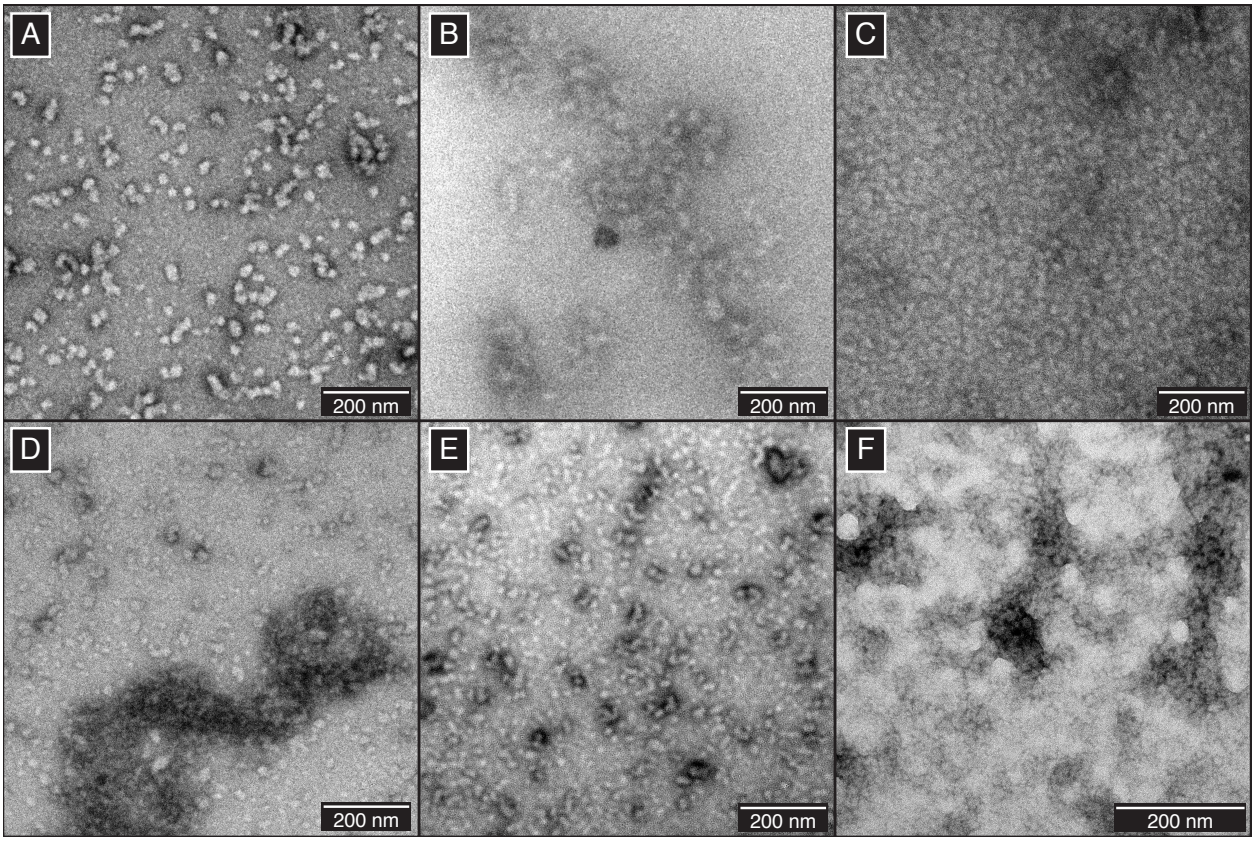

Figure 3.1: TEM micrograms of γS-crystallin aggregates. Native aggregates of γS-D26G (A), γS-G18V (B), and γS-V42M (C). Photodamaged aggregates form using UVA (D) or UVB (E) radiation. Aggregates resulting from the treatment of 0.5 equivalents of Cu^{2+} (F).

As observed for point mutants and UV irradiated samples, no consistent, distinctive mor-

phological features were observable for Cu^{2+}-induced aggregates (Figure 3.1F). This result is consistent with observations of Cu^{2+}-induced aggregates of γD-crystallin [39]. In order to probe for differences that would enable investigation of specific aggregation pathways, we probed the structure of the resulting aggregates via FTIR. The amide absorption frequencies of protein secondary structures differ from one another; therefore, one can infer changes in protein structure by comparing the amide I and II bands between samples. The amide I band largely results from C=O stretching vibration, while the amide II band is mainly composed of the N-H bending vibration and C-N stretching vibration. Between the soluble and aggregated mutant γS-crystallins, minimal changes were observed to the amide 1 band line shape, suggesting that an overall β-sheet structure is retained for each of the solid aggregates (SI Figure 5). Likewise, the changes observed following UVB irradiation or treatment with Cu^2+ are also minimal. Interestingly, the relative absorption of the amide I peak to amide II peak decreases for all aggregates, as well as the soluble UVB and Cu^{2+}-treated species. We suspect this change is possibly the result of minor conformational changes; however, no specific changes can be readily determined from this method alone.

We next turned to potential changes in hydrophobic surface exposure in order to better understand the effect of Cu^{2+} treatment. Cataract-causing point mutations serve as convenient references, as increased hydrophobic surface exposure can result from mutations within the hydrophobic core[165, 166] or on the protein surface [85, 167] but is not necessary for aggregation. We investigated changes in hydrophobic surface exposure of γS-crystallin following Cu^{2+} and UVB treatment using ANS, a small molecular probe that fluoresces strongly when coordinated to a protein through electrostatic and hydrophobic interactions [168]. Soluble γS-WT from Cu^{2+} treatment has a similar ANS fluorescence spectrum to that of γS-D26G (Figure 3.2), for which no structural changes are known. The spectra have minimally greater intensities than γS-WT. In contrast, the two point mutants with known increases hydrophobic surface exposure, γS-G18V and γS-V42M, show considerable increases in ANS fluorescence intensity.

Interestingly, UVB-exposed γS samples exhibit the greatest fluorescence, with an intensity more than twice γS-V42M. While UV irradiation and free copper can both catalyze ROS formation, the differences in ANS fluorescence suggest the two methods drive aggregation rather differently. While larger changes in hydrophobic surface exposure may occur for UVB due to the oxidation of the internal tryptophan residues, the lack of hydrophobic surface exposure following Cu^{2+} treatment suggests a highly efficient precipitation of modified or an alternative mechanism such an intermolecular bridging that occurs for other transition metals.[**?**]

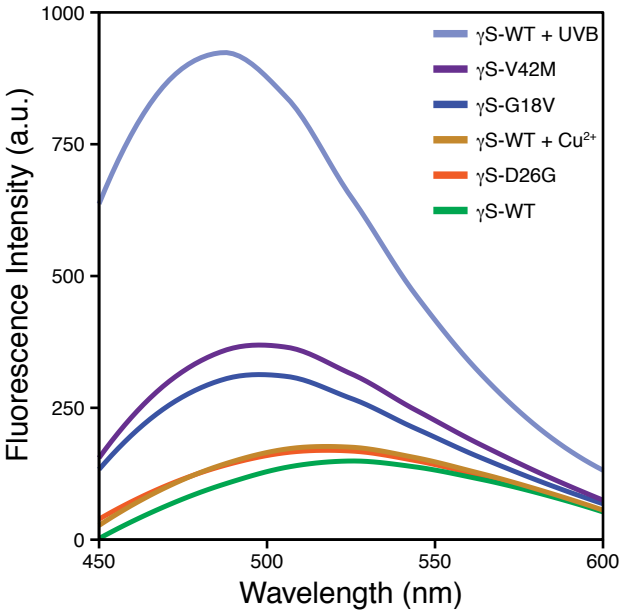

Figure 3.2: Fluorescence spectra of ANS binding to γS-crystallins. 50 μM of soluble protein was incubated with 750 μM of ANS in order to probe changes in hydrophobic surface exposure. UVB irradiation produces considerable hydrophobic exposure. The soluble γS-WT remaining after Cu^{2+} addition yields minimally changes relative to γS-WT. Point mutant ANS fluorescence changes are consistent with previous reports.

3.3.2 Cu^{2+}-induced aggregates are composed of different species

The presence of transition metals, notably zinc, can drive aggregation through intermolecular bridging. We previously observed in γS-crystallin that this bridging is abolished by the

removal of solvent-accessible cysteines for all but Cu^{2+}, in which cysteine removal accelerated aggregation [149]. In order to systematically evaluate the effect of Cu^{2+}, we began by investigating the aggregation of γS-WT and the γS-C_0 variant in which the four solvent accessible cysteines (C23, C25, C27, and C115) were mutated to serine. Consistent with our previous results, γS-WT aggregates to a lesser total extent than γS-C_0 (Figure 3.3A-B). In order to quantify aggregative factors, we treated insoluble Cu^{2+}-induced aggregates with excess EDTA (10 mM) to recover protein precipitated through intermolecular bridging. Both proteins show comparable amounts of recovery relative to the amount of insoluble aggregate formed (Figure 3.3C). Subsequently, we resuspended the remaining aggregates in the presence of DTT (5 mM) in order to disrupt potential disulfide crosslinks contributing to aggregation (Figure 3.3D). Unexpectedly, we observed resolubilization of both proteins. While a disulfide trapped fold is possible, we suspect the thiol character of DTT may allow it to chelate protein-bound copper more effectively than EDTA, as the reported binding affinity of DTT for Cu^{2+} (K_D 10^{-15} M at pH 7)[170, 171], is lower than EDTA (K_D of $10^{-18.8}$ M)[172]. The ability of a second, different chelating agent to resolubilize aggregates suggests that the process of Cu^{2+}-induced aggregation may occur though at least two mechanisms and may involve binding to at least two sites. In addition to intermolecular bridging and intermolecular disulfide bonding, we suspected that the tightly bound copper may induced structural modifications leading to an additional aggregation pathways.

Analysis of the resolubilized proteins was performed via fluorescence and circular dichroism (CD) in order to probe for structural changes. Tryptophan fluorescence is a sensitive measure of minor structural perturbations in γS-crystallin, as the two buried tryptophans of each domain act to effectively quench fluorescence. Therefore, minor structural changes are observable through red shifting – resulting from a more polar environment – and increased fluorescence peak intensity. We used samples from the treatment of 2 equivalents of Cu^{2+}, as the most similar protein concentrations were present across each treatment group. Soluble γS-WT and γS-C_0 after Cu^{2+} treatment exhibited reduced fluorescence intensity but

similar peak intensity near 330 nm (Figure 3.4A-B), with appreciable shouldering for γS-C_0. In contrast, resolubilized γS-WT from EDTA treatment exhibited peak broadening and red shifting while γS-C_0 showed dramatically increased fluorescence intensity in addition to red shifting. DTT resolubilized proteins resembled their respective soluble fractions, with γS-C_0 showing reduced fluorescence intensity. We attribute the reductions in fluorescence intensity for each of the treated samples to interactions with Cu^{2+} (Figure 3.4C). γS-WT is quenched more than γSC_0, which suggests the solvent accessible cysteines of γS-WT – C23, C25, and C27 – that are proximal to W47 may be a binding site.

The extent of unfolding for soluble and resolubilized proteins was assessed via the 355/325 fluorescence ratio. Soluble and DTT resolubilized γS-WT and γS-C_0 were minimally altered. The fluorescence ratio of EDTA resolubilized proteins increased from 0.57 to 0.78 for γS-WT and from 0.59 to 0.96 for γS-C_0. Both changes are non-trivial; the ratio for EDTA resolubilized γ-C_0 is comparable to the first unfolding transition observed in γS-G18V[124], γS-S39C[95], and γS-V42M[165] due to guanidinium hydrochloride, which is assumed to correspond to the partial unfolding of the N-terminal domain.

We subsequently measured the CD spectra for all samples to evaluate whether large-scale unfolding contributes to Cu^{2+}-induced aggregation. The CD spectrum of γS-WT exhibits a minimum at 218 nm, indicative of high β-sheet character, consistent with the solution-state NMR structure [85]. Soluble and DTT-resolubilized γS-WT after Cu^{2+}-treatment show a similar minimum at 218 nm, but with considerable broadening towards 212 nm. The spectrum of DTT-resolubilized γS-WT is reduced in intensity and shows distinct minima at 218 nm and 212 nm. As observed via fluorescence for γS- and γD-crystallin, the reduction in signal suggests that some Cu^{2+} may still be bound to the γS-WT [39]. The spectrum of γS-C_0 resolubilized using DTT resembles the untreated control, whereas the soluble protein is similar in shape, but considerably reduced in intensity. The minimum of EDTA-resolubilized γS-C_0 appears at 212 nm, similar to that of EDTA-resolubilized γS-WT, as well as a distinct

minimum near 200 nm, indicative of random coil character.

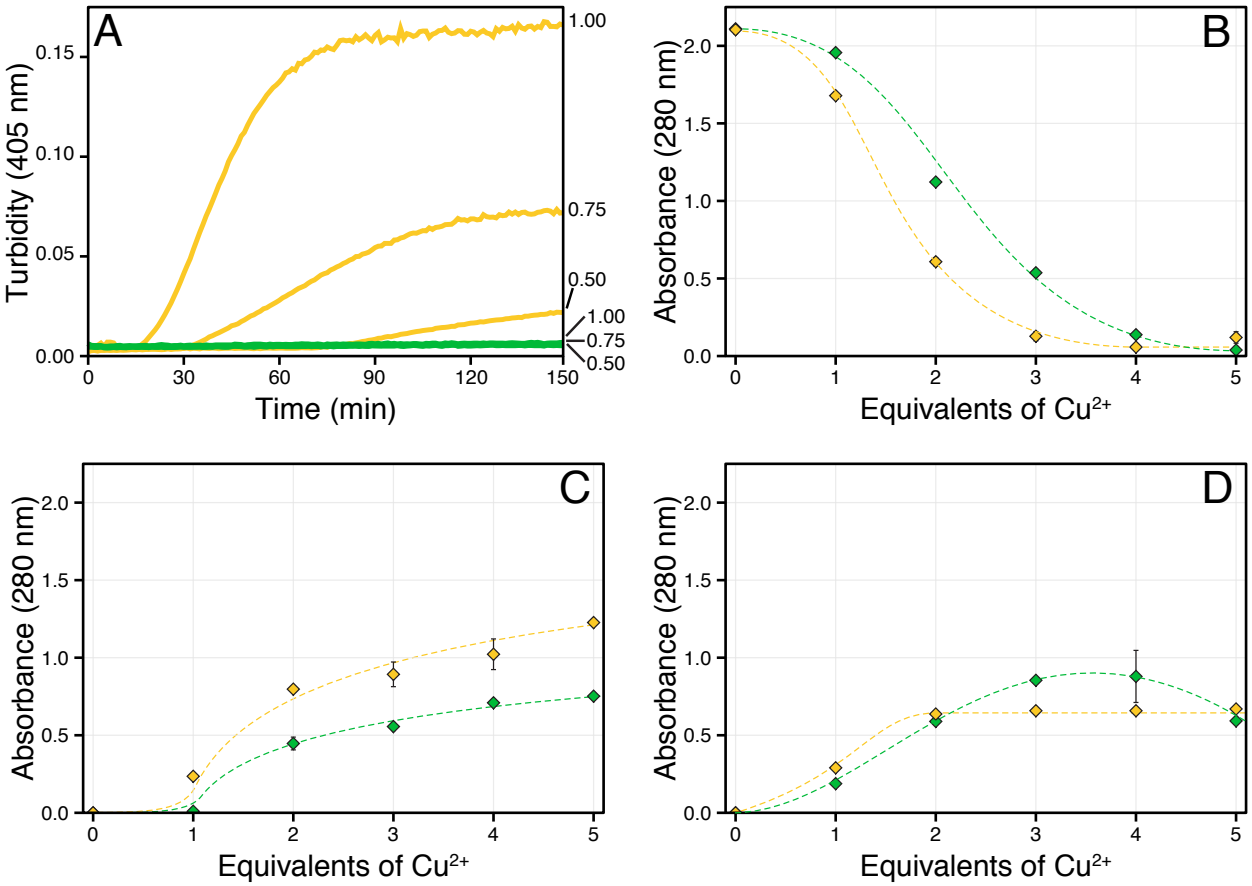

Figure 3.3: The 280 nm absorbance of γS-WT (green) and γS-C_0 (gold) was measured following Cu^{2+} addition. (A) Aggregation kinetics of γS-WT (green) and γS-C_0 (gold) following the addition of 0.5, 0.75, or 1 equivalent of Cu^{2+} (listed on right). After 150 minutes, no turbidity was observed for γS-WT, whereas the onset and extent of γS-C_0 turbidity increased with Cu^{2+} concentration. (B) Absorbance of the supernatant following centrifugation. (C) The absorbance of proteins resuspended from Cu^{2+}-induced aggregation via EDTA. (D) The absorbance of proteins resuspended from Cu^{2+}-induced aggregation via DTT. Error bars represent one standard deviation. The added lines are meant to serve as a visual guide.

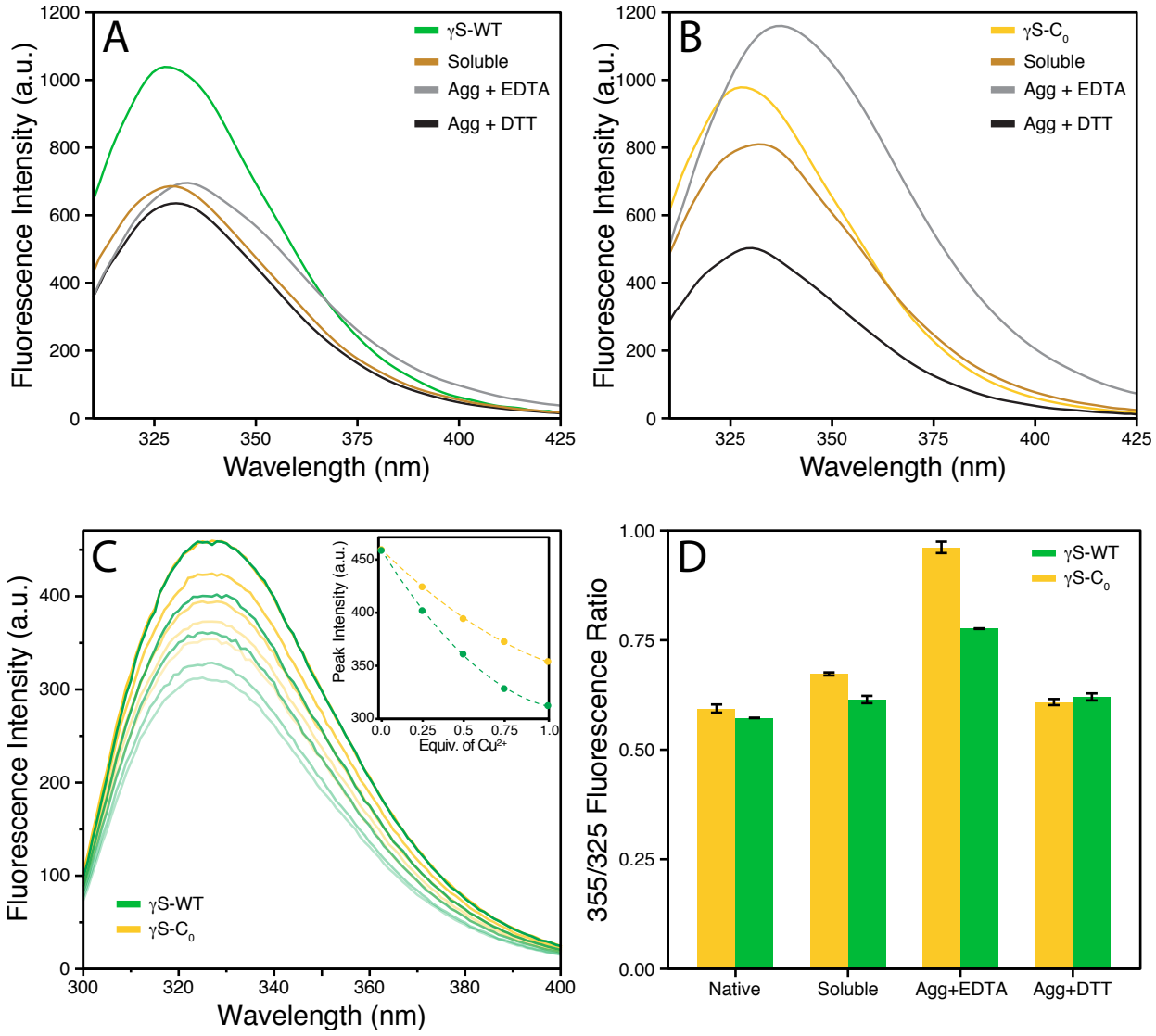

Figure 3.4: Fluorescence of soluble and aggregate γS-WT and γS-C_0 after incubation with 2 equivalents of Cu^{2+}. (A) Untreated and Cu^{2+}-incubated samples of γS-WT. (B) Untreated and Cu^{2+}-incubated samples of γS-C_0. (C) The 355 nm over 325 nm fluorescence intensity ratio for each of the samples measured in parts (A) and (B). Error bars represent one standard deviation. (D) Fluorescence spectra of γS-WT (green) and γS-C_0 (pink) in the presence of 0, 0.25, 0.5, 0.75, and 1 equivalent of Cu^{2+}. Increasing transparency translates to higher concentrations of Cu^{2+}. The fluorescence intensity of γS-WT decreases more rapidly than γS-C_0 when incubated with increasing equivalents of Cu^{2+} (inset).

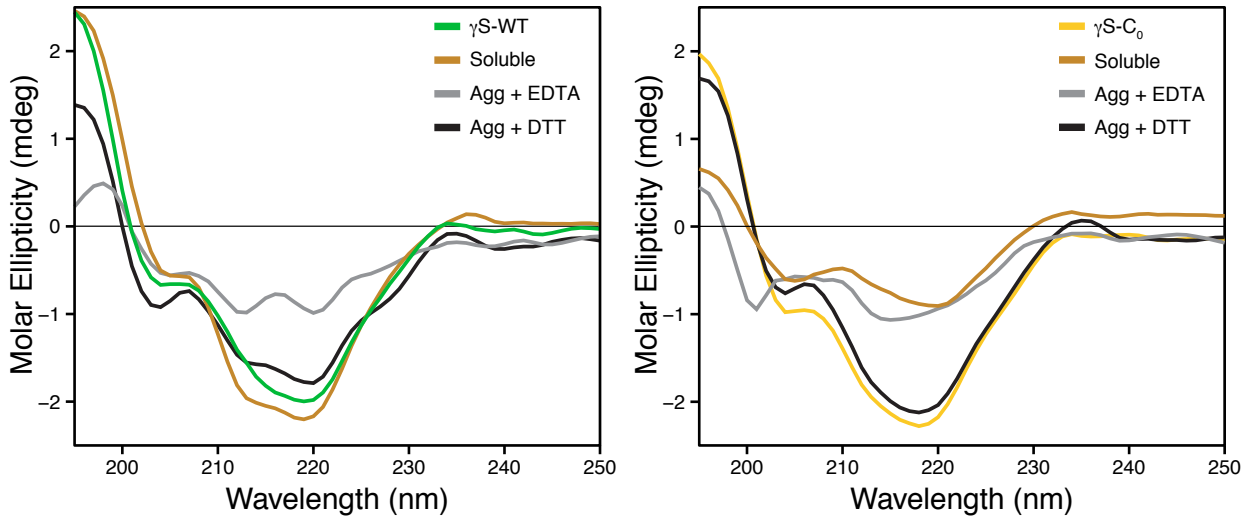

Figure 3.5: Circular dichroism of soluble and aggregate γS-WT and γS-C_0 after incubation with 2 equivalents of Cu^{2+}.

3.3.3 Covalent modifications alter γS-crystallin behavior

While resolubilization of aggregates was possible via DTT and EDTA, whether factors such as covalent crosslinking also contribute to Cu^{2+}-induced aggregation necessitated further investigation. To start, we measured the distribution of soluble and resolubilized γS-WT and γS-C_0 sizes via analytical SEC (SI Figure 7). For each γS-WT sample, increasing size resulted in lower abundance, with a clear predominance of monomers. γS-C_0, with the exception of the EDTA resolubilized sample in which the dimeric elution peak was the most populated. The presence of non-monomeric species suggested to us that crosslinkings may also be involved in driving aggregation.

We next analyzed the dimeric weight range peaks for the EDTA resolubilized proteins via UPLC-MS on a C4 column (Figure 3.6) Multiple peaks were present in both the γS-WT and γS-C_0 traces, allowing us to perform independent mass reconstructions. For both proteins the first peak contained a shoulder with an earlier elution and mass consistent with m+16 mass likely corresponding to a single oxidation while the main peak contains the parent mass. The later eluting peak of γS-WT was split in two. The reconstruction resolution of the earlier part of the second peak was limited by poor signal to noise but indicated the parent mass and an m+164 species to be present. The latter half of the second peak was more well resolved, reconstructing a m+221 mass. Likewise, the second peak of γS-C_0, which eluted at the same time as the latter half of the second γS-WT peak, also contained an m+221 peak as well as an m+329 peak.

Analytical SEC measurements of γS-WT were also made for samples treated with substoichiometric equivalents of Cu^{2+} and subsequently with excess EDTA. The monomeric peak of the untreated γS-WT (U) decreases and is split into left (L) and right (R) peaks at roughly the same elution time after Cu^{2+} treatment (Figure 3.7A). The mass reconstruction of both peaks show oxidation and dimerization is present, with a high extent of dimerization

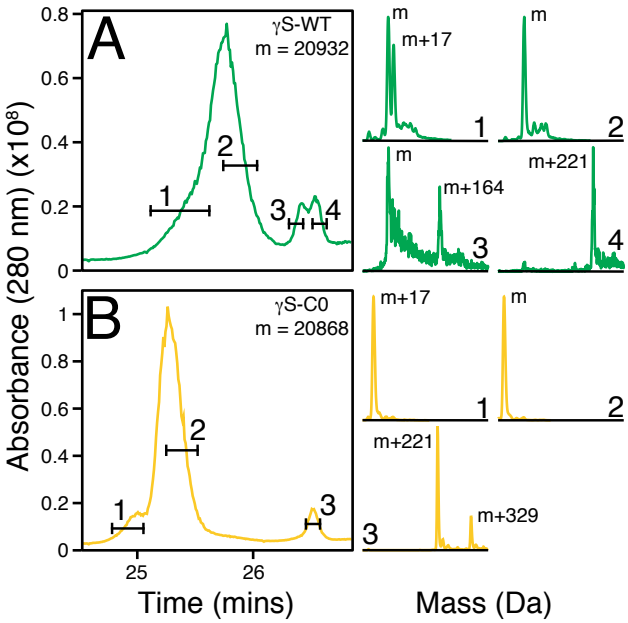

Figure 3.6: The dimer peaks of γS-WT (A) and γS-C_0 collect following analytical SEC were analyzed through separation on a C4 separation prior to mass spectroscopy. Two distinct peaks are visible for both proteins, with shouldering or splitting present for most peaks. The selected time frames drawn across the chromatographic traces correspond to the data used for the corresponding mass reconstructions.

present in the right peak (Figure 3.7B). A portion of the dimerization and higher molecular weight species observed from Cu^{2+} addition are likely attributable to disulfide bridging as the monomeric species almost exclusively present after reduction with DTT. Critically, the mass reconstructed for the left and right peaks are 2-3 Da lower than the observed γS-WT for mass, and do not change following reduction. We suspected that this was due to an intramolecular disulfide bond, as the soluble fraction of γS-C_0 does not exhibit the same mass shift.

In order to further probe the sensitivity of γS-WT to Cu^{2+}, we measured the distribution of aggregates sizes via SDS-PAGE. In measuring the soluble fraction of γS-WT after variable Cu^{2+} addition, we observed a predominance of monomeric protein, with noticeable dimer formation and trace high molecular weight complexes. Interestingly, the monomeric molecular weight range contains two distinct bands that are present at substoichiometric Cu^{2+} equivalents (SI Figure 3.8A). Additional analysis performed via lower sample loading and

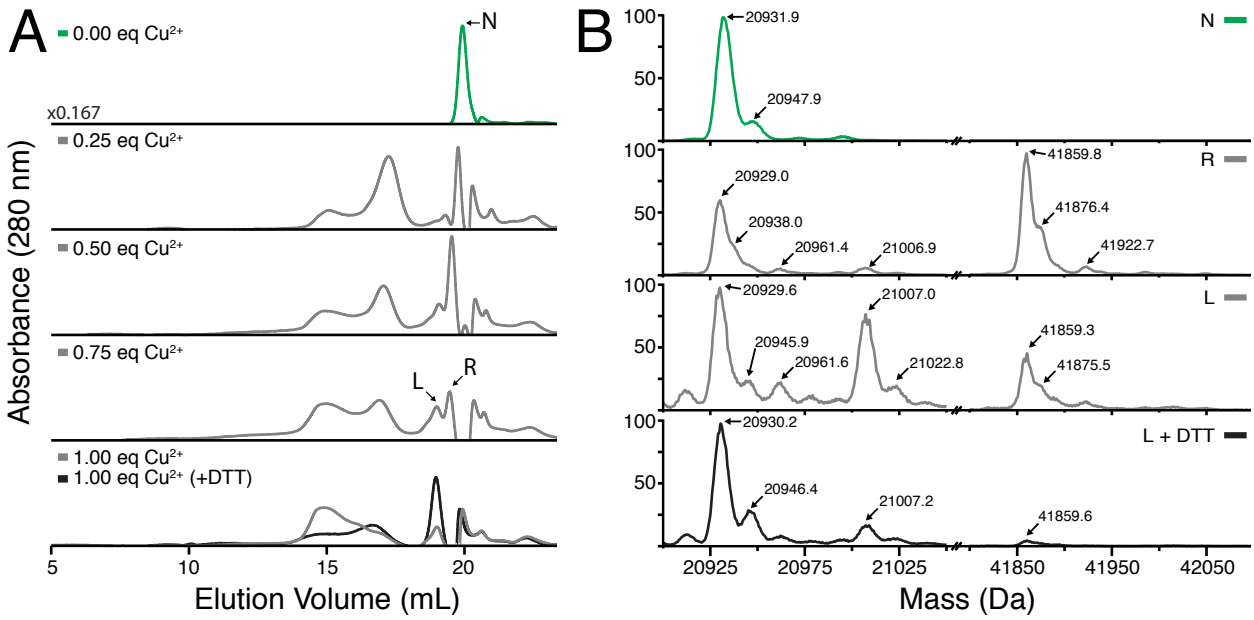

Figure 3.7: (**A**) Analytical SEC measurements of γS-WT treated with increasing equivalents of Cu^{2+} followed by excess EDTA. The addition of Cu^{2+} results in dimerization of γS, with a shift towards high molecular weight species with increasing concentration. These larger species are partly reversible via DTT reduction. (bottom panel). (**B**) Protein masses reconstructed using MaxEnt1 for individual peaks collected in (A). The untreated γS-WT (U) is strictly monomeric, whereas the peaks eluting at the same time (R) and just before (L) following copper treatment exhibit dimer character. Reduction via DTT considerably increases the total monomeric content of the L peak.

longer destaining showed that each of the initial two bands was a composite of two bands, indicating four distinct species. The presence of these four bands was consistent across several gels, with even fainter, lower bands also appearing in some gels. Reduction via BME results in the disappearance of the lower two bands (SI Figure 3.8B), but also occurred through treatment with EDTA (Figure 3.8B). These results indicate that the lower band are likely a result of Cu^{2+} binding and are consistent with previous observations of nickel-induced gel shifts[173]. γS-C_0 similarly produces two lower bands that were eliminated through EDTA addition.

The formation of intermolecular disulfide bonds between γS-crystallins is unsurprising given the high level of solvent accessibility of several cysteine residues. Similarly, the observation of intramolecular disulfide is not completely unexpected considering the proximity of the

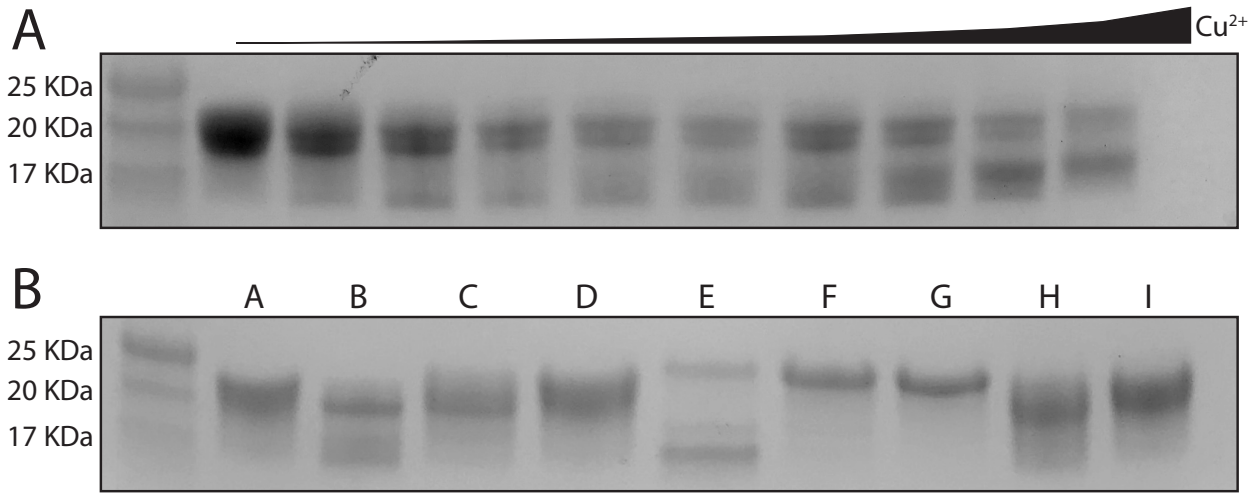

Figure 3.8: SDS-PAGE analysis of γS-crystallins (A) Soluble γS-WT after incubation with 0, 0.1, 0.2, 0.4, 0.6, 0.8, 1, 1.5, 2, 3, and 5 equivalents of Cu^{2+}. Two bands are observed at $\sim$20kDa beginning at 0.1 equivalent of Cu^{2+}. A lower band below the 17 kDa protein standard is also present after the addition of Cu^{2+} with a second band also present, most clearly visible at 1 and 2 equiv. (B) A: γS-WT, B: γS-WT treated 1 equivalent Cu^{2+} alone, C: sample B with EDTA, D: sample B with EDTA and BME, E: γS-C_0 treated 1 equivalent Cu^{2+}, F: sample E with EDTA, G: sample E with EDTA and BME, H: soluble UV-B treated γS-WT, I: sample H with BME.

C23, C25, C27, and C83 residues. What remains unclear, however, is the utility of these disulfide bonds as a buffering mechanism against Cu^{2+}-induced aggregation. Disulfides are observed in the crystal structures of human and mouse γS-crystallin (PDBID 6FD8[88], 6MYG, 6MYG), and are proposed to help enable domain-swapping and potentially drive aggregation. Conversely, the ability of γD to transfer an intramolecular disulfide bond to γD-W42Q[104] raises the possibility that γS could transfer disulfides internally as an oxidation buffering mechanism.

3.4 Conclusion

Several recent investigation of γ-crystallins have probed how cysteine may exacerbate or buffer aggregation. In this study we observe that the removal of the solvent accessible cysteines increases the susceptibility of γS-crystallin to Cu^{2+}-induced aggregation. The

reversibility of Cu^{2+}-binding to both γS-WT and γS-C_0 strongly indicates that multiple binding sites are present, raising the possibility that the cysteine tetrad of γS buffers further aggregation by coordinating to Cu^{2+}. The greater retention in structure of aggregated and soluble γS-WT compared to γS-C_0 also strongly suggests that the cysteine residues are important in buffering alternate aggregation mechanisms. While the exact mechanistic details of the Cu^{2+}-induced aggregation process require further investigation, crosslinking through intermolecular disulfide and other, unknown covalent bonds and hydrophobic interactions also contribute to this process. Intramolecular disulfide bonds also occur, although whether they destabilize the protein by locking it in a non-native confirmation or act as part of a buffering mechanism against oxidation in unknown. Further investigations are necessary to determine the binding sites of Cu^{2+} and refine our understanding of the molecular mechanisms underscoring the aggregation process.

Chapter 4

Multiple Aggregation Pathways in Human γS-Crystallin and Its Aggregation-Prone G18V Variant

4.1 Background

Cataract results from aggregation of the structural crystallin proteins of the eye lens. Several aggregation states have been observed in cataract, including fibrils, crystals, and most commonly, amorphous aggregates.[174] In the healthy eye lens, attractive interactions are present among the crystallin proteins, and $\beta\gamma$-crystallins maintain their refractive index gradient through short-range interprotein interactions.[175] Nevertheless, the $\beta\gamma$-crystallins exhibit a very low aggregation propensity, even at the high concentrations present in this specialized tissue.[176] Unmodified wild-type crystallin proteins are extremely stable in the lens environment; however, their solubility is readily compromised by changes in solution conditions, mutations, or posttranslational modifications. Most of the available literature indicates that

senile cataract primarily consists of amorphous aggregates[177, 178, 179, 180, 181]; however, several studies have shown that crystallins readily fibrillize in vitro under a variety of conditions,[182, 183, 184, 185, 186, 187, 33] and amyloid aggregates have been observed in vivo in mouse models of cataract.[177]

In general, protein aggregation has been implicated in numerous diseases as well as in vital cellular processes in organisms ranging from bacteria to humans. Aggregation mechanisms include nonspecific denaturation, native-like assemblies of the monomeric building block, or refolding into an alternate stable state. A wide variety of proteins are known to form amyloid fibrils, in which short b-strands stack upon one another and interact to form a characteristic cross-b structure.[188] This aggregation mechanism has been observed for many proteins, including those that are extremely soluble in their native conformations (e.g., lysozyme),[189, 190] leading to the hypothesis that the amyloid fibril state represents a generally stable state that any protein may adopt under appropriate conditions. Fibrillar structures have been observed for bovine α-, β-, and γ-crystallins,[191] as well as γD- and γC-crystallins.[183, 182] In γD-crystallin, elevated temperature promotes an increase in fibrillar aggregate formation at acidic pH.[33]

Many protein-deposition diseases are hereditary, with point mutations leading to protein products with reduced solubility. Some sequences are prone to misfolding to form amyloids, as in the case of the mutations causing early-onset Alzheimer's disease.[192] Alternatively, insoluble structures can be assembled from folded monomers having altered intermolecular interactions, as in sickle cell anemia.[193] Point mutations or posttranslational modifications can result in local unfolding, providing hotspots for aggregation despite the retention of all or most native structure.[194, 195, 196, 197, 198] At the other extreme, reduced overall stability leads to equilibrium unfolded states that promote nonspecific denaturation by exposing regions where hydrophobic interactions may occur between monomers, as in familial amyotrophic lateral sclerosis.[199]

To date more than 30 human γ-crystallin mutations have been linked to congenital cataract, including six truncations and two frameshifts (see Vendra et al.).[95, 200] Examples for human γD-crystallin include the G61C variant[201] and W42Q variant, which has increased aggregation propensity in the presence of the wild-type protein.[34] In γS-crystallin, the G18V,[93, 125, 124] G57W,[202] and D26G[163] variants are associated with hereditary cataract. The focus of the present study is γS-crystallin, the primary protein component in the cortex of the human eye lens and the most conserved of the mammalian crystallins, and its G18V variant. γS-G18V has been shown to be less thermally stable and more aggregation-prone than wildtype. Here we investigate whether the mutation alters the relative populations of different types of aggregates or changes the protein's susceptibility to UV light damage.

Crystallin aggregation can be induced or exacerbated by posttranslational modifications (PTMs) and UV-induced photodamage. UV-induced aggregates are of particular interest because the human eye lens is exposed to incident UV radiation from the sun on a daily basis. Although the cornea absorbs the bulk of the UV radiation reaching the eye, over a lifetime the total UV exposure of the lens is considerable. UV irradiation causes fragmentation and aggregate formation due to cross-linking in bovine β_L-crystallin.[203] This process is inhibited by the chaperone protein a-crystallin in vivo,[204] but as the lens ages, the aggregates accumulate until the chaperone is overwhelmed, resulting in cataract.[205, 206] Furthermore, UV-A radiation can cause dimerization and degradation of α-crystallin protein molecules themselves.[207] Many previous studies have focused on UV-B[185] or UV-C[208] irradiation. Here we investigate the effects of UV-A because lens fiber cells are exposed to a large flux of UV-A radiation over time, nearly 100 times greater than UV-B.[209] This potential source of cumulative photodamage is mitigated somewhat by UV-A–filtering metabolites present in the lens; however, wavelengths between 350 and 375 nm are nonetheless also absorbed by γ-crystallins.[210] Direct UV damage of crystallin proteins is implicated in cortical cataract, while the breakdown products of the small-molecule UV filters themselves play a

more important role in age-related nuclear cataract.[211] Characterization of the aggregates formed via all of these mechanisms is necessary in order to understand the interaction between protein mutations and environmental effects and to identify appropriate model systems for studying these processes in the laboratory.

4.2 Methods

4.2.1 Protein Expression and Purification

Expression and purification of wild-type human γS-crystallin (γS-WT) and γS-G18V was performed as described in Brubaker et al.[125] Briefly, pET28a(+) vectors (Novagen, Darmstadt, Germany) containing γS-WT and γS-G18V cDNA with an Nterminal 6x-His tag and a tobacco etch virus (TEV) protease cleavage sequence were transformed into Rosetta (DE3) Escherichia coli. Proteins were then overexpressed using standard isopropyl b-D-1-thiogalactopyranoside induction and lysed via sonication. Cell lysate was loaded on to a Ni-NTA column (Applied Biosystems, Foster City, CA, USA) and eluted using imidazole. His-tags were cleaved by TEV protease (produced in-house) and separated by reapplication to the Ni-NTA column. Finally, proteins were run over a HiLoad 16/ 600 Superdex 75 pg column (GE Healthcare Life Sciences, Piscataway, NJ, USA) and dialyzed into phosphate buffer (10 mM sodium phosphate, 150 mM NaCl, pH 6.9) prior to use.

4.2.2 Thermal and pH Aggregate Preparation

Purified γS-WT and γS-G18V were prepared at eight pH conditions using carbonate (pH 9), phosphate (pH 2, 3, 6, 7, 8), and acetate (pH 4, 5) buffers at 0.01 M with 150 mM NaCl. Samples were dialyzed by single pH increments over 12-hour periods to their final pH. Next,

aliquots of both proteins at 1 mg/mL were prepared and incubated at 25 °C or 37 °C in a water bath for 48 hours.

4.2.3 UV-A Induced Aggregation

Both proteins were concentrated to 6 mg/mL in phosphate buffer and filtered with a 0.22-lm filter. Samples were held in a 1-cm pathlength quartz cuvette (Starna Cells, Atascadero, CA, USA) and maintained between 22 °C and 24 °C using a temperature controller (Quantum Northwest Luma 40/Eclipse with Peletier element and recirculator; Quantum Northwest Inc., Liberty Lake, WA, USA). Continuous stirring was maintained throughout the experiment, with 100-lL aliquots taken every 10 minutes for 90 minutes. UV-A irradiation was produced using a 20 Hz Nd:YAG laser (Continuum Surelite II; Surelite, San Jose, CA, USA) coupled to a Surelite Separation Package (SSP) 2A (Surelite) to change the pump laser wavelength (1064 nm) to 355 nm via third harmonic generation. The laser flux was 89 mJ/cm2 at 10 Hz.

4.2.4 Turbidity Measurements

UV-irradiated samples were diluted with phosphate buffer to a concentration of 1 mg/mL. Samples were resuspended immediately prior to measurement in which 400-lL aliquots were loaded into a 1-cm pathlength quartz cuvette and measured using a spectrophotometer (JASCO V-730 UV-Vis; Jasco Analytical Instruments, Easton, MD, USA). The measured absorbance at 600 nm was used as the turbidity value.

4.2.5 Thioflavin T and Aromatic Fluorescence

To investigate amyloid fibril character, thioflavin T (ThT) assays were conducted as described by Nilsson et al.[212] A ThT working solution (25 lM ThT, 10 mM phosphate, 150 mM NaCl, pH 7) was prepared the day of analysis and used as a reference blank for all measurements. Aliquots (50 uL) of thermal or UV-treated protein were mixed with the ThT working solution to prepare 0.05 mg/mL samples for analysis. Fluorescence was recorded using a Gemini EM Microplate Reader (Molecular Devices, Sunnyvale, CA, USA) with 440 nm excitation and 482 nm emission. Measurements were performed in triplicate.

Intrinsic γS-crystallin tryptophan (Trp) fluorescence was measured using an excitation wavelength of 280 nm and emission range from 310 to 400 nm, in the instrument described above.

4.2.6 X-ray Diffraction

Aggregates were prepared for diffraction experiments by adding glycerol to the protein samples to a final concentration of 50% by volume. Each sample was mounted on a loop and frozen using a cryogenic nitrogen gas stream. X-ray diffraction data were collected using an in-house Rigaku MicroMax 007 rotating anode for x-ray generation and detected with a Saturn 944 detector (Crystal Logic, Los Angeles, CA, USA). Samples exhibiting diffraction bands corresponding to approximately 4.7 and 10 $\mathring{A}$ in real space contain amyloid fibrils. Lysozyme amyloid fibril samples prepared according to Xu et al. were used as a positive control.[213]

4.2.7 Matrix Assisted Laser Desorption Ionization-Time of Flight (MALDI-TOF) Mass Spectrometry

UV-irradiated and unexposed proteins were digested using MS Grade Pierce Trypsin Protease (ThermoFischer Scientific, Rockford, IL, USA) at 37 °C. The digest was mixed with saturated solution of a-cyano-4-hydrocinnamic acid in 50% acetonitrile and 1% trifluoroacetic acid and spotted onto a dry plate. MALDI-TOF analysis was performed using an AB SCIEX TOF/TOF 5800 System (SCIEX, Foster City, CA, USA and the resulting masses were referenced against the fragments predicted by Protein Prospector MS-Digest[214] (http://prospector.ucsf.edu, in the public domain).

4.3 Results

In order to measure the effects of pH on aggregate formation, the pH of γS-WT and γS-G18V solutions was varied over the range 2 through 9 while incubating the samples at room temperature (25 °C) and physiological temperature (37 °C). The ThT fluorescence of γS-WT and γS-G18V under all pH and both temperature conditions is summarized in Figure 4.1. Trace ThT fluorescence is observed for γS-WT held at 25 °C under all conditions examined, while for γS-G18V, elevated ThT fluorescence is observed at both low (2-3) and high (8-9) pH values (Fig. 4.1A). At 37 °C, samples of γS-WT incubated at pH 2 and 9 exhibit dramatic increases in fluorescence, while only minimal increases are observed at all remaining pH conditions. In contrast, γS-G18V exhibits elevated fluorescence over a larger pH range (pH 2-4 and 8-9). Roughly a 5-fold increase in ThT fluorescence is observed under acidic conditions (pH 2, 3, 4), while the signals observed from samples heated under basic conditions double in intensity. At 37 °C, γS-WT likewise displays a greater increase in ThT fluorescence at pH 2 than at pH 9.

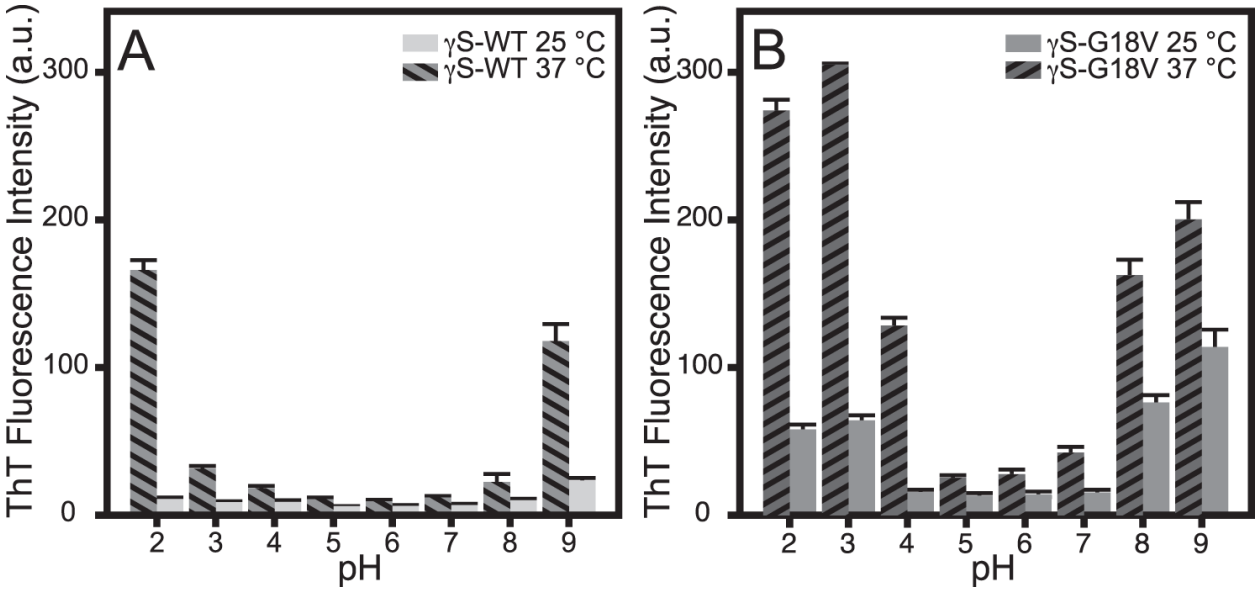

Figure 4.1: ThT fluorescence of γS-WT and γS-G18V prepared at variable pH and two temperatures. (A) For γS-WT at 25 °C, only background fluorescence is observed. For γS-G18V, elevated ThT fluorescence is observed at both low (2–3) and high (8–9) pH. Only heated samples (37 °C) at pH 2 and 9 exhibit elevated fluorescence. (B) At physiological temperature (37 °C), elevated ThT fluorescence is seen in γS-WT at pH 2 and 9, while γS-G18V displays significant increases in signal at pH 2, 3, 8, and 9.

In order to determine whether other aggregates were present that did not produce the elevated ThT fluorescence consistent with amyloid fibril formation, the solution turbidity was measured as the optical density at 600 nm (Figure 4.2). For γS-WT, increased turbidity was observed only at pH 9, despite increased ThT fluorescence at pH 2 and 9. The turbidity of γS-WT at pH 9 was roughly half that observed for γS-G18V under the same conditions. Increased turbidity for γS-G18V was greatest at pH 8 and 9, but also was elevated compared to neutral conditions at pH 2, 3, and 4.

The intrinsic Trp fluorescence of γS-WT and γS-G18V was measured in order to assess the degree of structural disruption to the crystallin fold upon changing the pH. Partial unfolding and changes to the local environment surrounding Trp residues alter the spectrum in both λ_{max} and intensity. In more polar environments, the Trp fluorescence maximum occurs at a longer wavelength; therefore, redshifting of the fluorescence peak indicates changes in conformation consistent with increased solvent exposure of the Trp residues. Trp fluorescence

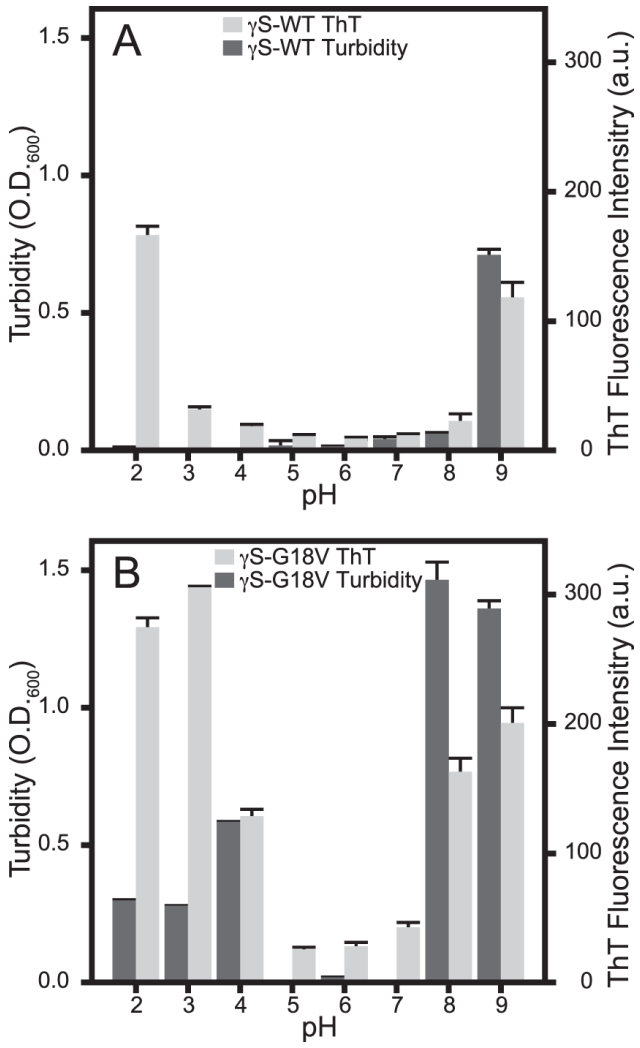

Figure 4.2: The ThT fluorescence and turbidity of γS-WT (A) and γS-G18V (B) from samples incubated at 37 °C plotted by pH. (A) Minimal γS-WT ThT fluorescence (light gray) and turbidity (dark gray) are observed over the pH range of 3 through 8. At pH 2, only ThT fluorescence increases, while both turbidity and ThT fluorescence increase at pH 9. (B) In γS-G18V, ThT fluorescence (light gray) and turbidity (dark gray) are elevated at basic and acidic conditions (pH 2, 3, 4, 8, 9). Acidic conditions result in the greatest γS-G18V ThT fluorescence levels, while basic conditions result in the greatest turbidity for γS-G18V. In both assays, only minimal changes are observed under neutral to weakly acidic conditions (pH 5, 6, 7).

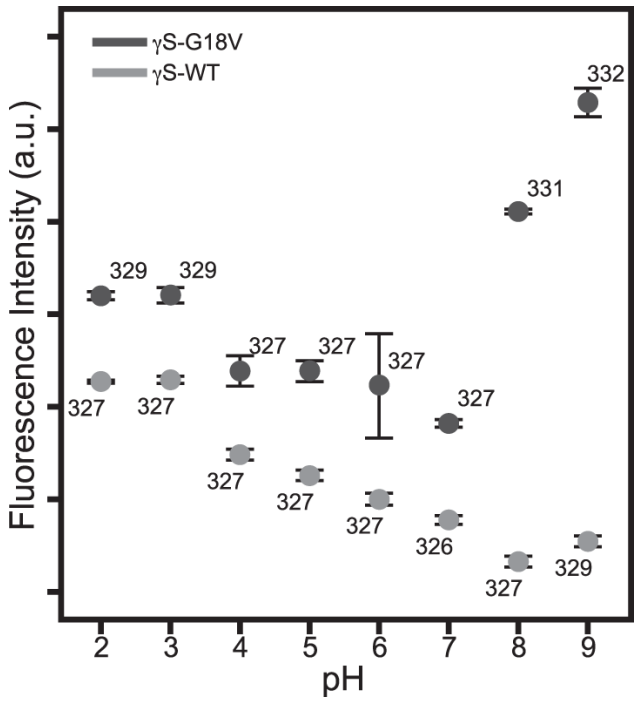

Figure 4.3: The intrinsic Trp fluorescence intensity for γS-WT (light gray) and γS-G18V (dark gray) at different pH values. The wavelength of the emission maximum is labeled next to each data point. Greater fluorescence for both proteins occurs under acidic conditions, with slight redshifting of the emission maxima for γS-G18V at pH 2 and 3. Under basic conditions, γS-G18V produces the greatest fluorescence intensity and maximum redshift, whereas the fluorescence intensity of γS-WT changes minimally and redshifts only slightly at pH 9.

results are summarized in Figure 4.3, while the full spectra for γS-WT and γS-G18V from pH 2 to 9 are shown in Supplementary Figure S1. The total Trp fluorescence signal decreases from pH 2 to 7 for both proteins, with only a slight redshift occurring for the fluorescence maxima at pH 2 and 3 in γS-G18V. Increased quenching is observed at pH 8 for γS-WT, and at pH 9 slight redshifting is also observed. The γS-G18V fluorescence signals at pH 8 and 9 are the most intense and redshifted observed for either protein, indicating that G18V is vulnerable to structural disruption at high pH, while γS-WT maintains the integrity of its fold over a wide range of solution conditions.

Aggregation of both γS-WT and γS-G18V was induced via UV-A irradiation at neutral pH and monitored using turbidity and ThT fluorescence. Samples of both proteins were irradiated for 90 minutes, at which point increases in solution turbidity leveled off (Supplementary Fig. S2). Both proteins exhibit large increases in turbidity following UV-A exposure. As for the samples incubated at physiological temperature, more aggregation is observed for γS-G18V than for γS-WT (Figure 4.4). In the case of both proteins, the UV-exposed samples exhibit only small increases in ThT fluorescence, suggesting that amyloid fibrils are not the

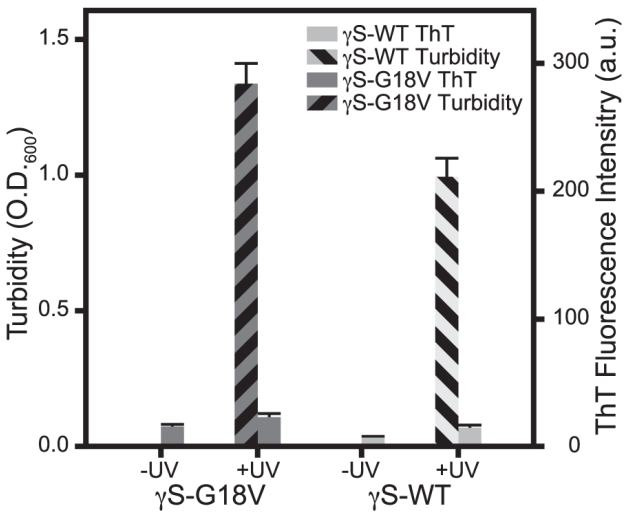

Figure 4.4: ThT fluorescence and turbidity measurements of γS-WT and γS-G18V at pH 7, before (-UV) and after (+UV) exposure to UV-A irradiation for 90 minutes. In both proteins, untreated samples display negligible ThT fluorescence and turbidity. UV-A irradiation produces significantly elevated turbidity, but only minimal increases in ThT fluorescence.

primary aggregation product produced under UV-A irradiation.

X-ray diffraction experiments were performed on low-pH and UV-treated γS-WT and γS-G18V in order to characterize the nature of the aggregates. Representative diffraction patterns are shown in Figure 5. Image analysis was conducted on a horizontal slice of the image, and all relevant peaks in the image intensity profile were labeled with their corresponding real-space resolution measurement, in angstrom units. The principal signals observed were sharp rings at 4.7 $\mathring{A}$ and broader rings at 10–11 $\mathring{A}$.

PTMs from UV-A photodamage were identified using MALDI-TOF mass spectrometry of trypsin-digested samples after 90 minutes of irradiation. Modifications were considered to be caused by UV-A irradiation if both the modified and unmodified fragments were observed and the peak corresponding to the modified fragment was uniquely observed in the UV-irradiated sample. Mass differences corresponding to deamidation (m + 1), oxidation (m + 16, m + 32), and Trp modifications such as kynurenine (m + 4) were observed in both proteins (Fig. 6).

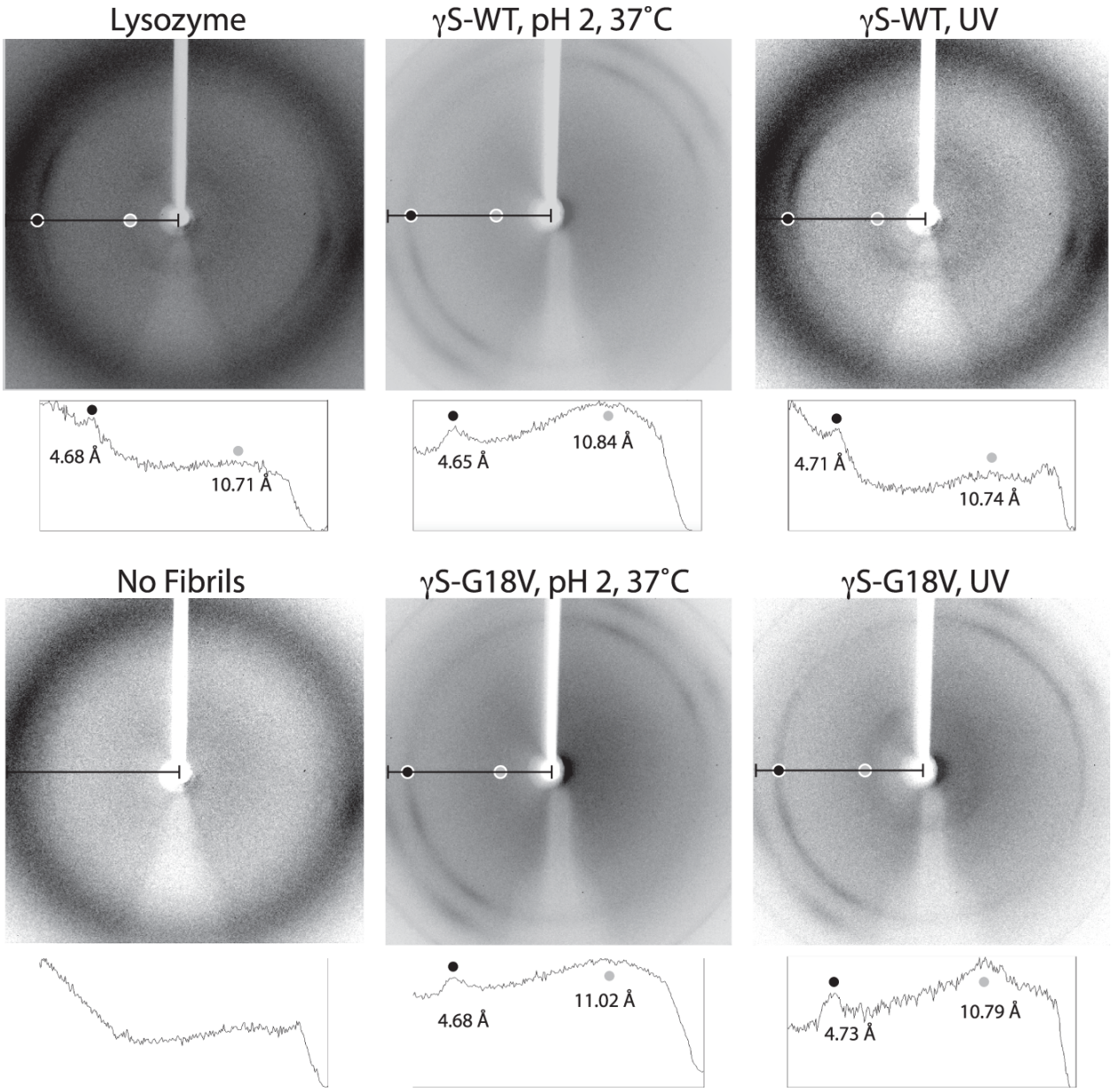

Figure 4.5: Representative x-ray diffraction patterns for fibrillar aggregates of γS-WT and γS-G18V. Lysozyme fibrils prepared by incubation at 60 °C and pH 2 for 2 days prior to the experiment were used as a positive control. Below each image, its corresponding image intensity profile is shown for the area of the image designated with a black line. Relevant peaks are labeled with their resolution measurement, in angstrom units, and the location of each peak is correlated to the location on the diffraction pattern with light gray or dark gray dots.

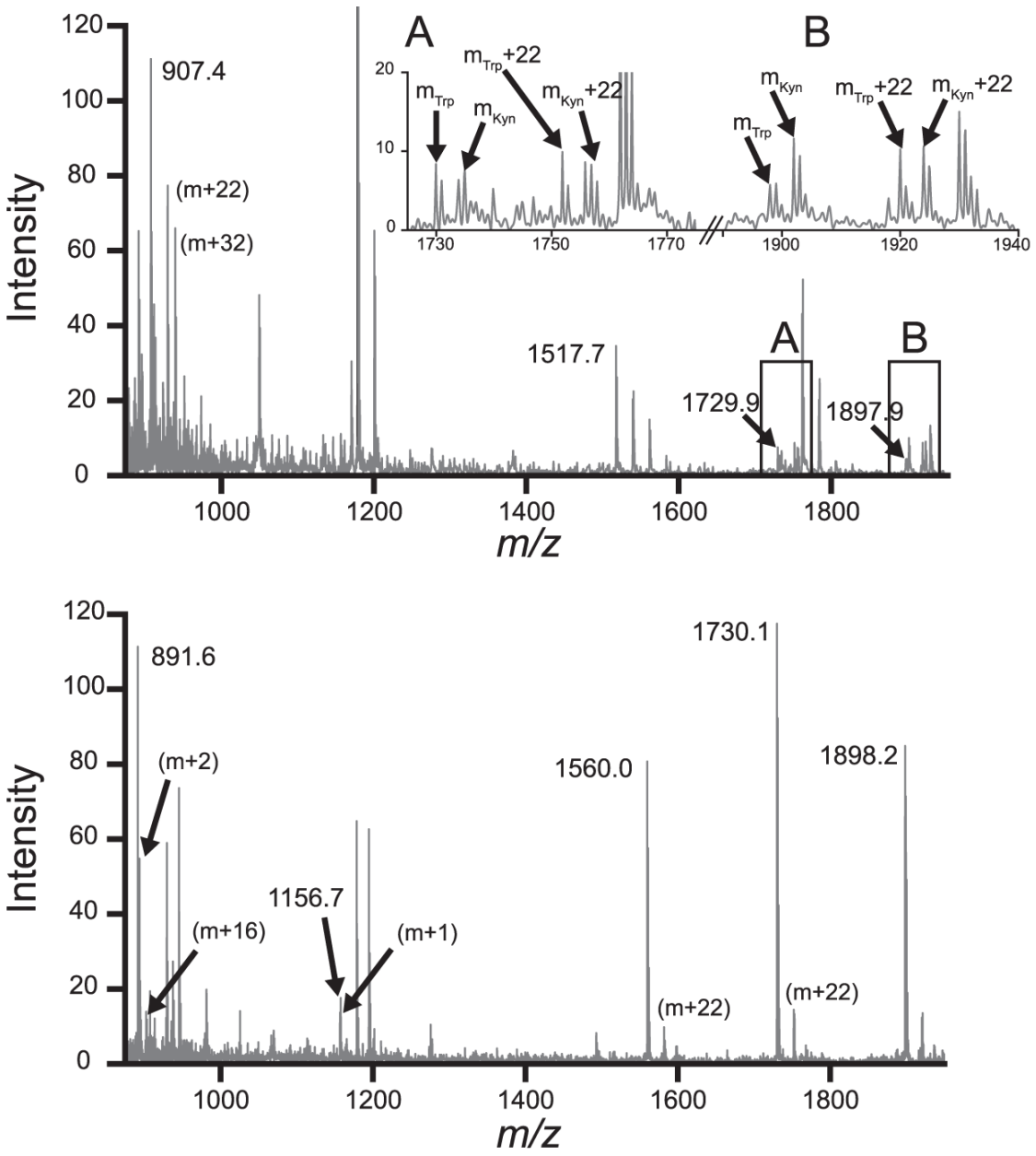

Figure 4.6: Representative MALDI-TOF spectra of trypsin-digested samples of γS-WT and γS-G18V after UV-A irradiation. Mass fragments were identified by manual comparison of mass-to-charge ratio peaks to the theoretical peaks and isotopic mass distributions from MS-Digest (http://prospector.ucsf.edu, in the public domain). Additional mass fragments corresponding to identifiable molecular weight changes are labeled with the specific mass difference, that is, m+16. Top: The γS-WT spectrum is shown with selected fragments annotated. Insets A and B display the observed cases of m+4 peaks in matched fragments containing a Trp residue. An m+4 mass difference matches a Trp-to-Kyn PTM. The masses for each peak are labeled as m_{Trp} and m_{Kyn}. Bottom: The γS-G18V distribution is shown with annotations indicating each of the observed peaks matching an MSDigest fragment. Kyn, kynurenine.

4.4 Discussion

Several pathways have been proposed to explain the mechanism of γ-crystallin aggregation.[215, 123, 216, 174, 217] Photochemical damage has been shown to cause intermolecular crosslinking, which may increase noncovalent aggregation due to redistributed charge altering the proteins' isoelectric points.[215] UV exposure may also produce reactive oxygen species via Fenton chemistry, resulting in nonspecific oxidation and crosslinking.[218] Other nonspecific PTMs such as glycation,[219] acetylation,[90] and deamidation[220] may destabilize the protein structure, similar to the effects of point mutations.[200, 221, 164, 165, 85] Unfolding within either domain or at the domain interface may lead to different domain-swapped aggregation pathways,[34] precede amyloid fibril formation,[183] or result in nonspecific aggregation.[222, 223, 224] Furthermore, two or more of these pathways may be in competition under a particular set of conditions, as is observed for both γS-WT and γS-G18V.

From these data, it is clear that low-pH conditions are necessary for γS-WT to form amyloid fibrils at physiological temperature. Under every other condition that was tested, the samples remained translucent with no visible signs of aggregation, and there was little to no increase in ThT fluorescence intensity, indicating the absence of b-amyloid structure. This result is not surprising given that γS-WT is a highly stable protein that has been selected for a very low propensity to aggregate, even under harsh conditions. By contrast, γS-G18V exhibits large increases in ThT fluorescence intensity under conditions where none was observed for γS-WT. For γS-G18V, increased ThT fluorescence signals were observed in all samples incubated at 37 °C, save for the pH 7 sample, and in two of the room-temperature samples as well (pH 2 and pH 9).

Although increased ThT fluorescence intensity was not observed in the γS-G18V pH 4, 25 °C sample or the pH 7, 37 °C sample, the incubated samples had visibly aggregated at the

time of the fluorescence measurement, indicating the formation of nonamyloid aggregates and supporting the hypothesis that more than one aggregation state is available to γS-crystallin. The increase in turbidity seen in these two samples without an accompanying increase in ThT fluorescence indicates that these aggregates are not fibrillar and instead adopt a more disordered aggregation state. Likewise, for γS-WT incubated at pH 2, strong ThT fluorescence but only weak turbidity were observed, consistent with reports for γD-crystallin under similar conditions.15 Similar changes were observed for γS-G18V at pH 2 and 3. However, correlated increases in ThT fluorescence and turbidity were seen for γS-WT at pH 9 and γS-G18V at pH 4, 8, and 9, indicating that the pH strongly influences the balance of different aggregation states.

Intrinsic Trp fluorescence was used to assess the degree of protein unfolding implicated in these different aggregation pathways. Trp fluorescence is a sensitive probe of native structure in this system because each Greek key domain contains two critical Trp residues in its hydrophobic core. These residues absorb UV-B light and are thought to participate in a proposed fluorescence resonance energy transfer quenching mechanism to dissipate energy that might otherwise damage the lens or retina.[26, 25, 137] The intrinsic aromatic Förster of γS-WT and γS-G18V showed similar quenching patterns under acidic (pH 2) to neutral (pH 7) conditions, with a slight redshift in the signal for γS-G18V under acidic conditions. The reduction in fluorescence quenching under acidic conditions may be correlated with changes in the protonation states of carboxyl side chains, which can disrupt hydrogen-bonding interactions and salt bridges. Under mildly basic conditions (pH 8 and 9), γS-G18V exhibits a larger redshift of 4–5 nm, along with significant increases in fluorescence compared to pH 7. For γS-WT, only minor changes are observed, even at pH 9.

In γS-G18V, significant structural changes are apparent from the large redshift at pH 8–9. These may be related to changes in cysteine protonation (pKa ∼8) and are consistent with the large structural rearrangement of the area around the cysteine loop of γS-G18V

relative to that of γS-WT, as observed in the solution-nuclear magnetic resonance structures (Protein Data Bank ID 2M3U and 2M3T).65 These data suggest that basic pH conditions favor partial unfolding of γS-G18V, while γS-WT does not appear to experience even partial unfolding under any conditions tested here. The observed redshifts in the Trp fluorescence maxima correlate with the increased optical densities: γS-G18V at pH 8 and 9 are the most turbid and display the greatest redshifts, while γS-WT at pH 9 and γS-G18V at pH 2 and 3 exhibit smaller redshifts and reduced optical density.

UV-A irradiation was also explored as a more biologically relevant mechanism of aggregation initiation. In our experiments, prolonged irradiation resulted in elevated solution turbidity, yet produced weaker ThT fluorescence than samples treated under acidic and basic conditions at physiological temperature. The minimal ThT fluorescence and elevated turbidity of UV-irradiated samples is most comparable to thermally treated γS-WT and γS-G18V under basic conditions. The reduced ThT response following the initial turbidity increases correlated with visible yellowing in irradiated sample precipitates, which were initially white, but progressively darkened with UV exposure.

To identify some of the protein modifications produced via UV-A exposure, endpoint samples were digested using trypsin and analyzed via MALDI-TOF mass spectrometry. The resulting data were compared to theoretical molecular weight values predicted by Protein Prospector MS-Digest with modifications reported from mass spectrometry analysis of cataractous lenses.[225, 89] Deamidation and oxidation products were both observed, consistent with literature reports of digested normal and cataract lenses.[90, 226] In particular, mass differences of 4 and 20 Da were observed, suggesting the presence of the tryptophan oxidation products kynurenine and N-formylkynurenine. This result is consistent with the yellowing of the UV aggregates over time, because kynurenine absorbs blue light, contributing to the color changes ranging from yellowing to browning often seen in aged lenses.[226]

To test for the presence of amyloid fibril character in our different aggregates, x-ray diffrac-

tion experiments were conducted. Powder diffraction techniques can be utilized to gain structural information about the degree of local order in solid samples. Diffraction patterns of noncrystalline structures can yield valuable information about the average distances between molecules. Due to the repeating cross-b structure of the fibril, the appearance of characteristic diffraction bands in the reciprocal space diffraction pattern corresponding to 4.7 and 10 Å in real space will be observed in samples containing amyloid fibrils. These distances represent the interstrand distance between b-strands along the fibril axis and the intersheet spacing distance within the fibril, respectively. Powder x-ray diffraction (representative data shown in Fig. 5) indicates that amyloid fibrils were detectable even under conditions that produced only weak ThT fluorescence, in this case UV-irradiated samples at neutral pH.

The results of these experiments support the hypothesis that there are at least two aggregation states available to both γS-WT and γS-G18V. One of these states is a disordered aggregate with little to no amyloid fibril character, which nonetheless results in the opacification of the sample, as seen through the increase in turbidity without an increase in ThT fluorescence or the amyloid fibril diffraction bands in the x-ray diffraction pattern. The second state has significant amyloid fibril character, as shown in both the increased ThT fluorescence and the appearance of the fibril diffraction bands in the x-ray diffraction experiments. The γS-G18V variant samples formed this second type of aggregate more readily, and under a broader range of conditions than the WT protein. UV-A exposure at neutral pH leads to aggregation as indicated by increased solution turbidity. Although only a weak ThT response is observed in these samples, amyloid fibril character is confirmed via powder x-ray diffraction. Taken together, these data suggest that changing the solution can shift the population of the two aggregation states to favor one or the other, but both forms are detectable under all conditions where aggregation was observed.

The visible coloration of UV samples provides a clue that photodamage may occur during

UV-A exposure. MALDI-TOF mass spectrometry of digested samples of UV-A–irradiated γS-WT and γS-G18V confirmed but does not inform us about, the mechanism driving aggregation or differentiate it from similar results produced via other methods; further studies are needed to elucidate the mechanisms underlying these disparate aggregation pathways.

4.5 Conclusions

Our results indicate that multiple aggregation pathways are accessible to both wild-type γS-crystallin and its aggregation prone G18V variant. The method used to initiate aggregation strongly determines the relative populations of the two types of aggregates, although both types are present under the conditions tested. The disease-related variant forms more aggregates than wild-type, and under milder conditions, but it does not apparently favor a particular type of aggregate. Future studies will focus on further characterization of the aggregates induced by UV-A irradiation.

Chapter 5

Conclusion

The γ-crystallins are unique structural proteins that have evolved to meet the demands of the eye lens environment. As seen through comparative biophysical characterizations to Ci-$\beta\gamma$, the γ-crystallins have eschewed stabilizing interactions with Ca^{2+} and other divalent cations. One aspect of this evolution has been the increased prevalence of cysteine residues, which strongly contribute to the proteins elevated dn/dc. While these cysteines enable aggregation through transition metal intermolecular crosslinkings, they also serve to buffer against Cu^{2+}-induced aggregation as aggregates without cysteines exhibit more unfolded character and aggregate more readily. Investigating the mechanisms behind Cu^{2+} mediated aggregation evidences that the several, interconnected mechanism are involved. Intermolecular copper-bridged crosslinkings occurs at multiple sites in addition to inter-/intra-molecular disulfide bonding and covalent crosslinkings that likely proceeds through a radical mechanism. Some of the indicators of ROS damage are similar to those observed from UV damage, but manifest differently. UV-induced aggregation was shown to occur from UVA and UVB irradiation with similar effects. These types of damage manifest in elevated levels of turbidity but do not respond to thioflavin T, unlike acid-induced fibrils of γS-crystallin. These results indicate that amyloid fibrils are unlikely to occur as a result of UV exposure.

Bibliography

[1] Aleš Cvekl and Ruth Ashery-Padan. The cellular and molecular mechanisms of vertebrate lens development. *Development*, 141(23):4432–4447, 2014.

[2] Hans Bloemendal, Wilfried de Jong, Rainer Jaenicke, Nicolette H Lubsen, Christine Slingsby, and Annette Tardieu. Ageing and vision: structure, stability and function of lens crystallins. *Progress in biophysics and molecular biology*, 86(3):407–485, 2004.

[3] Christine Slingsby, Graeme J Wistow, and Alice R Clark. Evolution of crystallins for a role in the vertebrate eye lens. *Protein Science*, 22(4):367–380, 2013.

[4] N Phelps Brown and Anthony J Bron. Lens disorders: a clinical manual of cataract diagnosis. *Ophthalmic Literature*, 1(49):64, 1996.

[5] Joseph Horwitz, Michael P Bova, Lin-Lin Ding, Dana A Haley, and Phoebe L Stewart. Lens α-crystallin: function and structure. *Eye*, 13(3b):403, 1999.

[6] Mathias Uhlén, Linn Fagerberg, Björn M Hallström, Cecilia Lindskog, Per Oksvold, Adil Mardinoglu, Åsa Sivertsson, Caroline Kampf, Evelina Sjöstedt, Anna Asplund, et al. Tissue-based map of the human proteome. *Science*, 347(6220):1260419, 2015.

[7] Xiaoqiu Huang and Webb Miller. A time-efficient, linear-space local similarity algorithm. *Advances in Applied Mathematics*, 12(3):337–357, 1991.

[8] Nathalie Braun, Martin Zacharias, Jirka Peschek, Andreas Kastenmüller, Juan Zou, Marianne Hanzlik, Martin Haslbeck, Juri Rappsilber, Johannes Buchner, and Sevil Weinkauf. Multiple molecular architectures of the eye lens chaperone αb-crystallin elucidated by a triple hybrid approach. *Proceedings of the National Academy of Sciences*, 108(51):20491–20496, 2011.

[9] Scott P Delbecq and Rachel E Klevit. One size does not fit all: the oligomeric states of αb crystallin. *FEBS letters*, 587(8):1073–1080, 2013.

[10] K Krishna Sharma, R Senthil Kumar, G Suresh Kumar, and P Thomas Quinn. Synthesis and characterization of a peptide identified as a functional element in αa-crystallin. *Journal of Biological Chemistry*, 275(6):3767–3771, 2000.

[11] Zohreh Toossi Farahbakhsh, Qing-Ling Huang, Lin-Lin Ding, Christian Altenbach, Heinz-Jürgen Steinhoff, Joseph Horwitz, and Wayne L Hubbell. Interaction of. alpha.-crystallin with spin-labeled peptides. *Biochemistry*, 34(2):509–516, 1995.

[12] Christine Slingsby and OA Bateman. Quaternary interactions in eye lens. beta.-crystallins: basic and acidic subunits of. beta.-crystallins favor heterologous association. *Biochemistry*, 29(28):6592–6599, 1990.

[13] Bing-Fen Liu and Jack J-N Liang. Protein–protein interactions among human lens acidic and basic β-crystallins. *FEBS letters*, 581(21):3936–3942, 2007.

[14] M Saleh Ajaz, Zhixiang Ma, David L Smith, and Jean B Smith. Size of human lens β-crystallin aggregates are distinguished by n-terminal truncation of βb1. *Journal of Biological Chemistry*, 272(17):11250–11255, 1997.

[15] Zhaoyong Xi, Matthew J Whitley, and Angela M Gronenborn. Human βb2-crystallin forms a face-en-face dimer in solution: An integrated nmr and saxs study. *Structure*, 25(3):496–505, 2017.

[16] OA Bateman, R Sarra, ST Van Genesen, G Kappe, NH Lubsen, and C Slingsby. The stability of human acidic β-crystallin oligomers and hetero-oligomers. *Experimental eye research*, 77(4):409–422, 2003.

[17] Takumi Takata, Luke G Woodbury, and Kirsten J Lampi. Deamidation alters interactions of β-crystallins in hetero-oligomers. *Molecular vision*, 15:241, 2009.

[18] Graeme Wistow. The human crystallin gene families. *Human genomics*, 6(1):26, 2012.

[19] Heiner Hartwich, Elena Rosengauer, Lukas Rüttiger, Viviane Wilms, Sarah-Kristin Waterholter, and Hans Gerd Nothwang. Functional role of γ-crystallin n in the auditory hindbrain. *PloS one*, 11(8):e0161140, 2016.

[20] S Tomarev, L Segovia, C Slingsby, and T Vihtelic. gamman-crystallin and the evolution of the betagamma-crystallin super-family in vertebrates. *FEBS J*, 272:22762291, 2005.

[21] KIMIKAZU Iwami, JIAN-YING Wang, RAJEEVE Jain, S McCormack, and LR Johnson. Intestinal ornithine decarboxylase: half-life and regulation by putrescine. *American Journal of Physiology-Gastrointestinal and Liver Physiology*, 258(2):G308–G315, 1990.

[22] S Mankarious, M Lee, S Fischer, KH Pyun, HD Ochs, VA Oxelius, and RJ Wedgwood. The half-lives of igg subclasses and specific antibodies in patients with primary immunodeficiency who are receiving intravenously administered immunoglobulin. *The Journal of laboratory and clinical medicine*, 112(5):634–640, 1988.

[23] Brandon H Toyama and Martin W Hetzer. Protein homeostasis: live long, won't prosper. *Nature reviews Molecular cell biology*, 14(1):55, 2013.

[24] Fanrong Kong and Jonathan King. Contributions of aromatic pairs to the folding and stability of long-lived human γd-crystallin. *Protein Science*, 20(3):513–528, 2011.

[25] Jiejin Chen, Shannon L Flaugh, Patrik R Callis, and Jonathan King. Mechanism of the highly efficient quenching of tryptophan fluorescence in human γd-crystallin. *Biochemistry*, 45(38):11552–11563, 2006.

[26] Jiejin Chen, Patrik R Callis, and Jonathan King. Mechanism of the very efficient quenching of tryptophan fluorescence in human γd-and γs-crystallins: the γ-crystallin fold may have evolved to protect tryptophan residues from ultraviolet photodamage. *Biochemistry*, 48(17):3708–3716, 2009.

[27] Weihong Qiu, Tanping Li, Luyuan Zhang, Yi Yang, Ya-Ting Kao, Lijuan Wang, and Dongping Zhong. Ultrafast quenching of tryptophan fluorescence in proteins: Interresidue and intrahelical electron transfer. *Chemical Physics*, 350(1-3):154–164, 2008.

[28] Huaying Zhao, Patrick H Brown, M Teresa Magone, and Peter Schuck. The molecular refractive function of lens γ-crystallins. *Journal of molecular biology*, 411(3):680–699, 2011.

[29] Huaying Zhao, Patrick H Brown, and Peter Schuck. On the distribution of protein refractive index increments. *Biophysical journal*, 100(9):2309–2317, 2011.

[30] Barbara Pierscionek, George Smith, and Robert C Augusteyn. The refractive increments of bovine α-, β-and γ-crystallins. *Vision research*, 27(9):1539–1541, 1987.

[31] Domarin Khago, Jan C Bierma, Kyle W Roskamp, Natalia Kozlyuk, and Rachel W Martin. Protein refractive index increment is determined by conformation as well as composition. *Journal of Physics: Condensed Matter*, 30(43):435101, 2018.

[32] Tianqi O Zhang, Ariel M Alperstein, and Martin T Zanni. Amyloid β-sheet secondary structure identified in uv-induced cataracts of porcine lenses using 2d ir spectroscopy. *Journal of molecular biology*, 429(11):1705–1721, 2017.

[33] Josephine W Wu, Mei-Er Chen, Wen-Sing Wen, Wei-An Chen, Chien-Ting Li, Chih-Kai Chang, Chun-Hsien Lo, Hwai-Shen Liu, and Steven S-S Wang. Comparative analysis of human γd-crystallin aggregation under physiological and low ph conditions. *PLoS One*, 9(11):e112309, 2014.

[34] Eugene Serebryany and Jonathan A King. Wild-type human γd-crystallin promotes aggregation of its oxidation-mimicking, misfolding-prone w42q mutant. *Journal of Biological Chemistry*, 290(18):11491–11503, 2015.

[35] Kuo-Ying Huang, Carolyn N Kingsley, Ryan Sheil, Chi-Yuan Cheng, Jan C Bierma, Kyle W Roskamp, Domarin Khago, Rachel W Martin, and Songi Han. Stability of protein-specific hydration shell on crowding. *Journal of the American Chemical Society*, 138(16):5392–5402, 2016.

[36] R Kanwar and D Balasubramanian. Structure and stability of the dityrosine-linked dimer of γb-crystallin. *Experimental eye research*, 68(6):773–784, 1999.

[37] Hui-Ren Zhao, Ramanakoppa H Nagaraj, and Edathara C Abraham. The role of α-and ε-amino groups in the glycation-mediated cross-linking of γb-crystallin study of three site-directed mutants. *Journal of Biological Chemistry*, 272(22):14465–14469, 1997.

[38] JA Dominguez-Calva, ML Perez-Vazquez, E Serebryany, JA King, and L Quintanar. Mercury-induced aggregation of human lens γ-crystallins reveals a potential role in cataract disease. *JBIC Journal of Biological Inorganic Chemistry*, 23(7):1105–1118, 2018.

[39] Liliana Quintanar, Jos A Domínguez-Calva, Eugene Serebryany, Lina Rivillas-Acevedo, Cameron Haase-Pettingell, Carlos Amero, and Jonathan A King. Copper and zinc ions specifically promote nonamyloid aggregation of the highly stable human γ-d crystallin. *ACS chemical biology*, 11(1):263–272, 2015.

[40] Jennifer C Boatz, Matthew J Whitley, Mingyue Li, Angela M Gronenborn, and Patrick CA van der Wel. Cataract-associated p23t γd-crystallin retains a native-like fold in amorphous-looking aggregates formed at physiological ph. *Nature communications*, 8:15137, 2017.

[41] Jan C Bierma, Kyle W Roskamp, Aaron P Ledray, Andor J Kiss, C-H Christina Cheng, and Rachel W Martin. Controlling liquid–liquid phase separation of cold-adapted crystallin proteins from the antarctic toothfish. *Journal of molecular biology*, 430(24):5151–5168, 2018.

[42] G. Wistow, L. Summers, and T. Blundell. *Myxococcus xanthus* spore coat protein S may have a similar structure to vertebrate lens $\beta\gamma$-crystallins. *Nature*, 315:771–773, 1985.

[43] Graeme Wistow. Evolution of a protein superfamily: relationships between vertebrate lens crystallins and microorganism dormancy proteins. *Journal of Molecular Evolution*, 30(2):140–145, 1990.

[44] R. Esposito, C. Racioppi, M.R. Pezzotti, M. Branno, A. Locascio, F. Ristoratore, and A. Spagnuolo. The ascidian pigmented sensory organs: Structures and developmental programs. *Genesis: The Journal of Genetics and Development*, 53(1):15–33, 2015.

[45] D. Sakurai, M. Goda, Y. Kohmura, T. Horie, H. Iwamoto, H. Ohtsuki, and M. Tsuda. The role of pigment cells in the brain of ascidian larva. *Journal of Comparative Neurology*, 475:70–82, 2004.

[46] Laura Coniglio, Angelica Morale, Cristiano Angelini, and Carla Falugi. Cholinergic activation of settlement in *Ciona intestinalis* metamorphosing larvae. *The Journal of Experimenal Zoology*, 280:314–320, 1998.

[47] Sebastian M Shimeld, Andrew G Purkiss, Ron PH Dirks, Orval A Bateman, Christine Slingsby, and Nicolette H Lubsen. Urochordate $\beta\gamma$-crystallin and the evolutionary origin of the vertebrate eye lens. *Current Biology*, 15(18):1684–1689, 2005.

[48] Amita Mishra, Bal Krishnan, Rajeev Raman, and Yogendra Sharma. Ca^{2+} and $\beta\gamma$-crystallins: An affair that did not last? *Biochimica et Biophysica Acta - General Subjects*, 1860(1):299–303, 2016.

[49] Ravi P Barnwal, Maroor K Jobby, Yogendra Sharma, and Kandala VR Chary. NMR assignment of M-crystallin: A novel Ca^{2+} binding protein of the $\beta\gamma$-crystallin superfamily from *Methanosarcina acetivorans*. *Journal of Biomolecular NMR*, 36:32–32, 2006.

[50] Shashi Kumar Suman, Daddali Ravindra, Yogendra Sharma, and Amita Mishra. Association properties and unfolding of a $\beta\gamma$-crystallin domain of a Vibrio-specific protein. *PloS One*, 8(1):e53610, 2013.

[51] Maroor K. Jobby and Yogendra Sharma. Calcium-binding to lens βB2-and βA3-crystallins suggests that all β-crystallins are calcium-binding proteins. *The FEBS Journal*, 274(16):4135–4147, 2007.

[52] Bheemreddy Rajini, Preetha Shridas, C Sivakama Sundari, Dasari Muralidhar, Sushil Chandani, Fairwell Thomas, and Yogendra Sharma. Calcium binding properties of γ-crystallin: calcium ion binds at the Greek key $\beta\gamma$-crystallin fold. *Journal of Biological Chemistry*, 276(42):38464–38471, 2001.

[53] Natalia Kozlyuk, Suvrajit Sengupta, Jan C Bierma, and Rachel W Martin. Calcium binding dramatically stabilizes an ancestral crystallin fold in tunicate $\beta\gamma$-crystallin. *Biochemistry*, 55(50):6961–6968, 2016.

[54] Joram Piatigorsky. Delta crystallins and their nucleic acids. *Molecular and Cellular Biochemistry*, 59(1-2):33–56, 1984.

[55] Shyh-Horng Chiou, WP Chang, and CC Chen. Characterization and comparison of epsilon-crystallin and lactate dehydrogenases in the lenses of vertebrates and invertebrates. *Biochemistry International*, 18(6):1093–1100, 1989.

[56] Q-L Huang, P Russell, SH Stone, and JS Zigler. Zeta-crystallin, a novel lens protein from the guinea pig. *Current Eye Research*, 6(5):725–732, 1987.

[57] JW Mulders, Wiljan Hendriks, W Matthijs Blankesteijn, Hans Bloemendal, and Wilfried W de Jong. Lambda-crystallin, a major rabbit lens protein, is related to hydroxyacyl-coenzyme A dehydrogenases. *Journal of Biological Chemistry*, 263(30):15462–15466, 1988.

[58] Graeme J Wistow, Tom Lietman, Leah A Williams, Steven O Stapel, Wilfried W De Jong, Joseph Horwitz, and Joram Piatigorsky. Tau-crystallin/alpha-enolase: one gene encodes both an enzyme and a lens structural protein. *The Journal of Cell Biology*, 107(6):2729–2736, 1988.

[59] Kalyan S Ghosh, Ajay Pande, and Jayanti Pande. Binding of γ-crystallin substrate prevents the binding of copper and zinc ions to the molecular chaperone α-crystallin. *Biochemistry*, 50(16):3279–3281, 2011.

[60] Srinivasagan Ramkumar, Xingjun Fan, Benlian Wang, Sichun Yang, and Vincent M Monnier. Reactive cysteine residues in the oxidative dimerization and Cu^{2+} induced

aggregation of human γD-crystallin: Implications for age-related cataract. *Biochimica et Biophysica Acta - Molecular Basis of Disease*, 1864(11):3595–3604, 2018.

[61] Jennmin Lin. Pathophysiology of cataracts: copper ion and peroxidation in diabetics. *Japanese Journal of Ophthalmology*, 41(3):130–137, 1997.

[62] Erdinc Aydin, Tongabay Cumurcu, Fikret Özuĝurlu, Hüseyin Özyurt, Serdar Sahinoglu, Durali Mendil, and Erdoĝan Hasdemir. Levels of iron, zinc, and copper in aqueous humor, lens, and serum in nondiabetic and diabetic patients. *Biological trace element research*, 108(1-3):33–41, 2005.

[63] Osman Cekic. Effect of cigarette smoking on copper, lead, and cadmium accumulation in human lens. *British Journal of Ophthalmology*, 82(2):186–188, 1998.

[64] J Dawczynski, M Blum, K Winnefeld, and J Strobel. Increased content of zinc and iron in human cataractous lenses. *Biological Trace Element Research*, 90(1-3):15–23, 2002.

[65] Martina Schmeling, Bruce I Gaynes, and Susanne Tidow-Kebritchi. Heavy metal analysis in lens and aqueous humor of cataract patients by total reflection X-ray fluorescence spectrometry. *Powder Diffraction*, 29(2):155–158, 2014.

[66] Marcus W Brazier, Paul Davies, Esmie Player, Frank Marken, John H Viles, and David R Brown. Manganese binding to the prion protein. *Journal of Biological Chemistry*, 283(19):12831–12839, 2008.

[67] Ravi Pratap Barnwal, MK Jobby, K Manjula Devi, Yogendra Sharma, and Kandala VR Chary. Solution structure and calcium-binding properties of M-crystallin, a primordial $\beta\gamma$-crystallin from archaea. *Journal of Molecular Biology*, 386(3):675–689, 2009.

[68] Penmatsa Aravind, Amita Mishra, Shashi Kumar Suman, Maroor K Jobby, Rajan Sankaranarayanan, and Yogendra Sharma. The $\beta\gamma$-crystallin superfamily contains a universal motif for binding calcium. *Biochemistry*, 48(51):12180–12190, 2009.

[69] Michael Kretschmar, Eva-Maria Mayr, and Rainer Jaenicke. Kinetic and thermodynamic stabilization of the $\beta\gamma$-crystallin homolog spherulin 3a from *Physarum polycephalum* by calcium binding. *Journal of Molecular Biology*, 289(4):701–705, 1999.

[70] Martina Wenk, Roland Baumgartner, Tad A Holak, Robert Huber, Rainer Jaenicke, and Eva-Maria Mayr. The domains of protein S from *Myxococcus xanthus*: structure, stability and interactions. *Journal of Molecular Biology*, 286(5):1533–1545, 1999.

[71] Kumars Riyahi and Sebastian M Shimeld. Chordate $\beta\gamma$-crystallins and the evolutionary developmental biology of the vertebrate lens. *Comparative Biochemistry and Physiology Part B: Biochemistry and Molecular Biology*, 147(3):347–357, 2007.

[72] Eric E Snyder, Brian W Buoscio, and Joseph J Falke. Calcium (ii) site specificity: effect of size and charge on metal ion binding to an EF-hand-like site. *Biochemistry*, 29(16):3937–3943, 1990.

[73] Chul-Seung Park and Roderick MacKinnon. Divalent cation selectivity in a cyclic nucleotide-gated ion channel. *Biochemistry*, 34(41):13328–13333, 1995.

[74] Sylvain Brunet, Todd Scheuer, Rachel Klevit, and William A Catterall. Modulation of CaV1. 2 channels by Mg^{2+} acting at an EF-hand motif in the COOH-terminal domain. *The Journal of General Physiology*, 126(4):311–323, 2005.

[75] SG Dove and MJ Kingsford. Use of otoliths and eye lenses for measuring trace-metal incorporation in fishes: a biogeographic study. *Marine Biology*, 130(3):377–387, 1998.

[76] Naomi J Clout, Michael Kretschmar, Rainer Jaenicke, and Christine Slingsby. Crystal structure of the calcium-loaded spherulin 3a dimer sheds light on the evolution of the eye lens $\beta\gamma$-crystallin domain fold. *Structure*, 9(2):115–124, 2001.

[77] Alessandro Vergara, Marco Grassi, Filomena Sica, Elio Pizzo, Giuseppe D'Alessio, Lelio Mazzarella, and Antonello Merlino. A novel interdomain interface in crystallins: structural characterization of the $\beta\gamma$-crystallin from *Geodia cydonium* at 0.99 Å resolution. *Acta Crystallographica Section D*, 69(6):960–967, 2013.

[78] Sudhir Kumar, Glen Stecher, and Koichiro Tamura. MEGA7: molecular evolutionary genetics analysis version 7.0 for bigger datasets. *Molecular Biology and Evolution*, 33(7):1870–1874, 2016.

[79] Robert C Edgar. MUSCLE: multiple sequence alignment with high accuracy and high throughput. *Nucleic acids research*, 32(5):1792–1797, 2004.

[80] Sergei L Kosakovsky Pond and Spencer V Muse. HyPhy: hypothesis testing using phylogenies. In *Statistical Methods in Molecular Evolution*, pages 125–181. Springer, 2005.

[81] Leigh Willard, Anuj Ranjan, Haiyan Zhang, Hassan Monzavi, Robert F Boyko, Brian D Sykes, and David S Wishart. VADAR: a web server for quantitative evaluation of protein structure quality. *Nucleic Acids Research*, 31(13):3316–3319, 2003.

[82] Hilmar Ebersbach, Erik Fiedler, Tanja Scheuermann, Markus Fiedler, Milton T Stubbs, Carola Reimann, Gabriele Proetzel, Rainer Rudolph, and Ulrike Fiedler. Affilin–novel binding molecules based on human γ-B-crystallin, an all β-sheet protein. *Journal of Molecular Biology*, 372(1):172–185, 2007.

[83] Karuna Dixit, Ajay Pande, Jayanti Pande, and Siddhartha P Sarma. Nuclear magnetic resonance structure of a major lens protein, human γC-crystallin: Role of the dipole moment in protein solubility. *Biochemistry*, 55(22):3136–3149, 2016.

[84] Ajit Basak, Orval Bateman, Christine Slingsby, Ajay Pande, Neer Asherie, Olutayo Ogun, George B Benedek, and Jayanti Pande. High-resolution x-ray crystal structures of human γd crystallin (1.25 å) and the r58h mutant (1.15 å) associated with aculeiform cataract. *Journal of molecular biology*, 328(5):1137–1147, 2003.

[85] William D Brubaker and Rachel W Martin. 1 h, 13 c, and 15 n assignments of wild-type human γs-crystallin and its cataract-related variant γs-g18v. *Biomolecular NMR Assignments*, 6(1):63–67, 2012.

[86] Yang Zhang. I-TASSER server for protein 3D structure prediction. *BMC bioinformatics*, 9(1):40, 2008.

[87] F William Studier. Protein production by auto-induction in high-density shaking cultures. *Protein expression and purification*, 41(1):207–234, 2005.

[88] David C Thorn, Aidan B Grosas, Peter D Mabbitt, Nicholas J Ray, Colin J Jackson, and John A Carver. The structure and stability of the disulfide-linked γs-crystallin dimer provide insight into oxidation products associated with lens cataract formation. *Journal of molecular biology*, 431(3):483–497, 2019.

[89] Peter G Hains and Roger JW Truscott. Post-translational modifications in the nuclear region of young, aged, and cataract human lenses. *Journal of Proteome Research*, 6(10):3935–3943, 2007.

[90] PA Wilmarth, S Tanner, S Dasari, SR Nagalla, MA Riviere, V Bafna, PA Pevzner, and LL David. Age-related changes in human crystallins determined from comparative analysis of post-translational modifications in young and aged lens: does deamidation contribute to crystallin insolubility? *Journal of Proteome Research*, 5(10):2554–2566, 2006.

[91] Ashraf G Madian and Fred E Regnier. Proteomic identification of carbonylated proteins and their oxidation sites. *Journal of Proteome Research*, 9(8):3766–3780, 2010.

[92] Andrew R Pitt and Corinne M Spickett. Mass spectrometric analysis of HOCl-and free-radical-induced damage to lipids and proteins. *Biochemical Society Transactions*, 36:1077–1082, 2008.

[93] H Sun, Z Ma, Y Li, B Liu, Z Li, X Ding, Y Gao, W Ma, X Tang, X Li, et al. Gamma-s crystallin gene (crygs) mutation causes dominant progressive cortical cataract in humans. *Journal of Medical Genetics*, 42(9):706–710, 2005.

[94] Ramachandran Ramya Devi, Wenliang Yao, Perumalsamy Vijayalakshmi, Yuri V Sergeev, Periasamy Sundaresan, and J Fielding Hejtmancik. Crystallin gene mutations in Indian families with inherited pediatric cataract. *Molecular Vision*, 14:1157–1170, 2008.

[95] Venkata Pulla Rao Vendra, Ismail Khan, Sushil Chandani, Anbukkarasi Muniyandi, and Dorairajan Balasubramanian. Gamma crystallins of the human eye lens. *Biochimica et Biophysica Acta (BBA)-General Subjects*, 1860(1):333–343, 2016.

[96] Fangling Ji, Jinwon Jung, and Angela M Gronenborn. Structural and biochemical characterization of the childhood cataract-associated R76S mutant of human γD-crystallin. *Biochemistry*, 51(12):2588–2596, 2012.

[97] Shashi Kumar Suman, Amita Mishra, Daddali Ravindra, Lahari Yeramala, and Yogendra Sharma. Evolutionary remodelling of the betagamma-crystallins for domain stability at the cost of Ca^{2+}-binding. *Journal of Biological Chemistry*, 8:jbc–M111, 2011.

[98] Shashi Kumar Suman, Amita Mishra, Lahari Yeramala, Ishan Das Rastogi, and Yogendra Sharma. Disability for function: loss of Ca^{2+}-binding is obligatory for fitness of mammalian $\beta\gamma$-crystallins. *Biochemistry*, 52(50):9047–9058, 2013.

[99] Shanti Swaroop Srivastava, Amita Mishra, Bal Krishnan, and Yogendra Sharma. Ca^{2+}-binding motif of $\beta\gamma$-crystallins. *Journal of Biological Chemistry*, 289(16):10958–10966, 2014.

[100] KA Kozlov. Vertebrate crystallins–from proteins to genes. *Russian Journal of Developmental Biology*, 32(5):265–282, 2001.

[101] Nanjiang Shu, Tuping Zhou, and Sven Hovmöller. Prediction of zinc-binding sites in proteins from sequence. *Bioinformatics*, 24(6):775–782, 2008.

[102] J Keenan, DF Orr, and BK Pierscionek. Patterns of crystallin distribution in porcine eye lenses. *Molecular Vision*, 14:1245–1253, 2008.

[103] Yingwei Chen, Huaying Zhao, Peter Schuck, and Graeme Wistow. Solution properties of γ-crystallins: Compact structure and low frictional ratio are conserved properties of diverse γ-crystallins. *Protein Science*, 23(1):76–87, 2014.

[104] Eugene Serebryany, Shuhuai Yu, Sunia A Trauger, Bogdan Budnik, and Eugene I Shakhnovich. Dynamic disulfide exchange in a crystallin protein in the human eye lens promotes cataract-associated aggregation. *Journal of Biological Chemistry*, 293(46):17997–18009, 2018.

[105] Veniamin N Lapko, David L Smith, and Jean B Smith. Methylation and carbamylation of human γ-crystallins. *Protein Science*, 12(8):1762–1774, 2003.

[106] Sergei L Kosakovsky Pond and Simon DW Frost. Not so different after all: a comparison of methods for detecting amino acid sites under selection. *Molecular Biology and Evolution*, 22(5):1208–1222, 2005.

[107] F Timur Senguen and Zenon Grabarek. X-ray structures of magnesium and manganese complexes with the N-terminal domain of calmodulin: insights into the mechanism and specificity of metal ion binding to an EF-hand. *Biochemistry*, 51(31):6182–6194, 2012.

[108] Anita Lewit-Bentley and Stéphane Réty. Ef-hand calcium-binding proteins. *Current Opinion in Structural Biology*, 10(6):637–643, 2000.

[109] Mitsunori Fukuda, Toshio Kojima, and Katsuhiko Mikoshiba. Regulation by bivalent cations of phospholipid binding to the C2A domain of synaptotagmin iii. *Biochemical Journal*, 323(2):421–425, 1997.

[110] M Teintze, M Inouye, and S Inouye. Characterization of calcium-binding sites in development-specific protein S of *Myxococcus xanthus* using site-specific mutagenesis. *Journal of Biological Chemistry*, 263(3):1199–1203, 1988.

[111] Maroor K Jobby and Yogendra Sharma. Calcium-binding crystallins from *Yersinia pestis*: characterization of two single $\beta\gamma$-crystallin domains of a putative exported protein. *Journal of Biological Chemistry*, 280(2):1209–1216, 2005.

[112] M. Feng, D. Patel, JJ. Dervan, T. Ceska, D. Suck, I. Haq, and J.R. Sayers. Roles of divalent metal ions in flap endonuclease–substrate interactions. *Nature Structural and Molecular Biology*, 11:450–456, 2004.

[113] Yang Chao and Dax Fu. Thermodynamic studies of the mechanism of metal binding to the *Escherichia coli* zinc transporter YiiP. *Journal of Biological Chemistry*, 279:17173–17180, 2004.

[114] Pijush Basak, Tanay Debnath, Rajat Banerjee, and Maitree Bhattacharyya. Selective binding of divalent cations toward heme proteins. *Frontiers in Biology*, 11(1):32–42, 2016.

[115] G. Bodenhausen and D.J. Ruben. Natural abundance nitrogen-15 NMR by enhanced heteronuclear spectroscopy. *Chemical Physics Letters*, 69(1):185–189, 1980.

[116] Masayuki Nara, Masaru Tanokura, Tatsuyuki Yamamoto, and Mitsuo Tasumi. A comparative study of the binding effects of Mg^{2+}, Ca^{2+}, Sr^{2+}, and Cd^{2+} on calmodulin by fourier-transform infrared spectroscopy. *Biospectroscopy*, 1(1):47–54, 1995.

[117] Sheng Hao Chao, Yasuhiro Suzuki, JOHN R Zysk, and WY Cheung. Activation of calmodulin by various metal cations as a function of ionic radius. *Molecular Pharmacology*, 26(1):75–82, 1984.

[118] Takeaki Ozawa, Kazuki Sasaki, and Yoshio Umezawa. Metal ion selectivity for formation of the calmodulin–metal–target peptide ternary complex studied by surface plasmon resonance spectroscopy. *Biochimica et Biophysica Acta - Protein Structure and Molecular Enzymology*, 1434(2):211–220, 1999.

[119] Aaron P Yamniuk, Leonard T Nguyen, Tung T Hoang, and Hans J Vogel. Metal ion binding properties and conformational states of calcium-and integrin-binding protein. *Biochemistry*, 43(9):2558–2568, 2004.

[120] Aaron P Yamniuk, Dylan M Silver, Kathryn L Anderson, Stephen R Martin, and Hans J Vogel. Domain stability and metal-induced folding of calcium-and integrin-binding protein 1. *Biochemistry*, 46(24):7088–7098, 2007.

[121] Yves Blancuzzi, Andre Padilla, Adrien Cave, and Joseph Parello. Symmetrical rearrangement of the cation-binding sites of parvalbumin upon calcium/magnesium exchange. a study by proton 2D NMR. *Biochemistry*, 32(5):1302–1309, 1993.

[122] Melissa S Kosinski-Collins, Shannon L Flaugh, and Jonathan King. Probing folding and fluorescence quenching in human γd crystallin greek key domains using triple tryptophan mutant proteins. *Protein Science*, 13(8):2223–2235, 2004.

[123] Shannon L Flaugh, Melissa S Kosinski-Collins, and Jonathan King. Contributions of hydrophobic domain interface interactions to the folding and stability of human γd-crystallin. *Protein Science*, 14(3):569–581, 2005.

[124] Zhiwei Ma, Grzegorz Piszczek, Paul T Wingfield, Yuri V Sergeev, and J Fielding Hejtmancik. The g18v crygs mutation associated with human cataracts increases γs-crystallin sensitivity to thermal and chemical stress. *Biochemistry*, 48(30):7334–7341, 2009.

[125] William D Brubaker, J Alfredo Freites, Kory J Golchert, Rebecca A Shapiro, Vasilios Morikis, Douglas J Tobias, and Rachel W Martin. Separating instability from aggregation propensity in γs-crystallin variants. *Biophysical Journal*, 100(2):498–506, 2011.

[126] Damien Ray, Nicholas J.and Hall and John A. Carver. Deamidation of N76 in human γS-crystallin promotes dimer formation. *Biochimica et Biophysica Acta (BBA) - General Subjects*, 1860(1, Part B):315–324, 2016.

[127] Vladislav Victorovich Khrustalev, Eugene Victorovich Barkovsky, and Tatyana Aleksandrovna Khrustaleva. Magnesium and manganese binding sites on proteins have the same predominant motif of secondary structure. *Journal of Theoretical Biology*, 395:174–185, 2016.

[128] Robert D Shannon. Revised effective ionic radii and systematic studies of interatomic distances in halides and chalcogenides. *Acta Crystallographica Section A*, 32(5):751–767, 1976.

[129] Ralph G Pearson. Hard and soft acids and bases. *Journal of the American Chemical Society*, 85(22):3533–3539, 1963.

[130] K. Hsin, Y. Sheng, M.M. Harding, P. Taylor, and M.D. Walkinshaw. MESPEUS: a database of the geometry of metal sites in proteins. *Journal of Applied Crystallography*, 41(5):963–968, 2008.

[131] Minko Dudev, Jonathan Wang, Todor Dudev, and Carmay Lim. Factors governing the metal coordination number in metal complexes from Cambridge Structural Database analyses. *The Journal of Physical Chemistry B*, 110(4):1889–1895, 2006.

[132] Marjorie M Harding. Geometry of metal–ligand interactions in proteins. *Acta Crystallographica Section D*, 57(3):401–411, 2001.

[133] Priya R Banerjee, Ajay Pande, Alexander Shekhtman, and Jayanti Pande. Molecular mechanism of the chaperone function of mini-α-crystallin, a 19-residue peptide of human α-crystallin. *Biochemistry*, 54(2):505–515, 2014.

[134] Domarin Khago, Eric K Wong, Carolyn N Kingsley, J Alfredo Freites, Douglas J Tobias, and Rachel W Martin. Increased hydrophobic surface exposure in the cataract-related g18v variant of human γs-crystallin. *Biochimica et Biophysica Acta (BBA)-General Subjects*, 1860(1):325–332, 2016.

[135] José A Domínguez-Calva, Cameron Haase-Pettingell, Eugene Serebryany, Jonathan A King, and Liliana Quintanar. A histidine switch for Zn-induced aggregation of γ-crystallins reveals a metal-bridging mechanism relevant to cataract disease. *Biochemistry*, 57(33):4959–4962, 2018.

[136] Per P Fagerholm, Bo T Philipson, and Bo Lindström. Normal human lens?the distribution of protein. *Experimental eye research*, 33(6):615–620, 1981.

[137] Jiejin Chen, Dmitri Toptygin, Ludwig Brand, and Jonathan King. Mechanism of the efficient tryptophan fluorescence quenching in human γd-crystallin studied by time-resolved fluorescence. *Biochemistry*, 47(40):10705–10721, 2008.

[138] Frank J Giblin. Glutathione: a vital lens antioxidant. *Journal of Ocular Pharmacology and Therapeutics*, 16(2):121–135, 2000.

[139] Kirsten J Lampi, Phillip A Wilmarth, Matthew R Murray, and Larry L David. Lens β-crystallins: the role of deamidation and related modifications in aging and cataract. *Progress in biophysics and molecular biology*, 115(1):21–31, 2014.

[140] Veronica Harrington, Shantis McCall, Sy Huynh, Kiran Srivastava, and Om P Srivastava. Crystallins in water soluble-high molecular weight protein fractions and water insoluble protein fractions in aging and cataractous human lenses. *Mol Vis*, 10(61):476–489, 2004.

[141] Noriko Fujii, Yuko Momose, Yoshihiro Ishibashi, Toshimasa Uemura, Masatoshi Takita, and Makoto Takehana. Specific racemization and isomerization of the aspartyl residue of αa-crystallin due to uv-b irradiation. *Experimental eye research*, 65(1):99–104, 1997.

[142] Michelle Yu Sung Hooi, Mark J Raftery, and Roger John Willis Truscott. Racemization of two proteins over our lifespan: deamidation of asparagine 76 in γs crystallin is greater in cataract than in normal lenses across the age range. *Investigative ophthalmology & visual science*, 53(7):3554–3561, 2012.

[143] Peter G Hains and Roger JW Truscott. Proteomic analysis of the oxidation of cysteine residues in human age-related nuclear cataract lenses. *Biochimica et Biophysica Acta (BBA)-Proteins and Proteomics*, 1784(12):1959–1964, 2008.

[144] S Zigman. Environmental near-uv radiation and cataracts. *Ophthalmic Literature*, 3(49):182, 1996.

[145] M Balaji, K Sasikala, and T Ravindran. Copper levels in human mixed, nuclear brunescence, and posterior subcapsular cataract. *British journal of ophthalmology*, 76(11):668–669, 1992.

[146] Péter Rácz and Mary Ördögh. Investigations on trace elements in normal and senile cataractous lenses. *Albrecht von Graefes Archiv für klinische und experimentelle Ophthalmologie*, 204(1):67–72, 1977.

[147] Anzar Ahmad, Imtiaz Ahmad, Moazzam A Khan, Alia B Munshi, Ishratullah Siddiqui, Ovais Anzar, and Alvina Anzar. On-set of cataract and accumulation of copper, lead and cadmium in smokers of karachi, pakistan. *Journal of Environmental & Analytical Toxicology*, 5(2):1, 2015.

[148] Alex Langford-Smith, Viranga Tilakaratna, Paul R Lythgoe, Simon J Clark, Paul N Bishop, and Anthony J Day. Age and smoking related changes in metal ion levels in human lens: implications for cataract formation. *PloS one*, 11(1):e0147576, 2016.

[149] K.W. Roskamp, N. Kozlyuk, S. Sengupta, and R.W. Martin. Divalent cations interactions with $\beta\gamma$-crystallins are function dependent. *Biochemistry*.

[150] Brian J Tabner, Stuart Turnbull, OMA El-Aganf, and David Allsop. Production of reactive oxygen species from aggregating proteins implicated in alzheimer's disease, parkinson's disease and other neurodegenerative diseases. *Current topics in medicinal chemistry*, 1(6):507–517, 2001.

[151] Shanmugam Manoharan, Gilles J Guillemin, Rajagopal Selladurai Abiramasundari, Musthafa Mohamed Essa, Mohammed Akbar, and Mohammed D Akbar. The role of reactive oxygen species in the pathogenesis of alzheimer?s disease, parkinson?s disease, and huntington?s disease: a mini review. *Oxidative Medicine and Cellular Longevity*, 2016, 2016.

[152] Andrés Binolfi, Liliana Quintanar, Carlos W Bertoncini, Christian Griesinger, and Claudio O Fernández. Bioinorganic chemistry of copper coordination to alpha-synuclein: Relevance to parkinson's disease. *Coordination Chemistry Reviews*, 256(19-20):2188–2201, 2012.

[153] Xiaoyan Wang, Dima Moualla, Josephine A Wright, and David R Brown. Copper binding regulates intracellular alpha-synuclein localisation, aggregation and toxicity. *Journal of neurochemistry*, 113(3):704–714, 2010.

[154] Ashley I Bush. The metallobiology of alzheimer's disease. *Trends in neurosciences*, 26(4):207–214, 2003.

[155] Peter Faller, Christelle Hureau, and Giovanni La Penna. Metal ions and intrinsically disordered proteins and peptides: from cu/zn amyloid-β to general principles. *Accounts of chemical research*, 47(8):2252–2259, 2014.

[156] Fabio Arnesano, Simone Scintilla, Vincenza Calò, Elena Bonfrate, Chiara Ingrosso, Maurizio Losacco, Teresa Pellegrino, Enrico Rizzarelli, and Giovanni Natile. Copper-triggered aggregation of ubiquitin. *PloS one*, 4(9):e7052, 2009.

[157] Olga V Bocharova, Leonid Breydo, Vadim V Salnikov, and Ilia V Baskakov. Copper (ii) inhibits in vitro conversion of prion protein into amyloid fibrils. *Biochemistry*, 44(18):6776–6787, 2005.

[158] Lian-Xiu Zhou, Jin-Tang Du, Zhi-Yang Zeng, Wei-Hui Wu, Yu-Fen Zhao, Kenji Kanazawa, Yasuko Ishizuka, Tadashi Nemoto, Hiroshi Nakanishi, and Yan-Mei Li. Copper (ii) modulates in vitro aggregation of a tau peptide. *Peptides*, 28(11):2229–2234, 2007.

[159] Xiaohui Wang, Claudia M Garcia, Ying-Bo Shui, and David C Beebe. Expression and regulation of α-, β-, and γ-crystallins in mammalian lens epithelial cells. *Investigative ophthalmology & visual science*, 45(10):3608–3619, 2004.

[160] Noah E Robinson, Kirsten J Lampi, J Paul Speir, Gary Kruppa, Michael Easterling, and Arthur B Robinson. Quantitative measurement of young human eye lens crystallins by direct injection fourier transform ion cyclotron resonance mass spectrometry. *Mol Vis*, 12:704–11, 2006.

[161] Roland J Siezen, John A Thomson, Elizabeth D Kaplan, and George B Benedek. Human lens gamma-crystallins: isolation, identification, and characterization of the expressed gene products. *Proceedings of the National Academy of Sciences*, 84(17):6088–6092, 1987.

[162] Ajay Pande, Onofrio Annunziata, Neer Asherie, Olutayo Ogun, George B Benedek, and Jayanti Pande. Decrease in protein solubility and cataract formation caused by the pro23 to thr mutation in human γd-crystallin. *Biochemistry*, 44(7):2491–2500, 2005.

[163] Srinivasu Karri, Ramesh Babu Kasetti, Venkata Pulla Rao Vendra, Sushil Chandani, and Dorairajan Balasubramanian. Structural analysis of the mutant protein d26g of human γs-crystallin, associated with coppock cataract. *Molecular Vision*, 19:1231, 2013.

[164] Somireddy Venkata Bharat, Alexander Shekhtman, and Jayanti Pande. The cataract-associated v41m mutant of human γs-crystallin shows specific structural changes that directly enhance local surface hydrophobicity. *Biochemical and Biophysical Research Communications*, 443(1):110–114, 2014.

[165] Venkata Pulla Rao Vendra, Sushil Chandani, and Dorairajan Balasubramanian. The mutation v42m distorts the compact packing of the human gamma-s-crystallin molecule, resulting in congenital cataract. *PLoS One*, 7(12):e51401, 2012.

[166] Fangling Ji, Jinwon Jung, Leonardus MI Koharudin, and Angela M Gronenborn. The human w42r γD-crystallin mutant structure provides a link between congenital and age-related cataracts. *Journal of Biological Chemistry*, 288(1):99–109, 2013.

[167] Venu Talla, Chitra Narayanan, Narayanaswamy Srinivasan, and Dorairajan Balasubramanian. Mutation causing self-aggregation in human γc-crystallin leading to congenital cataract. *Investigative ophthalmology & visual science*, 47(12):5212–5217, 2006.

[168] Daumantas Matulis, Christoph G Baumann, Victor A Bloomfield, and Rex E Lovrien. 1-anilino-8-naphthalene sulfonate as a protein conformational tightening agent. *Biopolymers: Original Research on Biomolecules*, 49(6):451–458, 1999.

[169] Eugene Serebryany. Wt human γD crystallin promotes aggregation of its oxidation-mimicking mutants. *Biophysical Journal*, 110(3):387a–388a, 2016.

[170] Zhiguang Xiao, Jens Brose, Sonja Schimo, Susan M Ackland, Sharon La Fontaine, and Anthony G Wedd. Unification of the copper (i) binding affinities of the metallochaperones atx1, atox1, and related proteins detection probes and affinity standards. *Journal of Biological Chemistry*, 286(13):11047–11055, 2011.

[171] Artur Kr?żel, Wojciech Leśniak, Małgorzata Jeżowska-Bojczuk, Piotr Młynarz, Justyna Brasuñ, Henryk Kozłowski, and Wojciech Bal. Coordination of heavy metals by dithiothreitol, a commonly used thiol group protectant. *Journal of inorganic biochemistry*, 84(1-2):77–88, 2001.

[172] J Wu, FC Hsu, and SD Cunningham. Chelate-assisted pb phytoextraction: Pb availability, uptake, and translocation constraints. *Environmental Science & Technology*, 33(11):1898–1904, 1999.

[173] Rahul Mahadev Shelake, Yuki Ito, Junya Masumoto, Eugene Hayato Morita, and Hidenori Hayashi. A novel mechanism of ?metal gel-shift? by histidine-rich ni2+-binding hpn protein from helicobacter pylori strain ss1. *PloS one*, 12(2):e0172182, 2017.

[174] Eugene Serebryany and Jonathan A King. The $\beta\gamma$-crystallins: native state stability and pathways to aggregation. *Progress in Biophysics and Molecular Biology*, 115(1):32–41, 2014.

[175] Mireille Delaye and Annette Tardieu. Short-range order of crystallin proteins accounts for eye lens transparency. *Nature*, 302(5907):415, 1983.

[176] Annette Tardieu, Françoise Vérétout, Brigitte Krop, and Christine Slingsby. Protein interactions in the calf eye lens: interactions between β-crystallins are repulsive whereas in γ-crystallins they are attractive. *European Biophysics Journal*, 21(1):1–12, 1992.

[177] Aileen Sandilands, Aileen M Hutcheson, Heather A Long, Alan R Prescott, Gijs Vrensen, Jana Löster, Norman Klopp, Raimund B Lutz, Jochen Graw, Shigeo Masaki, et al. Altered aggregation properties of mutant γ-crystallins cause inherited cataract. *The EMBO Journal*, 21(22):6005–6014, 2002.

[178] Juliet A Moncaster, Roberto Pineda, Robert D Moir, Suqian Lu, Mark A Burton, Joy G Ghosh, Maria Ericsson, Stephanie J Soscia, Anca Mocofanescu, Rebecca D Folkerth, et al. Alzheimer's disease amyloid-β links lens and brain pathology in down syndrome. *PloS One*, 5(5):e10659, 2010.

[179] Lee E Goldstein, Julien A Muffat, Robert A Cherny, Robert D Moir, Maria H Ericsson, Xudong Huang, Christine Mavros, Jennifer A Coccia, Kyle Y Faget, Karlotta A Fitch, et al. Cytosolic β-amyloid deposition and supranuclear cataracts in lenses from people with alzheimer's disease. *The Lancet*, 361(9365):1258–1265, 2003.

[180] Peter H Frederikse. Amyloid-like protein structure in mammalian ocular lenses. *Current Eye Research*, 20(6):462–468, 2000.

[181] Ralph Michael, Jurja Rosandić, Gustavo A Montenegro, Elvira Lobato, Francisco Tresserra, Rafael I Barraquer, and Gijs FJM Vrensen. Absence of beta-amyloid in cortical cataracts of donors with and without alzheimer's disease. *Experimental Eye Research*, 106:5–13, 2013.

[182] Yongting Wang, Sarah Petty, Amy Trojanowski, Kelly Knee, Daniel Goulet, Ishita Mukerji, and Jonathan King. Formation of amyloid fibrils in vitro from partially unfolded intermediates of human γc-crystallin. *Investigative Ophthalmology & Visual Science*, 51(2):672–678, 2010.

[183] Katerina Papanikolopoulou, Ishara Mills-Henry, Shannon L Thol, Yongting Wang, Abby AR Gross, Daniel A Kirschner, Sean M Decatur, and Jonathan King. Formation of amyloid fibrils in vitro by human γd-crystallin and its isolated domains. *Molecular Vision*, 14:81, 2008.

[184] Melissa S Kosinski-Collins and Jonathan King. In vitro unfolding, refolding, and polymerization of human γd crystallin, a protein involved in cataract formation. *Protein Science*, 12(3):480–490, 2003.

[185] Sean D Moran, Tianqi O Zhang, Sean M Decatur, and Martin T Zanni. Amyloid fiber formation in human γd-crystallin induced by uv–b photodamage. *Biochemistry*, 52(36):6169–6181, 2013.

[186] Sean D Moran, Tianqi O Zhang, and Martin T Zanni. An alternative structural isoform in amyloid-like aggregates formed from thermally denatured human γd-crystallin. *Protein Science*, 23(3):321–331, 2014.

[187] Sean D Moran, Sean M Decatur, and Martin T Zanni. Structural and sequence analysis of the human γd-crystallin amyloid fibril core using 2d ir spectroscopy, segmental 13c labeling, and mass spectrometry. *Journal of the American Chemical Society*, 134(44):18410–18416, 2012.

[188] Fabrizio Chiti and Christopher M Dobson. Protein misfolding, functional amyloid, and human disease. *Annu. Rev. Biochem.*, 75:333–366, 2006.

[189] David R Booth, Margaret Sunde, Vittorio Bellotti, Carol V Robinson, Winston L Hutchinson, Paul E Fraser, Philip N Hawkins, Christopher M Dobson, Sheena E Radford, Colin CF Blake, et al. Instability, unfolding and aggregation of human lysozyme variants underlying amyloid fibrillogenesis. *Nature*, 385(6619):787, 1997.

[190] MB Pepys, PN Hawkins, DR Booth, DM Vigushin, GA Tennent, AK Soutar, N Totty, O Nguyen, CCF Blake, CJ Terry, et al. Human lysozyme gene mutations cause hereditary systemic amyloidosis. *Nature*, 362(6420):553, 1993.

[191] Sarah Meehan, Yoke Berry, Ben Luisi, Christopher M Dobson, John A Carver, and Cait E MacPhee. Amyloid fibril formation by lens crystallin proteins and its implications for cataract formation. *Journal of Biological Chemistry*, 279(5):3413–3419, 2004.

[192] Rita Cacace, Kristel Sleegers, and Christine Van Broeckhoven. Molecular genetics of early-onset alzheimer's disease revisited. *Alzheimer's & Dementia*, 12(6):733–748, 2016.

[193] Linus Pauling, Harvey A Itano, Seymour J Singer, and Ibert C Wells. Sickle cell anemia, a molecular disease. *Science*, 110(2865):543–548, 1949.

[194] Fabrizio Chiti and Christopher M Dobson. Amyloid formation by globular proteins under native conditions. *Nature Chemical Biology*, 5(1):15, 2009.

[195] Catherine M Eakin, Frank J Attenello, Charles J Morgan, and Andrew D Miranker. Oligomeric assembly of native-like precursors precedes amyloid formation by β-2 microglobulin. *Biochemistry*, 43(24):7808–7815, 2004.

[196] Anna Sanders, C Jeremy Craven, Lee D Higgins, Silva Giannini, Matthew J Conroy, Andrea M Hounslow, Jonathan P Waltho, and Rosemary A Staniforth. Cystatin forms a tetramer through structural rearrangement of domain-swapped dimers prior to amyloidogenesis. *Journal of Molecular Biology*, 336(1):165–178, 2004.

[197] Yanshun Liu, Giovanni Gotte, Massimo Libonati, and David Eisenberg. A domain-swapped rnase a dimer with implications for amyloid formation. *Nature Structural & Molecular Biology*, 8(3):211, 2001.

[198] Neeti Sinha, Chung-Jung Tsai, and Ruth Nussinov. A proposed structural model for amyloid fibril elongation: domain swapping forms an interdigitating β-structure polymer. *Protein Engineering*, 14(2):93–103, 2001.

[199] Aaron Kerman, Hsueh-Ning Liu, Sidney Croul, Juan Bilbao, Ekaterina Rogaeva, Lorne Zinman, Janice Robertson, and Avijit Chakrabartty. Amyotrophic lateral sclerosis is a non-amyloid disease in which extensive misfolding of sod1 is unique to the familial form. *Acta Neuropathologica*, 119(3):335–344, 2010.

[200] Venkata Pulla Rao Vendra, Garima Agarwal, Sushil Chandani, Venu Talla, Narayanaswamy Srinivasan, and Dorairajan Balasubramanian. Structural integrity of the greek key motif in $\beta\gamma$-crystallins is vital for central eye lens transparency. *PloS One*, 8(8):e70336, 2013.

[201] Wang Zhang, Hong-Chen Cai, Fei-Feng Li, Yi-Bo Xi, Xu Ma, and Yong-Bin Yan. The congenital cataract-linked g61c mutation destabilizes γd-crystallin and promotes non-native aggregation. *PLoS One*, 6(5):e20564, 2011.

[202] Ismail Khan, Sushil Chandani, and Dorairajan Balasubramanian. Structural study of the g57w mutant of human gamma-s-crystallin, associated with congenital cataract. *Molecular Vision*, 22:771, 2016.

[203] Konstantin O Muranov, Olga I Maloletkina, Nikolay B Poliansky, Kira A Markossian, Sergey Yu Kleymenov, Sergey P Rozhkov, Andrei S Goryunov, Michail A Ostrovsky, and Boris I Kurganov. Mechanism of aggregation of uv-irradiated βl-crystallin. *Experimental Eye Research*, 92(1):76–86, 2011.

[204] RAYMOND F BORKMAN, Grady Knight, and Bettie Obi. The molecular chaperone α-crystallin inhibits uv-induced protein aggregation. *Experimental Eye Research*, 62(2):141–148, 1996.

[205] Kate L Moreau and Jonathan A King. Protein misfolding and aggregation in cataract disease and prospects for prevention. *Trends in Molecular Medicine*, 18(5):273–282, 2012.

[206] Magalie Michiel, Elodie Duprat, Fériel Skouri-Panet, Jason A Lampi, Annette Tardieu, Kirsten J Lampi, and Stéphanie Finet. Aggregation of deamidated human βb2-crystallin and incomplete rescue by α-crystallin chaperone. *Experimental Eye Research*, 90(6):688–698, 2010.

[207] Kerri Mafia, Ratna Gupta, Marion Kirk, L Wilson, OP Srivastava, and Stephen Barnes. Uv-a-induced structural and functional changes in human lens deamidated αb-crystallin. *Molecular Vision*, 14:234, 2008.

[208] SS-S. Wang and W-S Wen. Examining the influence of ultraviolet c irradiation on recombinant human γd-crystallin. *Molecular Vision*, 16:2777–2790, 2010.

[209] SEYMOUR Zigman. Environmental near-uv radiation and cataracts. *Optometry and Vision Science*, 72(12):899–901, 1995.

[210] GJ Bessems, E Keizer, J Wollensak, and HJ Hoenders. Non-tryptophan fluorescence of crystallins from normal and cataractous human lenses. *Investigative Ophthalmology & Visual Science*, 28(7):1157–1163, 1987.

[211] RJW Truscott. Human cataract: the mechanisms responsible; light and butterfly eyes. *The International Journal of Biochemistry & Cell Biology*, 35(11):1500–1504, 2003.

[212] Melanie R Nilsson. Techniques to study amyloid fibril formation in vitro. *Methods*, 34(1):151–160, 2004.

[213] Ming Xu, Vladimir V Ermolenkov, Vladimir N Uversky, and Igor K Lednev. Hen egg white lysozyme fibrillation: a deep-uv resonance raman spectroscopic study. *Journal of Biophotonics*, 1(3):215–229, 2008.

[214] Robert J Chalkley, Kirk C Hansen, and Michael A Baldwin. Bioinformatic methods to exploit mass spectrometric data for proteomic applications. *Methods in Enzymology*, 402:289–312, 2005.

[215] Dong-Yun Li, Raymond F Borkman, Ren-Hong Wang, and James Dillon. Mechanisms of photochemically produced turbidity in lens protein solutions. *Experimental Eye Research*, 51(6):663–669, 1990.

[216] Aabgeena Naeem and Naveed Ahmad Fazili. Defective protein folding and aggregation as the basis of neurodegenerative diseases: the darker aspect of proteins. *Cell Biochemistry and Biophysics*, 61(2):237–250, 2011.

[217] Eugene Serebryany, Takumi Takata, Erika Erickson, Nathaniel Schafheimer, Yongting Wang, and Jonathan A King. Aggregation of trp¿ glu point mutants of human gammad crystallin provides a model for hereditary or uv-induced cataract. *Protein Science*, 25(6):1115–1128, 2016.

[218] Roger JW Truscott. Age-related nuclear cataract?oxidation is the key. *Experimental Eye Research*, 80(5):709–725, 2005.

[219] Manni Luthra and D Balasubramanian. Nonenzymatic glycation alters protein structure and stability. a study of two eye lens crystallins. *Journal of Biological Chemistry*, 268(24):18119–18127, 1993.

[220] S.R. Hanson, D.L. Smith, and J.B. Smith. Deamidation and disulfide bonding in human lens γ-crystallins. *Experimental Eye Research*, 67(3):301–312, 1998.

[221] Xiao-Qiao Li, Hong-Chen Cai, Shi-Yi Zhou, Ju-Hua Yang, Yi-Bo Xi, Xiao-Bo Gao, Wei-Jie Zhao, Peng Li, Guang-Yu Zhao, Yi Tong, et al. A novel mutation impairing the tertiary structure and stability of γc-crystallin (crygc) leads to cataract formation in humans and zebrafish lens. *Human Mutation*, 33(2):391–401, 2012.

[222] Yung Hae Kim, Deborah M Kapfer, Jos Boekhorst, Nicolette H Lubsen, Hans Peter Bächinger, Thomas R Shearer, Larry L David, Jimmy B Feix, and Kirsten J Lampi. Deamidation, but not truncation, decreases the urea stability of a lens structural protein, βb1-crystallin. *Biochemistry*, 41(47):14076–14084, 2002.

[223] Kirsten J Lampi, Kencee K Amyx, Petra Ahmann, and Eric A Steel. Deamidation in human lens βb2-crystallin destabilizes the dimer. *Biochemistry*, 45(10):3146–3153, 2006.

[224] Takumi Takata, Julie T Oxford, Theodore R Brandon, and Kirsten J Lampi. Deamidation alters the structure and decreases the stability of human lens βa3-crystallin. *Biochemistry*, 46(30):8861–8871, 2007.

[225] Stacy RA Hanson, Azeem Hasan, David L Smith, and Jean B Smith. The major in vivo modifications of the human water-insoluble lens crystallins are disulfide bonds, deamidation, methionine oxidation and backbone cleavage. *Experimental Eye Research*, 71(2):195–207, 2000.

[226] Peter G Hains and Roger JW Truscott. Age-dependent deamidation of lifelong proteins in the human lens. *Investigative Ophthalmology & Visual Science*, 51(6):3107–3114, 2010.

[227] Ling Fu and Jack J-N Liang. Conformational change and destabilization of cataract γC-crystallin T5P mutant. *FEBS Letters*, 513(2-3):213–216, 2002.

[228] Vilius Pigaga and Roy A Quinlan. Lenticular chaperones suppress the aggregation of the cataract-causing mutant T5P γC-crystallin. *Experimental Cell Research*, 312(1):51–62, 2006.

[229] Jack J-N Liang. Interactions and chaperone function of αa-crystallin with T5P γC-crystallin mutant. *Protein Science*, 13(9):2476–2482, 2004.

[230] Ling Fu and Jack J-N Liang. Alteration of protein–protein interactions of congenital cataract crystallin mutants. *Investigative Ophthalmology & Visual Science*, 44(3):1155–1159, 2003.

[231] Chitra Kannabiran and Vanita Vanita. Genetics of cataract in Asia: An overview of research in congenital and age-related cataract with emphasis on Indian populations. In *Advances in Vision Research, Volume I*, pages 55–70. Springer, 2017.

[232] Wei-Jie Zhao and Yong-Bin Yan. Increasing susceptibility to oxidative stress by cataract-causing crystallin mutations. *International Journal of Biological Macromolecules*, 108:665–673, 2018.

[233] Yi-Bo Xi, Xiang-Jun Chen, Wei-Jie Zhao, and Yong-Bin Yan. Congenital cataract-causing mutation G129C in γC-crystallin promotes the accumulation of two distinct unfolding intermediates that form highly toxic aggregates. *Journal of Molecular Biology*, 427(17):2765–2781, 2015.

[234] Dietrich A Stephan, Elizabeth Gillanders, Deborah Vanderveen, Diana Freas-Lutz, Graeme Wistow, Andreas D Baxevanis, Christiane M Robbins, Ann Van Auken, Matthew I Quesenberry, Joan Bailey-Wilson, et al. Progressive juvenile-onset punctate cataracts caused by mutation of the γD-crystallin gene. *Proceedings of the National Academy of Sciences*, 96(3):1008–1012, 1999.

[235] Li-Yun Zhang, Bo Gong, Jian-Ping Tong, Dorothy Shu-Ping Fan, Sylvia Wai-Yee Chiang, Dinghua Lou, Dennis Shun-Chiu Lam, Gary Hin-Fai Yam, and Chi-Pui Pang. A novel γD-crystallin mutation causes mild changes in protein properties but leads to congenital coralliform cataract. *Molecular Vision*, 15:1521, 2009.

[236] Yi Zhai, Jinyu Li, Wangshu Yu, Sha Zhu, Yinhui Yu, Menghan Wu, Guizhen Sun, Xiaohua Gong, and Ke Yao. Targeted exome sequencing of congenital cataracts related genes: broadening the mutation spectrum and genotype–phenotype correlations in 27 chinese han families. *Scientific reports*, 7(1):1219, 2017.

[237] Jinwon Jung, In-Ja L Byeon, Yongting Wang, Jonathan King, and Angela M Gronenborn. The structure of the cataract-causing p23t mutant of human γd-crystallin exhibits distinctive local conformational and dynamic changes. *Biochemistry*, 48(12):2597–2609, 2009.

[238] P Evans, K Wyatt, GJ Wistow, OA Bateman, BA Wallace, and C Slingsby. The P23T cataract mutation causes loss of solubility of folded γD-crystallin. *Journal of Molecular Biology*, 343(2):435–444, 2004.

[239] E Nandrot, Christine Slingsby, A Basak, M Cherif-Chefchaouni, B Benazzouz, Y Hajaji, S Boutayeb, O Gribouval, L Arbogast, A Berraho, et al. Gamma-D crystallin gene (CRYGD) mutation causes autosomal dominant congenital cerulean cataracts. *Journal of Medical Genetics*, 40(4):262–267, 2003.

[240] Ajay Pande, Kalyan S Ghosh, Priya R Banerjee, and Jayanti Pande. Increase in surface hydrophobicity of the cataract-associated P23T mutant of human γD-crystallin is responsible for its dramatically lower, retrograde solubility. *Biochemistry*, 49(29):6122–6129, 2010.

[241] Fangling Ji, Leonardus MI Koharudin, Jinwon Jung, and Angela M Gronenborn. Crystal structure of the cataract-causing P23T γD-crystallin mutant. *Proteins: Structure, Function, and Bioinformatics*, 81(9):1493–1498, 2013.

[242] Priya R Banerjee, Shadakshara S Puttamadappa, Ajay Pande, Alexander Shekhtman, and Jayanti Pande. Increased hydrophobicity and decreased backbone flexibility explain the lower solubility of a cataract-linked mutant of γD-crystallin. *Journal of Molecular Biology*, 412(4):647–659, 2011.

[243] A Pande, J Zhang, A Shekhtman, and J Pande. A high-resolution NMR study of human gammaD crystallin and its cataract-linked P23T mutant: Small conformational changes in P23T explain its low and retrograde solubility. *Investigative Ophthalmology & Visual Science*, 49(13):4084–4084, 2008.

[244] Wenmin Sun, Xueshan Xiao, Shiqiang Li, Xiangming Guo, and Qingjiong Zhang. Mutation analysis of 12 genes in Chinese families with congenital cataracts. *Molecular Vision*, 17:2197, 2011.

[245] Stanislav Kmoch, Jirí Brynda, Befekadu Asfaw, Karel Bezouška, Petr Novák, Pavlína Řezáčová, Lenka Ondrová, Martin Filipec, Juraj Sedláček, and Milan Elleder. Link between a novel human γD-crystallin allele and a unique cataract phenotype explained by protein crystallography. *Human Molecular Genetics*, 9(12):1779–1786, 2000.

[246] Deborah K VanderVeen, Caroline Andrews, Bharti R Nihalani, and Elizabeth C Engle. Crystalline cataract caused by a heterozygous missense mutation in γD-crystallin (crygd). *Molecular Vision*, 17:3333, 2011.

[247] Jingzhi Gu, Yanhua Qi, Li Wang, Jin Wang, Lisong Shi, Hui Lin, Xiang Li, Hong Su, and Shangzhi Huang. A new congenital nuclear cataract caused by a missense mutation in the gammad-crystallin gene (crygd) in a Chinese family. *Molecular Vision*, 11(9):971, 2005.

[248] Li Wang, Xueli Chen, Yi Lu, Jihong Wu, Boqi Yang, and Xinghuai Sun. A novel mutation in γD-crystallin associated with autosomal dominant congenital cataract in a Chinese family. *Molecular Vision*, 17:804, 2011.

[249] Eugene Serebryany, Jaie C Woodard, Bharat V Adkar, Mohammed Shabab, Jonathan A King, and Eugene I Shakhnovich. An internal disulfide locks a misfolded aggregation-prone intermediate in cataract-linked mutants of human γD-crystallin. *Journal of Biological Chemistry*, pages jbc–M116, 2016.

[250] Sathiyavedu T Santhiya, Ganesan Senthil Kumar, Pridhvi Sudhakar, Navnit Gupta, Norman Klopp, Thomas Illig, Torben Söker, Marco Groth, Matthias Platzer, Puthiya M Gopinath, et al. Molecular analysis of cataract families in india: new mutations in the crybb2 and gja3 genes and rare polymorphisms. *Molecular Vision*, 16:1837, 2010.

[251] Feifeng Li, Shuzhen Wang, Chang Gao, Shiguo Liu, Baojian Zhao, Meng Zhang, Shangzhi Huang, Siquan Zhu, and Xu Ma. Mutation G61C in the CRYGD gene causing autosomal dominant congenital coralliform cataracts. *Molecular Vision*, 14:378, 2008.

[252] Mascarenhas Roshan, Pai H Vijaya, G Rao Lavanya, Prasada K Shama, ST Santhiya, Jochen Graw, PM Gopinath, and K Satyamoorthy. A novel human CRYGD mutation in a juvenile autosomal dominant cataract. *Molecular Vision*, 16:887, 2010.

[253] A Pande, PR Banerjee, J Patrosz, and J Pande. The cataract-associated mutation Glu107 to Ala in human gamma-D crystallin has no effect on protein structure, solubility and light scattering in solution: How does it cause cataract? *Investigative Ophthalmology & Visual Science*, 50(13):1640–1640, 2009.

[254] Priya R Banerjee, Ajay Pande, George Thurston, and Jayanti Pande. Thermodynamic studies on the cataract-associated mutant, E107A, of human gamma-D crystallin: Molecular basis for cataract formation. *Biophysical Journal*, 98(3):44a, 2010.

[255] Brian P Danysh, Tapan P Patel, Kirk J Czymmek, David A Edwards, Liyun Wang, Jayanti Pande, and Melinda K Duncan. Characterizing molecular diffusion in the lens capsule. *Matrix Biology*, 29(3):228–236, 2010.

[256] Venkata Pulla Rao Vendra and Dorairajan Balasubramanian. Structural and aggregation behavior of the human γD-crystallin mutant e107a, associated with congenital nuclear cataract. *Molecular Vision*, 16:2822, 2010.

[257] Priya R Banerjee, Ajay Pande, Julita Patrosz, George M Thurston, and Jayanti Pande. Cataract-associated mutant E107A of human γD-crystallin shows increased attraction to α-crystallin and enhanced light scattering. *Proceedings of the National Academy of Sciences*, 108(2):574–579, 2011.

[258] Carolyn N Kingsley, William D Brubaker, Stefan Markovic, Anne Diehl, Amanda J Brindley, Hartmut Oschkinat, and Rachel W Martin. Preferential and specific binding of human αb-crystallin to a cataract-related variant of γs-crystallin. *Structure*, 21(12):2221–2227, 2013.

[259] Jun Jiang, Kory J Golchert, Carolyn N Kingsley, William D Brubaker, Rachel W Martin, and Shaul Mukamel. Exploring the aggregation propensity of γS-crystallin protein variants using two-dimensional spectroscopic tools. *The Journal of Physical Chemistry B*, 117(46):14294–14301, 2013.

[260] Ajay Pande and Jayanti Pande. Interaction of human gammas-crystallin and its cataract-associated G18V mutant with alpha-crystallins. *Investigative Ophthalmology & Visual Science*, 56(7):5593–5593, 2015.

[261] Kyle W Roskamp, David M Montelongo, Chelsea D Anorma, Diana N Bandak, Janine A Chua, Kurtis T Malecha, and Rachel W Martin. Multiple aggregation pathways in human γs-crystallin and its aggregation-prone g18v variant. *Investigative ophthalmology & visual science*, 58(4):2397–2405, 2017.

[262] Vanita Vanita, Jai Rup Singh, Daljit Singh, Raymonda Varon, and Karl Sperling. Novel mutation in the γ-s crystallin gene causing autosomal dominant cataract. *Molecular Vision*, 15:476, 2009.

[263] Zhenfei Yang, Qian Li, Siquan Zhu, and Xu Ma. A G57W mutation of CRYGS associated with autosomal dominant pulverulent cataracts in a Chinese family. *Ophthalmic Genetics*, 36(3):281–283, 2015.

[264] Khandekar Jishan Bari, Shrikant Sharma, and Kandala VR Chary. Sequence specific ^{1}H, ^{13}C and ^{15}N resonance assignments of a cataract-related variant G57W of human γS-crystallin. *Biomolecular NMR assignments*, 12(1):51–55, 2018.

[265] Khandekar Jishan Bari, Shrikant Sharma, and Kandala VR Chary. Structural and functional characterization of a missense mutant of human γS-crystallin associated with dominant infantile cataracts. *Biochemical and Biophysical Research Communications*, 2018.

[266] Tianxiao Zhang, Lulu Yan, Yunji Leng, Chen Chen, Liwei Ma, Qian Wang, Jinsong Zhang, and Lihua Cao. A novel missense mutation of CRYGS underlies congenital cataract in a Chinese family. *Gene*, 675:9–14, 2018.

[267] Sha Zhu, Xi-Bo Xi, Tian-Li Duan, Yi Zhai, Jinyu Li, Yong-Bin Yan, and Ke Yao. The cataract-causing mutation G75V promotes γS-crystallin aggregation by modifying and destabilizing the native structure. *International Journal of Biological Macromolecules*, 2018.

[268] Genetic and allelic heterogeneity of cryg mutations in eight distinct forms of dominant cataract in the mouse. *Investigative Ophthalmology & Visual Science*, 45(4):1202–1213, 2004.

[269] Haiquan Liu, Xin Du, Meng Wang, Qingling Huang, Linlin Ding, Hayes W McDonald, John R Yates, Bruce Beutler, Joseph Horwitz, and Xiaohua Gong. Crystallin γB-I4F mutant protein binds to α-crystallin and affects lens transparency. *Journal of Biological Chemistry*, 2005.

[270] Lin Li, Bo Chang, Catherine Cheng, Da Chang, Norman L Hawes, Chun-hong Xia, and Xiaohua Gong. Dense nuclear cataract caused by the γB-crystallin S11R point mutation. *Investigative Ophthalmology & Visual Science*, 49(1):304–309, 2008.

[271] Jochen Graw, Jana Löster, Dian Soewarto, Helmut Fuchs, André Reis, Eckhard Wolf, Rudi Balling, and Martin Angelis. V76D mutation in a conserved γD-crystallin region leads to dominant cataracts in mice. *Mammalian Genome*, 13(8):452–455, 2002.

[272] Kate L Moreau and Jonathan A King. Cataract-causing defect of a mutant γ-crystallin proceeds through an aggregation pathway which bypasses recognition by the α-crystallin chaperone. *PloS One*, 7(5):e37256, 2012.

[273] Kate L Drahos and Jonathan King. Hydrophobic core mutations associated with cataract development in mice destabilize human γD-crystallin. *Journal of Biological Chemistry*, pages jbc–M109, 2009.

[274] Matthew J Whitley, Zhaoyong Xi, Jonathan C Bartko, Malene Ringkjøbing Jensen, Martin Blackledge, and Angela M Gronenborn. A combined NMR and SAXS analysis of the partially folded cataract-associated V75D γD-crystallin. *Biophysical Journal*, 112(6):1135–1146, 2017.

[275] Zhenzhen Liu, Allen Taylor, Yizhi Liu, Mingxing Wu, Xiaohua Gong, and Fu Shang. Enhancement of ubiquitin conjugation activity reduces intracellular aggregation of V76D mutant γD-crystallin. *Investigative Ophthalmology & Visual Science*, 53(10):6655–6665, 2012.

[276] Bryon Mahler, Kiran Doddapaneni, Ian Kleckner, Chunhua Yuan, Graeme Wistow, and Zhengrong Wu. Characterization of a transient unfolding intermediate in a core mutant of γS-crystallin. *Journal of Molecular Biology*, 405(3):840–850, 2011.

[277] Soojin Lee, Bryon Mahler, Jodie Toward, Blake Jones, Keith Wyatt, Lijin Dong, Graeme Wistow, and Zhengrong Wu. A single destabilizing mutation (F9S) promotes concerted unfolding of an entire globular domain in γS-crystallin. *Journal of Molecular Biology*, 399(2):320–330, 2010.

[278] AA Zamyatnin. Protein volume in solution. *Progress in Biophysics and Molecular Biology*, 24:107–123, 1972.

[279] Walfrido Antuch, Peter Güntert, and Kurt Wüthrich. Ancestral βγ-crystallin precursor structure in a yeast killer toxin. *Nature Structural and Molecular Biology*, 3(8):662, 1996.

[280] Hubert Mayerhofer, Gabriele Schramm, Georgios N Hatzopoulos, Christoph Mueller-Dieckmann, Helmut Haas, and Jochen Mueller-Dieckmann. Cloning, expression, purification, crystallization and preliminary X-ray crystallographic analysis of interleukin-4-inducing principle from *Schistosoma mansoni* eggs (ipse/alpha-1). *Acta Crystallographica Section F*, 65(6):594–596, 2009.

[281] Ayako Ohno, Shin-ichi Tate, Sailaja S Seeram, Kazumi Hiraga, Mark B Swindells, Kohei Oda, and Masatsune Kainosho. NMR structure of the *Streptomyces* metalloproteinase inhibitor, SMPI, isolated from *Streptomyces nigrescens* TK-23: another example of an ancestral $\beta\gamma$-crystallin precursor structure. *Journal of Molecular Biology*, 282(2):421–433, 1998.

[282] Atul K Srivastava and Kandala VR Chary. Conformational heterogeneity and dynamics in a $\beta\gamma$-crystallin from *Hahella chejuensis*. *Biophysical Chemistry*, 157(1-3):7–15, 2011.

[283] V Rajanikanth, Shanti Swaroop Srivastava, Aditya K Singh, M Rajyalakshmi, Kousik Chandra, Penmatsa Aravind, Rajan Sankaranarayanan, and Yogendra Sharma. Aggregation-prone near-native intermediate formation during unfolding of a structurally similar nonlenticular $\beta\gamma$-crystallin domain. *Biochemistry*, 51(43):8502–8513, 2012.

[284] Eila S Cedergren-Zeppezauer, Nalin CW Goonesekere, Michael D Rozycki, James C Myslik, Zbigniew Dauter, Uno Lindberg, and Clarence E Schutt. Crystallization and structure determination of bovine profilin at $2 \cdot 0$ Å resolution. *Journal of Molecular Biology*, 240(5):459–475, 1994.

[285] Penmatsa Aravind, Graeme Wistow, Yogendra Sharma, and Rajan Sankaranarayanan. Exploring the limits of sequence and structure in a variant $\beta\gamma$-crystallin domain of the protein Absent in Melanoma-1 (AIM1). *Journal of Molecular Biology*, 381(3):509–518, 2008.

Appendix A

1: Supplementary material for Introduction.

Table A.1: Cataractous γ-crystallin substitution point mutants

Species	**Mutation**	**Research**
Homo sapiens	γC-T5P	[227, 228, 229, 230]
Homo sapiens	γC-R48H	[231, 232]
Homo sapiens	γC-G129C	[232, 233]
Homo sapiens	γC-R168W	[94, 231, 232]
Homo sapiens	γD-R14C	[232, 234]
Homo sapiens	γD-R14S	[235, 236]
Homo sapiens	γD-P24T	[231, 200, 237, 238, 239, 162, 240, 241, 242, 243, 236]
Homo sapiens	γD-A36P	[244, 200]
Homo sapiens	γD-R37S	[245, 246, 247]
Homo sapiens	γD-R37P	[248]
Homo sapiens	γD-W43R	[166, 249, 169]
Homo sapiens	γD-M44V	[250]
Homo sapiens	γD-R58H	[84, 232]
Homo sapiens	γD-G61C	[201, 251, 232]
Homo sapiens	γD-R77S	[231, 200, 252, 96]
Homo sapiens	γD-E107A	[253, 254, 255, 256, 257]
Homo sapiens	γS-G18V	[93, 124, 125, 85, 258, 259, 260, 134, 261]
Homo sapiens	γS-G18D	[236]
Homo sapiens	γS-D26G	[163, 244]
Homo sapiens	γS-S39C	[94, 231, 95]
Homo sapiens	γS-V42M	[165, 164, 262, 231]
Homo sapiens	γS-G57W	[263, 202, 264]
Homo sapiens	γS-Y67N	[265, 266]
Homo sapiens	γS-G75V	[267, 236]
Mus musculus	γA-W43R	[268]
Mus musculus	γA-D74G	[268]
Mus musculus	γB-I4F	[269]
Mus musculus	γB-S11R	[270]
Mus musculus	γD-L45P	[268]
Mus musculus	γD-V76D	[268, 271, 272, 273, 274, 275]
Mus musculus	γD-I90F	[268, 272, 273]
Mus musculus	γE-L45P	[268]
Mus musculus	γE-V126M	[268]
Mus musculus	γF-V38E	[268]
Mus musculus	γS-F9S	[276, 277]

Appendix B

2: Supplementary material for Divalent cations and the divergence of $\beta\gamma$-crystallin function

Table B.1: Mean amino acid composition of cation-binding $\beta\gamma$-, lens γA-D, and lens γS-crystallins

	γA-D	**γS**	$\beta\gamma$
A	2.0 ± 0.7	4.1 ± 0.9	5.3 ± 3.0
C	4.3 ± 0.9	3.7 ± 0.4	0.5 ± 0.9
D	6.8 ± 0.9	5.7 ± 0.6	7.1 ± 2.0
E	6.0 ± 0.8	7.8 ± 0.7	4.4 ± 2.7
F	3.6 ± 1.1	5.4 ± 0.5	4.5 ± 2.3
G	7.6 ± 0.6	8.1 ± 0.7	10.2 ± 2.7
H	3.2 ± 1.0	3.2 ± 0.8	0.7 ± 0.6
I	3.6 ± 0.9	4.7 ± 0.9	6.2 ± 2.3
K	1.4 ± 0.6	4.9 ± 0.6	5.0 ± 2.0
L	8.9 ± 1.3	5.2 ± 0.5	6.2 ± 2.3
M	3.4 ± 0.8	3.3 ± 0.5	0.6 ± 0.9
N	3.1 ± 0.7	3.3 ± 0.4	8.3 ± 2.5
P	4.0 ± 0.6	4.1 ± 0.5	3.8 ± 2.2
Q	5.4 ± 1.0	4.9 ± 0.5	3.3 ± 1.4
R	11.5 ± 0.9	7.5 ± 0.9	2.7 ± 2.2
S	8.0 ± 0.9	6.6 ± 0.9	9.8 ± 2.7
T	2.1 ± 0.8	3.3 ± 0.6	6.2 ± 4.6
V	3.8 ± 0.8	4.7 ± 1.0	8.8 ± 2.7
W	2.3 ± 0.2	2.2 ± 0.1	1.8 ± 1.5
Y	8.8 ± 1.0	7.2 ± 0.6	4.7 ± 2.1

The mean amino acid composition of lens γA-D, γS, and cation-binding $\beta\gamma$-crystallins with ± standard deviation. The variability across all amino acids is similar for the lens γA-D and γS. Variability is higher for the cation-binding $\beta\gamma$-crystallins.

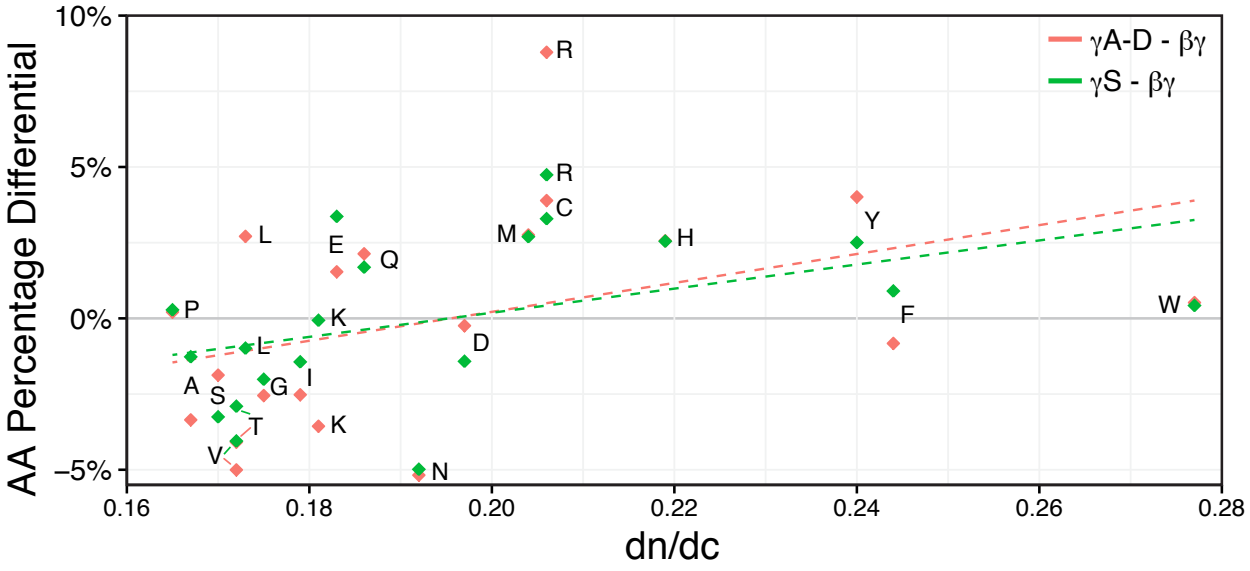

Figure A.1: Amino acid composition difference between lens γ-crystallins and cation-binding $\beta\gamma$-crystallins. The difference in the mean amino acid composition of lens γA-D (red) and γS-crystallins (green) from cation-binding $\beta\gamma$-crystallins is plotted against the refractive index increment (dn/dc) for each amino acid [29]. Regression lines were plotted as a visual guide. Both groups of lens γ-crystallins are more enriched in highly refractive amino acids than the cation-binding $\beta\gamma$-crystallins.

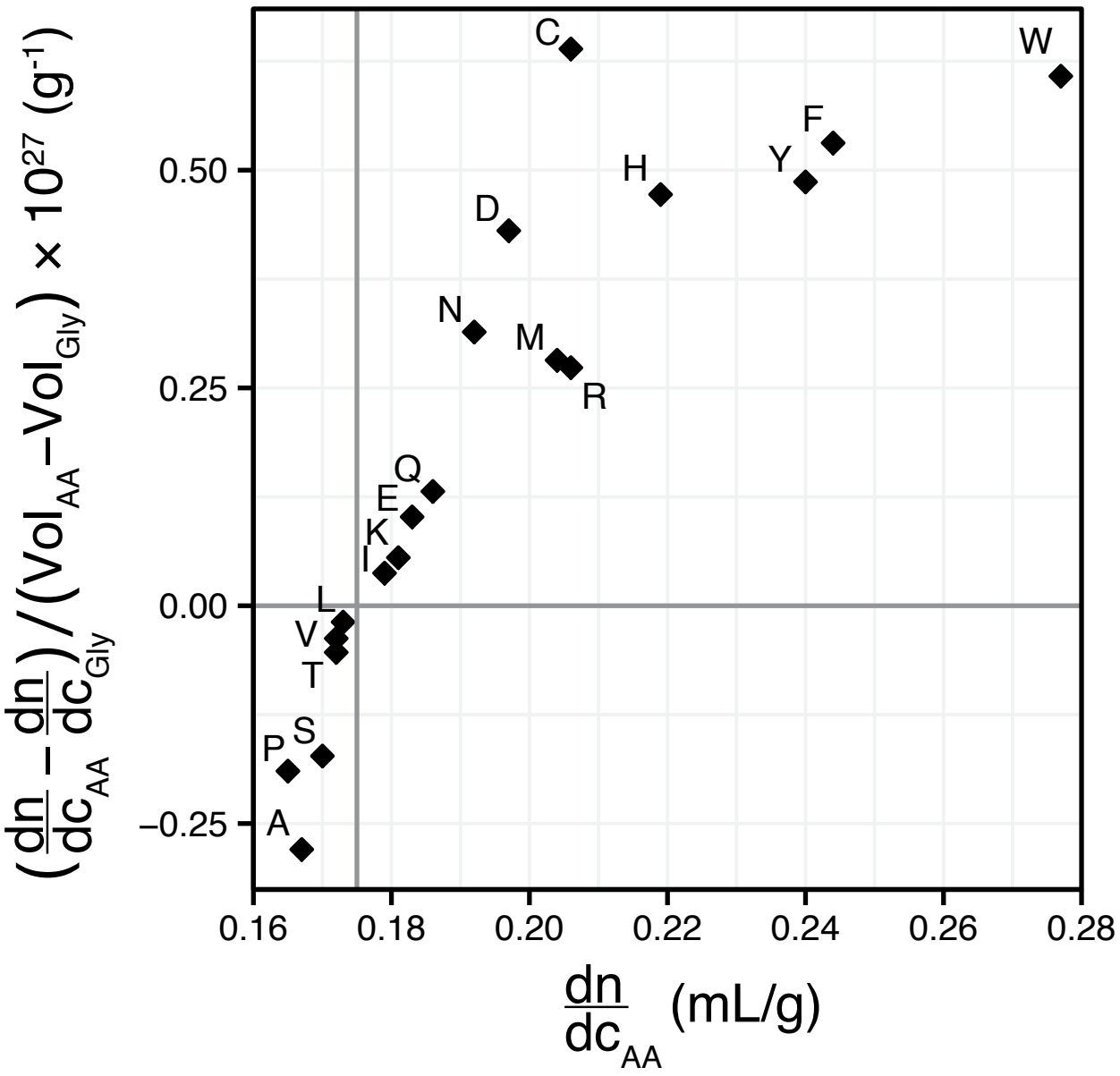

Figure A.2: The dn/dc of each amino acid was scaled by its volume after subtracting the corresponding value for glycine to account for the contribution of the backbone atoms. Cysteine is the most refractive amino acid for the size of its sidechain, whereas alanine is the least refractive. The amino acid dn/dc values and volumes were taken from Zhou *et al.* and Zamyatnin *et al.*, respectively [29, 278].

Table B.2: Comparison of conserved lens γ-crystallin cysteine positions to cation-binding $\beta\gamma$-crystallins

Lens γA-NTD	$\mathbf{C}_{15}$	$\mathbf{C}_{18}$	S	$\mathbf{C}_{22}$	N	$\mathbf{C}_{32}$	I	$\mathbf{C}_{41}$	$\mathbf{C}_{78}$	R
Lens γB-NTD	$\mathbf{C}_{15}$	$\mathbf{C}_{18}$	S	$\mathbf{C}_{22}$	N	$\mathbf{C}_{32}$	I	$\mathbf{C}_{41}$	$\mathbf{C}_{78}$	R
Lens γC-NTD	$\mathbf{C}_{15}$	$\mathbf{C}_{18}$	S	$\mathbf{C}_{22}$	N	$\mathbf{C}_{32}$	I	$\mathbf{C}_{41}$	$\mathbf{C}_{78}$	$\mathbf{C}_{79}$
Lens γD-NTD	H	$\mathbf{C}_{18}$	S	H	N	$\mathbf{C}_{32}$	V	$\mathbf{C}_{41}$	$\mathbf{C}_{78}$	R
Lens γS-NTD	R	$\mathbf{C}_{23}$	$\mathbf{C}_{25}$	$\mathbf{C}_{27}$	N	$\mathbf{C}_{37}$	I	T	$\mathbf{C}_{83}$	R
Lens γA-CTD	V	L	E	$\mathbf{C}_{108}$	$\mathbf{C}_{110}$	I	L	$\mathbf{C}_{129}$	L	R
Lens γB-CTD	M	I	D	$\mathbf{C}_{108}$	S	I	L	S	L	R
Lens γC-CTD	M	L	E	$\mathbf{C}_{108}$	$\mathbf{C}_{110}$	V	L	$\mathbf{C}_{129}$	L	R
Lens γD-CTD	M	F	E	$\mathbf{C}_{108}$	S	I	L	S	L	R
Lens γS-CTD	M	T	E	$\mathbf{C}_{115}$	S	I	$\mathbf{C}_{130}$	A/V	F	R
Geodia cydonium $\beta\gamma$-CTD	E	L	N	N	R	V	A	Q	M	E
Ciona intestinalis $\beta\gamma$	K	L	P	V	D	V	I	T	V	K
Methanosarcina acetivorans $\beta\gamma$	S	A	S	Q	G	I	L	T	F	R
Clostridium beijerinckii $\beta\gamma$	S	L	P	N	T	M	V	W	V	K
Myxococcus xanthus $\beta\gamma$	Q	L	P	N	T	I	V	V	I	R
Flavobacterium johnsoniae $\beta\gamma$	S	L	I	D	N	V	L	Y	I	R
Physarum polycephalum $\beta\gamma$	S	V	G	V	D	V	V	T	I	I

Alignment of the consensus cysteine positions between the N-terminal (NTD) and C-terminal (CTD) domains of lens γ-crystallins and cation-binding $\beta\gamma$-crystallins. Only positions containing a cysteine in a lens γ-crystallin consensus sequence are shown for clarity. The sequence position for each cysteine is given as a subscript, where the γA-D crystallins are annotated using the sequence index of human γD-crystallin. The NTD of *Geodia cydonium* $\beta\gamma$-crystallin does not bind any cations, and is therefore excluded from the analysis.

The observed state of cysteine residues from $\beta\gamma$-crystallins that have 3D structures deposited in the PDB. The cysteines of cation-binding $\beta\gamma$-crystallins are found in disulfide bonds. The one cysteine from *P. polycephalum* participates in an intermolecular disulfide bond. Non-calcium-binding $\beta\gamma$-crystallins from bacteria (PDBID: 1WKT, PDBID: 4EL6, PDBID: 1BHU, PDBID: 2KP5) show disulfide bonding of all cysteine residues. The three mammalian $\beta\gamma$-crystallins contain cysteines that are not found in disulfide bonds.

Table B.3: Status of cysteine residues in solved structures of $\beta\gamma$-crystallins

PDBID	**Organism**	**Free Cys**	**Disulfide Cys**	**Cation Binding**
1HDF [76]	*Physarum polycephalum*	0	1	Yes
1NPS [70]	*Myxococcus xanthus*	0	0	Yes
2BV2 [47]	*Ciona intestinalis*	0	0	Yes
3HZB [68]	*Flavobacterium johnsoniae*	0	2	Yes
3HZ2 [68]	*Methanosarcina acetivorans*	0	0	Yes
5HT9	*Methanosarcina acetivorans*	0	0	Yes
3I9H [68]	*Clostridium beijerinckii*	0	0	Yes
4IAU [77]	*Geodia cydonium*	0	0	Yes
1WKT [279]	*Cyberlindnera mrakii*	0	10	No
4EL6 [280]	*Schistosoma mansoni*	0	6	No
1BHU [281]	*Streptomyces nigrescens*	0	4	No
2KP5 [282]	*Hahella chejuensis*	0	0	No
4FD9 [283]	*Mus musculus*	1	0	No
1PNE [284]	*Bos taurus*	3	0	No
3CW3 [285]	*Homo sapiens*	3	0	No

Table B.4: Cysteine solvent-accessible surface area in human γ-crystallins

	15	**18**	**20**	**22**	**32**	**41**	**78**	**79**	**108**	**110**	**123**	**129**	**153**
γ**A**	50%	11%		21%	0%	4%	0%		0%	14%		1%	
γ**B**		9%		16%	0%	6%	0%	8%	7%				
γ**C**				16%	0%	2%	2%	10%	9%			9%	13%
γ**D**		18%			0%	5%	0%		8%	26%			
	20	**23**	**25**	**27**	**37**	**46**	**83**	**84**	**115**	**117**	**130**	**136**	**159**
γ**S**		21%	77%	40%	2%		1%		1%		1%		

Solvent-accessible surface area for all cysteines from human γA, γB, γC, γD, and γS crystallin. The top indices refer to the position of each γA-D cysteine with respect to the human γD sequence. The bottom indices refer to the position of each γS cysteine with respect to the human γS sequence. The solvent-accessible surface area was determined using VADAR.

Table B.5: Cysteine conservation in terrestrial animal lens γA-D and γS-crystallins

	15	**18**		**22**	**32**	**41**	**78**	**79**	**108**	**110**		**129**
γA	80.0	98.0	S	82.0	100	96.0	100	R	100	98.0	L	84.0
γB	66.7	97.4	S	75.6	100	91.0	100	R	98.7	S	L	S/D
γC	62.9	82.3	S	87.1	100	96.8	100	61.3	100	67.7	L	85.5
γD	H	100	S	H	100	98.2	100	R	100	S	L	S
		23	**25**	**27**	**37**		**83**		**115**		**130**	
γS	R	74.2	72.6	96.8	100	T	100	R	100	S	95.2	A/V

Alignment and percent conservation for the conserved cysteines from terrestrial vertebrate γA-, γB-, γC-, γD-, and γS-crystallins. The top indices refer to the positions of the γA-D cysteines aligned to the human γD sequence. The bottom indices refer to the position of the γS cysteines in the human γS sequence. Typical lens γ-crystallin sequence are ∼170 residues long, which near identical numbers of residues in the N-terminal and C-terminal domains.

Table B.6: p-values for negative selection of cysteines in terrestrial vertebrate lens γA-D and γS-crystallins

	15	**18**	**22**	**32**	**41**	**78**	**79**	**108**	**110**	**129**
γA - FEL	0.15	0.63	0.41	0.03	0.16	*		< 0.01	0.04	0.30
γA - SLAC	1.00	1.00	0.62	0.18	0.33	*		< 0.01	0.10	1.00
γB - FEL	0.34	0.68	0.26	1.00	0.01	< 0.01		0.31		
γB - SLAC	0.94	0.02	0.28	< 0.01	0.65	0.03		< 0.01		
γC - FEL	0.17	0.34	< 0.01	< 0.01	0.69	< 0.01	0.06	*	0.12	0.30
γC - SLAC	1.00	1.00	0.09	0.03	1.00	< 0.01	0.05	*	0.40	1.00
γD - FEL		0.05		0.03	0.65	< 0.01		0.03		
γD - SLAC		0.20		0.20	1.00	0.04		0.19		

	23	**25**	**27**	**37**	**83**	**115**	**130**
γS - FEL	< 0.01	< 0.01	< 0.01	< 0.01	*	< 0.01	< 0.01
γS - SLAC	< 0.01	< 0.01	< 0.01	0.04	*	< 0.01	< 0.01

Negative selection was tested for at each of the conserved cysteine sites in terrestrial animal lens γA-D and γS-crystallins using SLAC and FEL. The p-values for each method at each site are tabulated above. Sites at which no synonymous or non-synonymous substitutions were observed are marked with an asterisk (*).

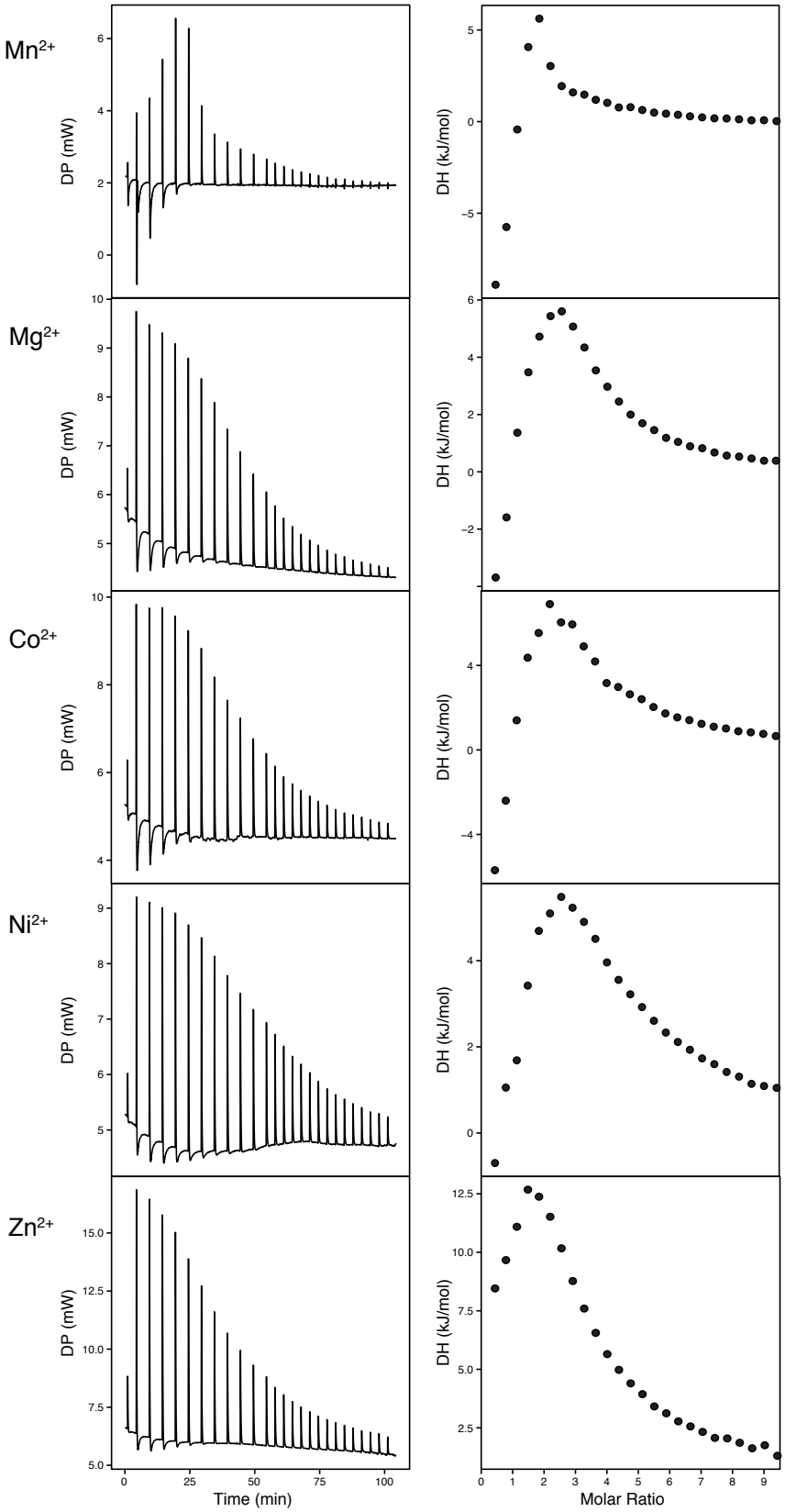

Figure A.3: Isothermal titration calorimetry measurements of 111 μM Ci-$\beta\gamma$ crystallin with 5 mM Mg^{2+}, Co^{2+}, Mn^{2+}, Ni^{2+}, and Zn^{2+}. Each of the tested divalent cations exhibited an endothermic isotherm.

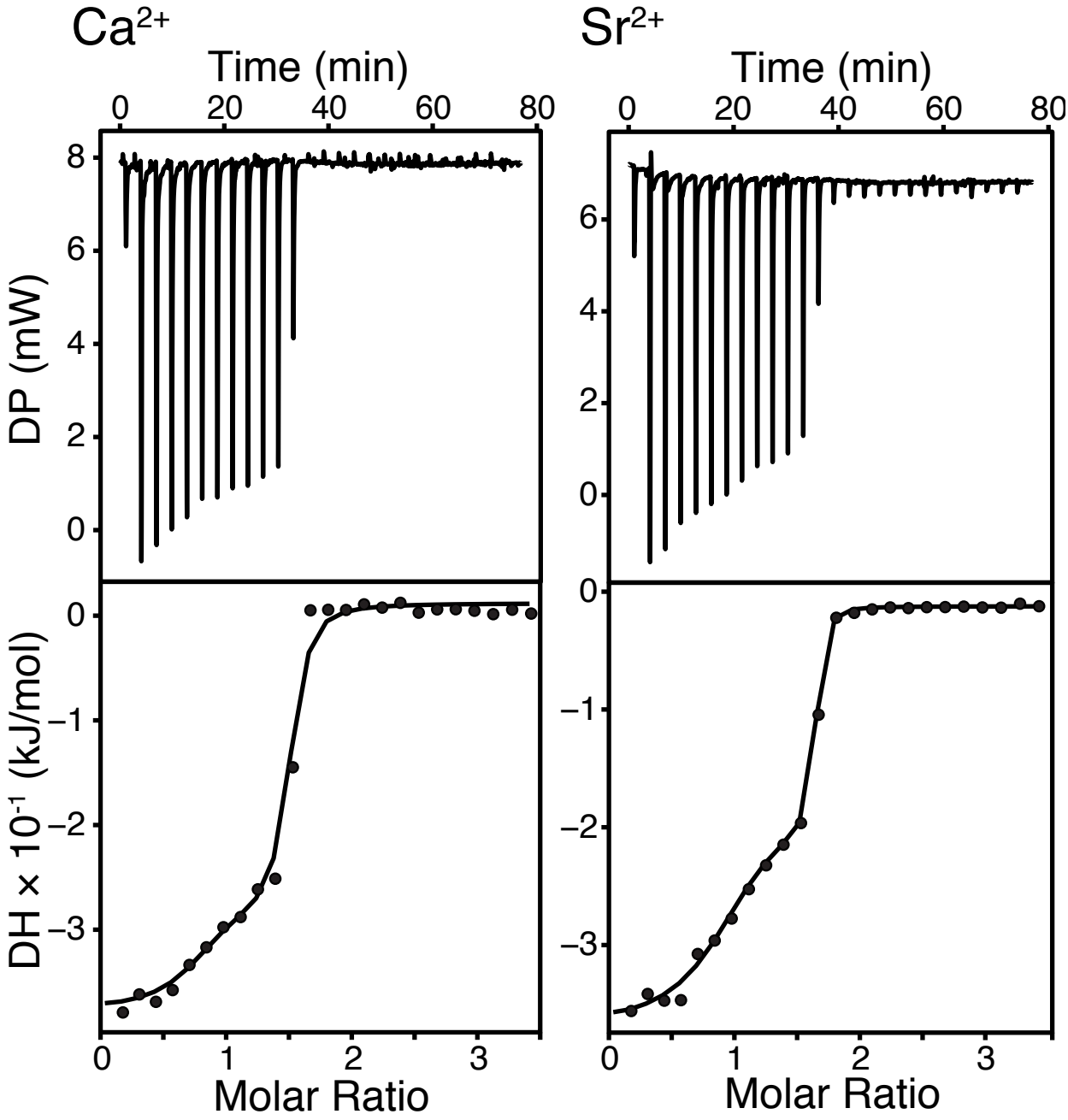

Figure A.4: Isothermal titration calorimetry measurements of 111 μM Ci-$\beta\gamma$ crystallin with 2 mM Ca^{2+} and Sr^{2+}. An exothermic isotherm was observed for both divalent cations, consistent with previous Ci-$\beta\gamma$ binding of Ca^{2+}, and of other $\beta\gamma$-crystallin to Ca^{2+}.

Table B.7: Cation binding distances and tetrahedral volumes of M-crystallin.

	Ca^{2+}	**Mg^{2+}**
Cation – E9 (Å)	2.49 ± 0.02	2.12 ± 0.19[1]
Cation – N76 (Å)	2.43 ± 0.01	2.25 ± 0.12
Cation – K34 (Å)	2.54 ± 0.01	2.40 ± 0.01
Cation – S36 (Å)	2.50 ± 0.01	2.28 ± 0.10
Site 1 ($Å^3$)	4.93 ± 0.07	3.87 ± 0.44
Cation – E49 (Å)	2.42 ± 0.02	2.03 ± 0.06
Cation – D33 (Å)	2.47 ± 0.01	2.11 ± 0.02
Cation – S77 (Å)	2.48 ± 0.02	2.09 ± 0.02
Cation – S79 (Å)	2.59 ± 0.03	2.04 ± 0.08
Site 2 ($Å^3$)	5.09 ± 0.10	2.86 ± 0.17

The distances and corresponding tetrahedral binding site volume from the X-ray crystal structures of M-crystallin bound to Mg^{2+} (PDBID: 5HT9) and Ca^{2+} (PDBID: 3HZ2). The standard deviation for each distance and volume were calculated from the variance between monomer crystal structures. Two monomers were present for the Ca^{2+}-bound M-crystallin while four monomers were present in the Mg^{2+}-bound M-crystallin.

[1]The E9 and H10 sidechains coordinate a highly solvated Ni^{2+} which may be responsible for the increased variance.

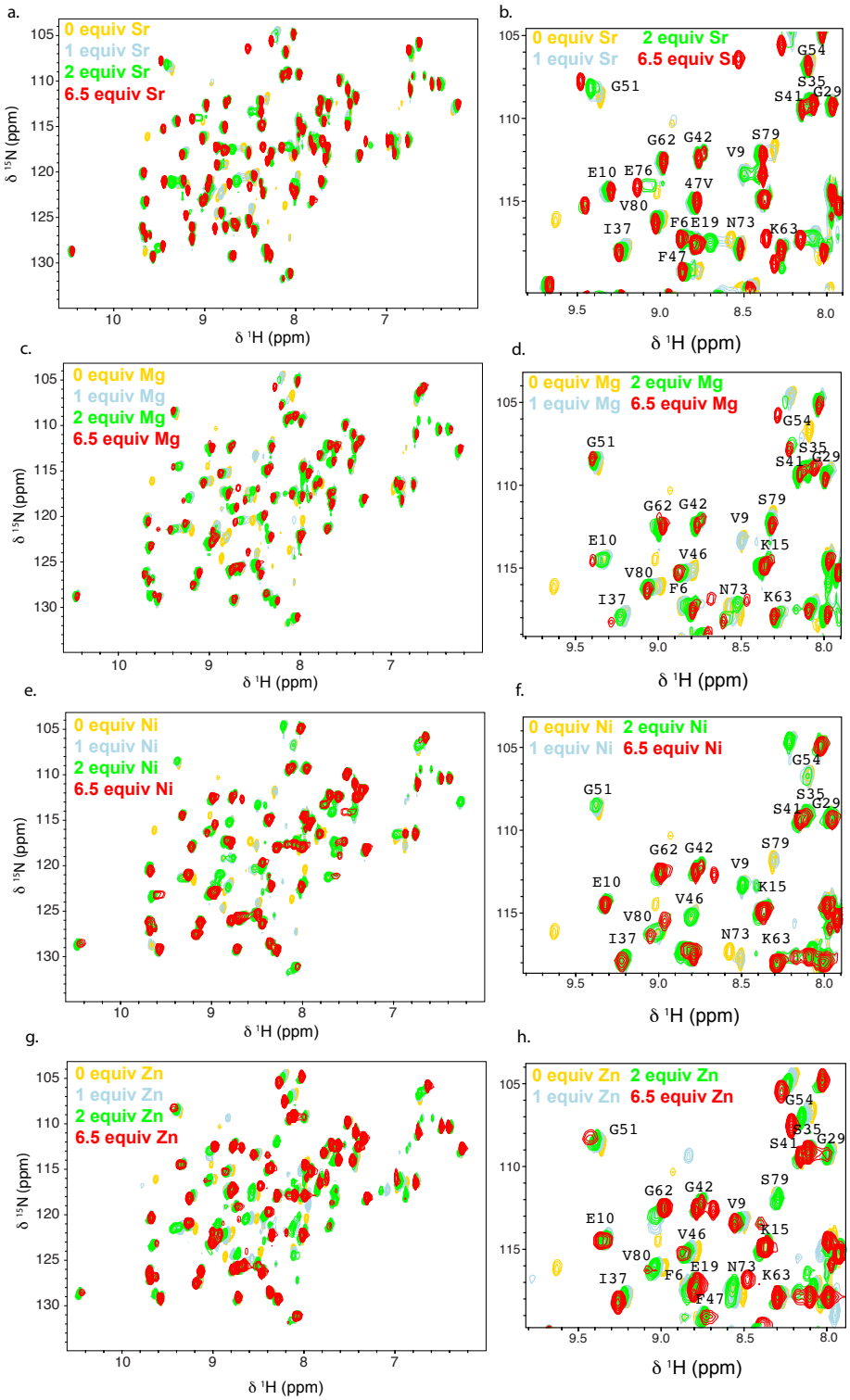

Figure A.5: Overlaid ^{15}N-^{1}H HSQC spectra of *Ci*-$\beta\gamma$ crystallin in with Sr^{2+} (a, b), Mg^{2+} (c, d), Ni^{2+} (e, f), and Zn^{2+} (g, h). Spectra of the entire relevant ^{1}H and ^{15}N regions are shown in (a), (c), (e), and (g) with representative subplots expanded in (b), (d), (f), and (h), respectively, to exemplify concentration-dependent changes in chemical shift. For each divalent cation, samples prepared with 0 (yellow), 1 (blue), 2 (green), and 6.5 (red) molar equivalents were measured.

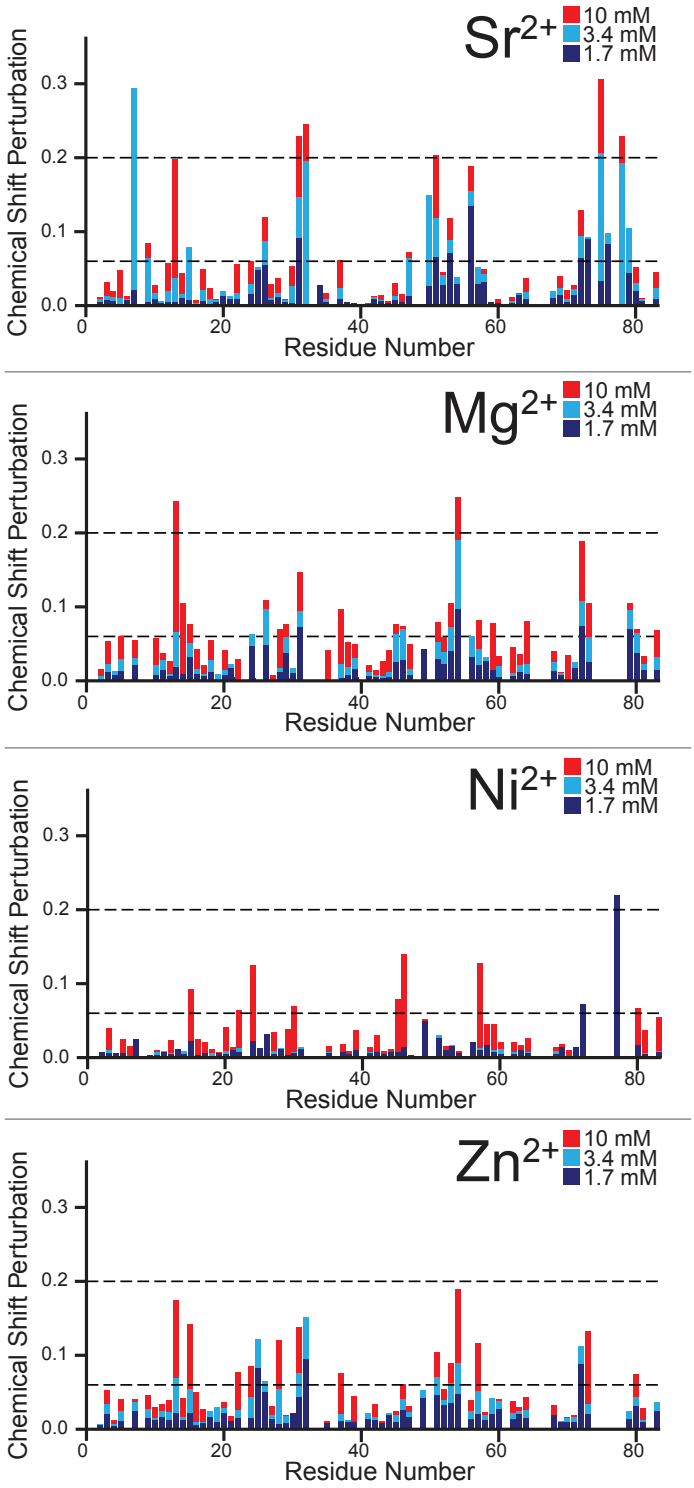

Figure A.6: ^{1}H-^{15}N-HSQC CSPs of *Ci*-$\beta\gamma$ from the titration of 1.7 (dark blue), 3.4 (cyan), and 10 (red) mM (1, 2, and 6.5 molar equivalents) Ca^{2+}, Sr^{2+}, Mg^{2+}, Ni^{2+}, and Zn^{2+}. The classification for strong (≥ 0.2) and moderate ($0.2 \leq, \geq 0.06$) CSPs is based on previously reported chemical shift changes of *Ci*-$\beta\gamma$ upon binding Ca^{2+}.

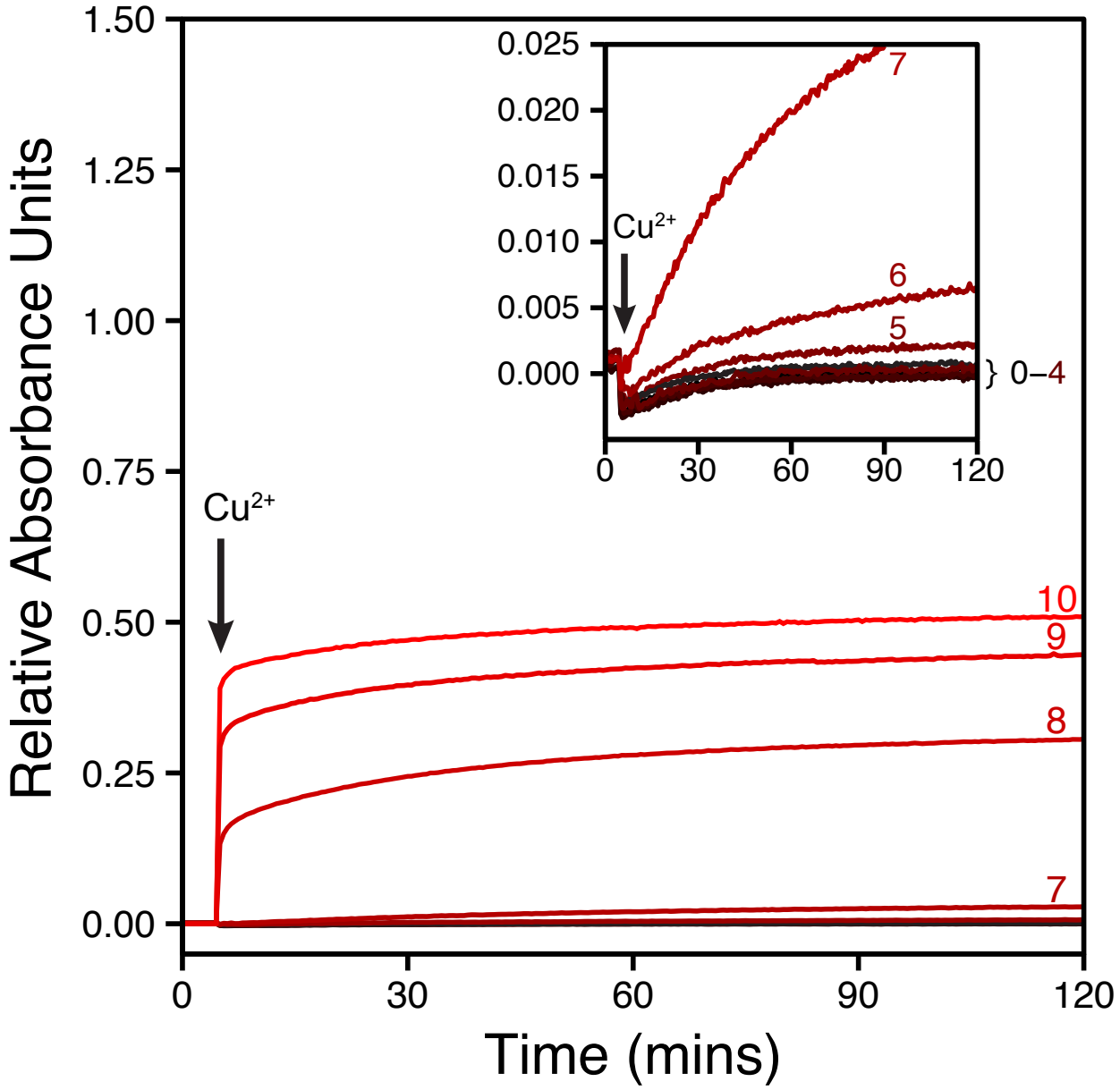

Figure A.7: Light scattering at 405 nm of *Ci*-$\beta\gamma$ in the presence of 0 to 10 equivalents of Cu^{2+}. Traces are labeled on the right with the number of molar equivalents of Cu^{2+} and colored from black (0 equivalents) to red (10 equivalents) to indicate the molar equivalents of Cu^{2+}. Appreciable levels of light scattering are observed at seven equivalents of Cu^{2+}

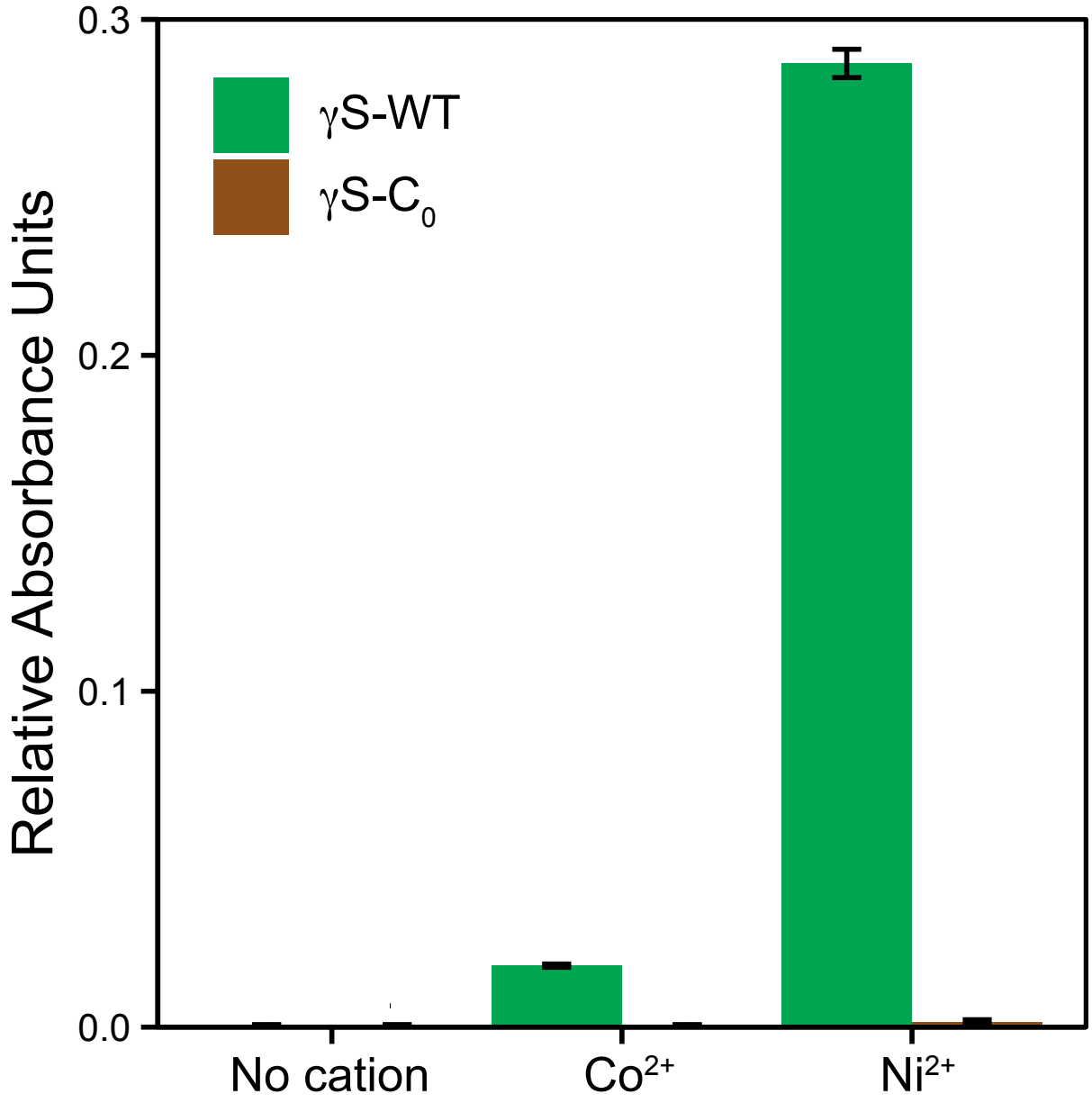

Figure A.8: Light scattering at 405 nm of monomeric HγS-WT (green) and γS-C_0 (brown). 10 equivalents of Co^{2+} or Ni^{2+} added to 50 μM protein and allowed to incubate for two hours at 42 °C. Error bars represent one standard deviation.

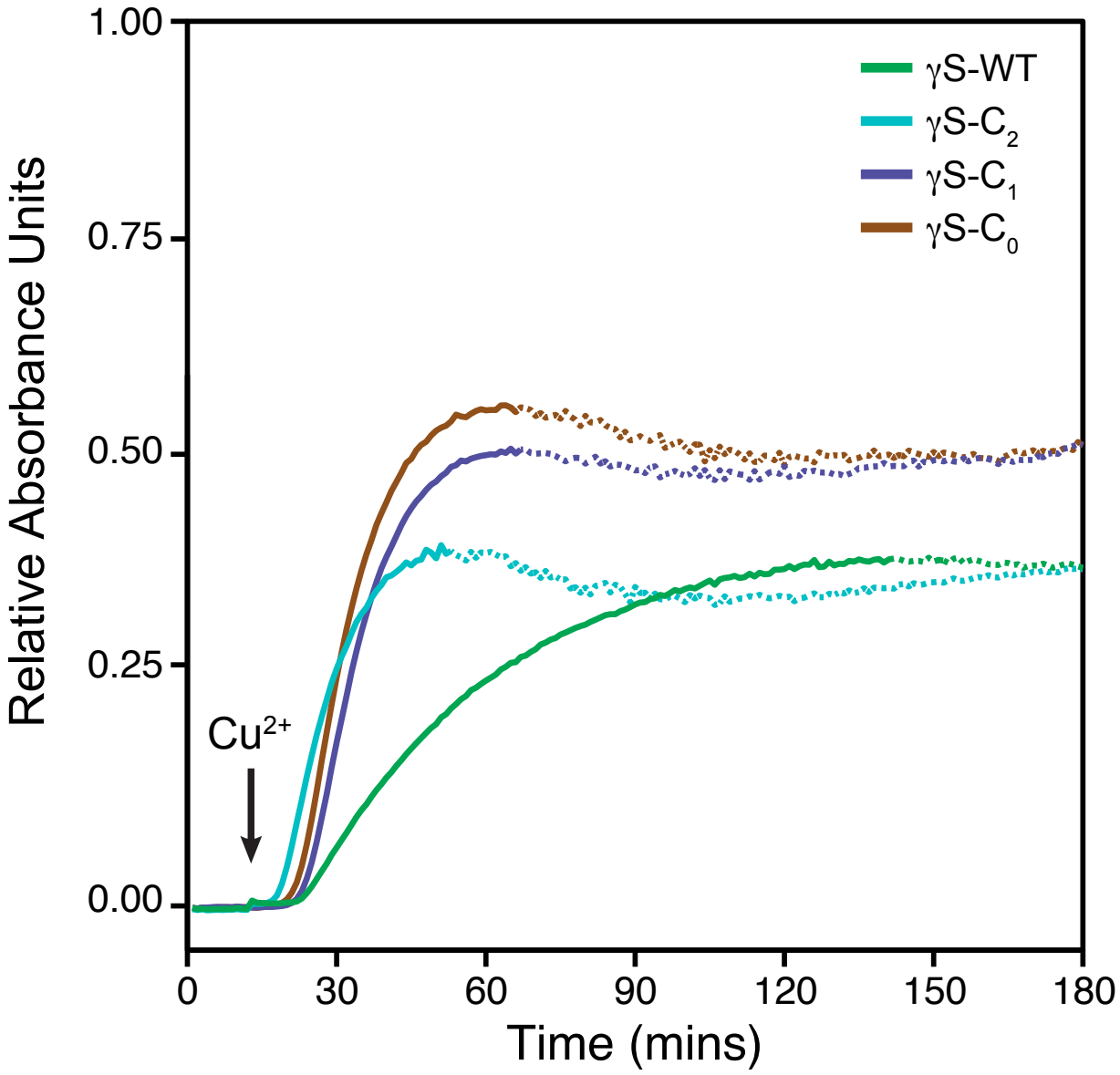

Figure A.9: Light scattering at 405 nm of monomeric forms of γS-WT (green), γS-C23S/C27S (cyan), γS-C23S/C25S/C27S (purple), and γS-C23S/C25S/C27S/C115S (brown). 2 equivalent of Cu^{2+} was added to a final concentration of 50 μM protein and allowed to incubate for three hours at 30 °C. The point at which protein precipitation is estimated to occur is denoted by a change from a solid line to a dashed line in each trace. Error bars represent one standard deviation.

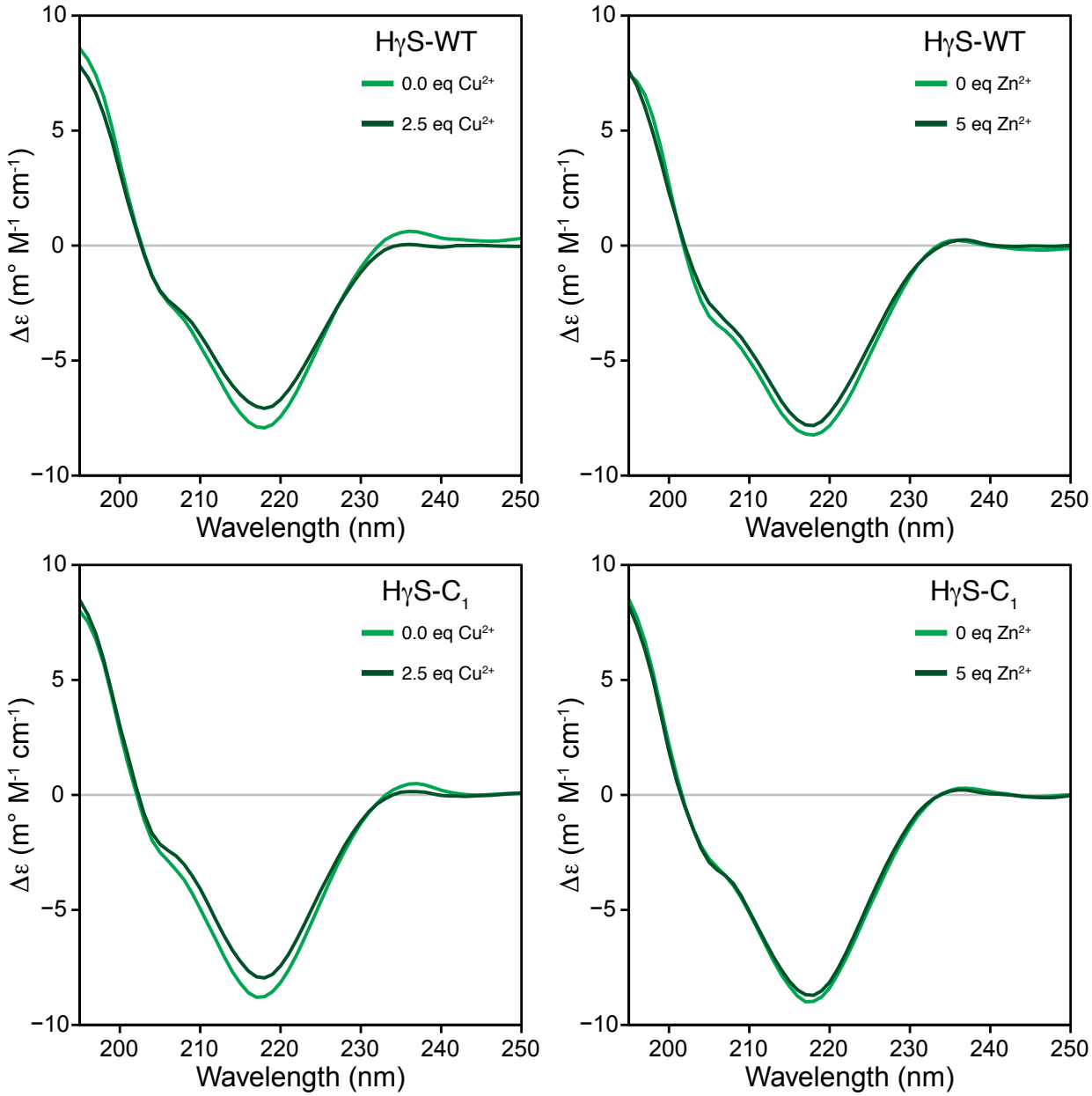

Figure A.10: Far-UV circular dichroism spectra of monomeric HγS and HγS-C_1 with Cu^{2+} or Zn^{2+}. The line shape following the addition of divalent cation in both cases remains unchanged.

Table B.8: Cu^{2+}-induced post-translational modifications of γS-WT and γS-C_0

Protein	**Start**	**End**	**Modification**	**Modified Residues**
γS-WT	20	36	m+32	C23 and/or C25
γS-WT	21	36	m+32	C23 and/or C25
γS-WT	102	125	m+16	C115
γS-C_0	42	72	m+16	M59
γS-C_0	102	125	m+16	M124

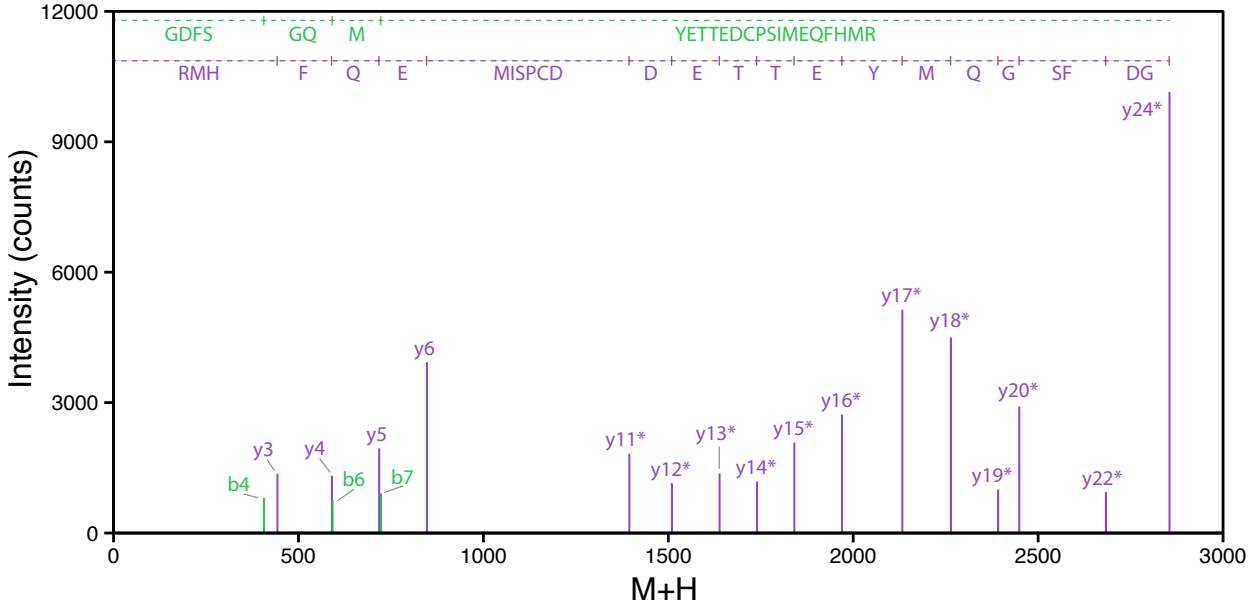

Figure A.11: Observed secondary ion fragmentation for the GDFSGQMYETTEDCPSIMEQFHMR peptide derived from γS-WT. The b (green) and y (purple) ions containing an m+16 mass difference are denoted with an asterisk.

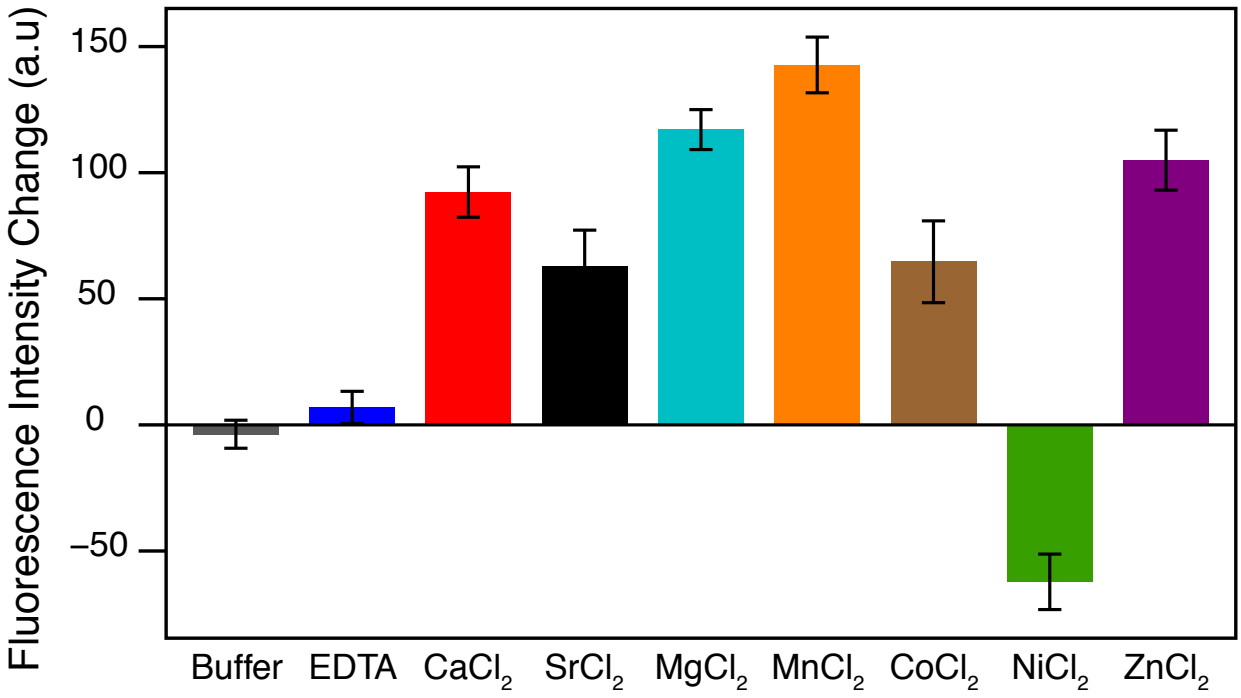

Figure A.12: Fluorescence intensity changes following the addition of divalent cations to apo-*Ci*-$\beta\gamma$. The mean difference in fluorescence intensity were measured in triplicate using the maximum intensity value. Error bars represent one standard deviation.

Appendix C

3: Supplementary material for Copper-induced aggregation of human γS-crystallin involves multiple mechanisms

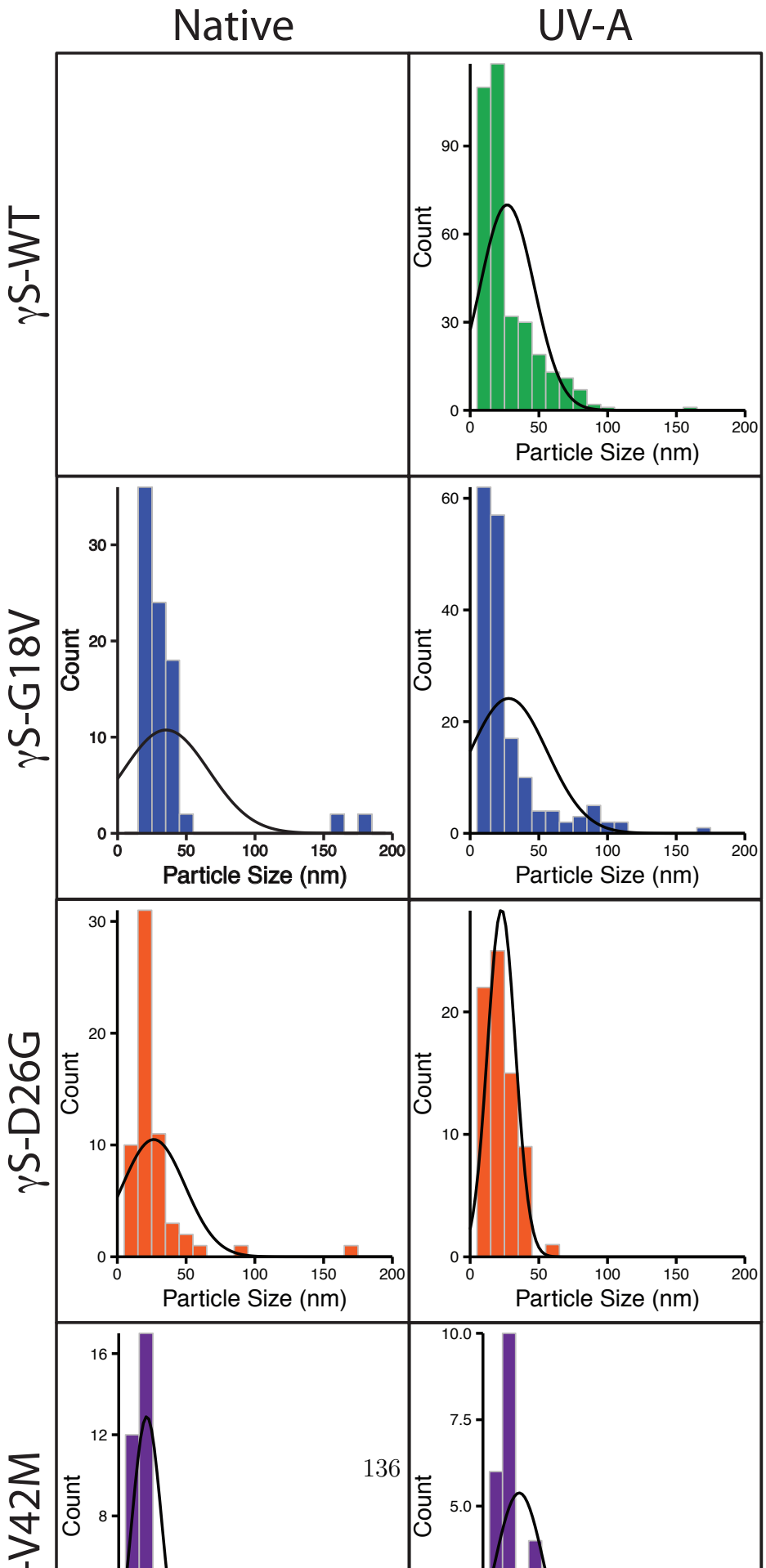
Native
UV-A
γS-WT
γS-G18V
γS-D26G
γS-V42M
Count
Particle Size (nm)
0
50
100
150
200
10
20
30
40
60
90
8
12
16
5.0
7.5
10.0

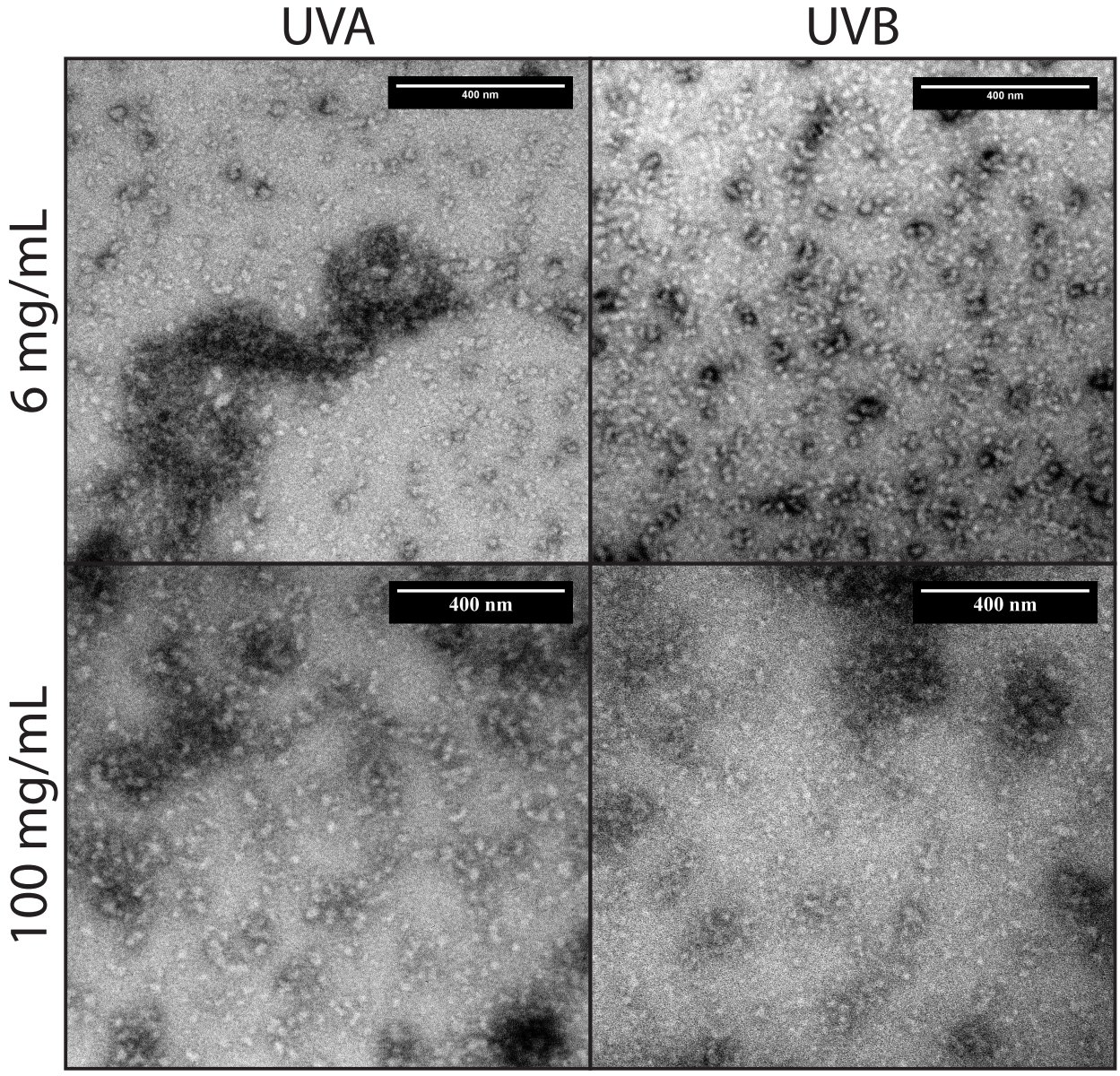

Figure A.2: Irradiation of γS-WT from UVA (1.6 kJ/cm^2) and UVB (104.4 J/cm^2) produces aggregates with similar morphology independent of sample concentration during irradiation.

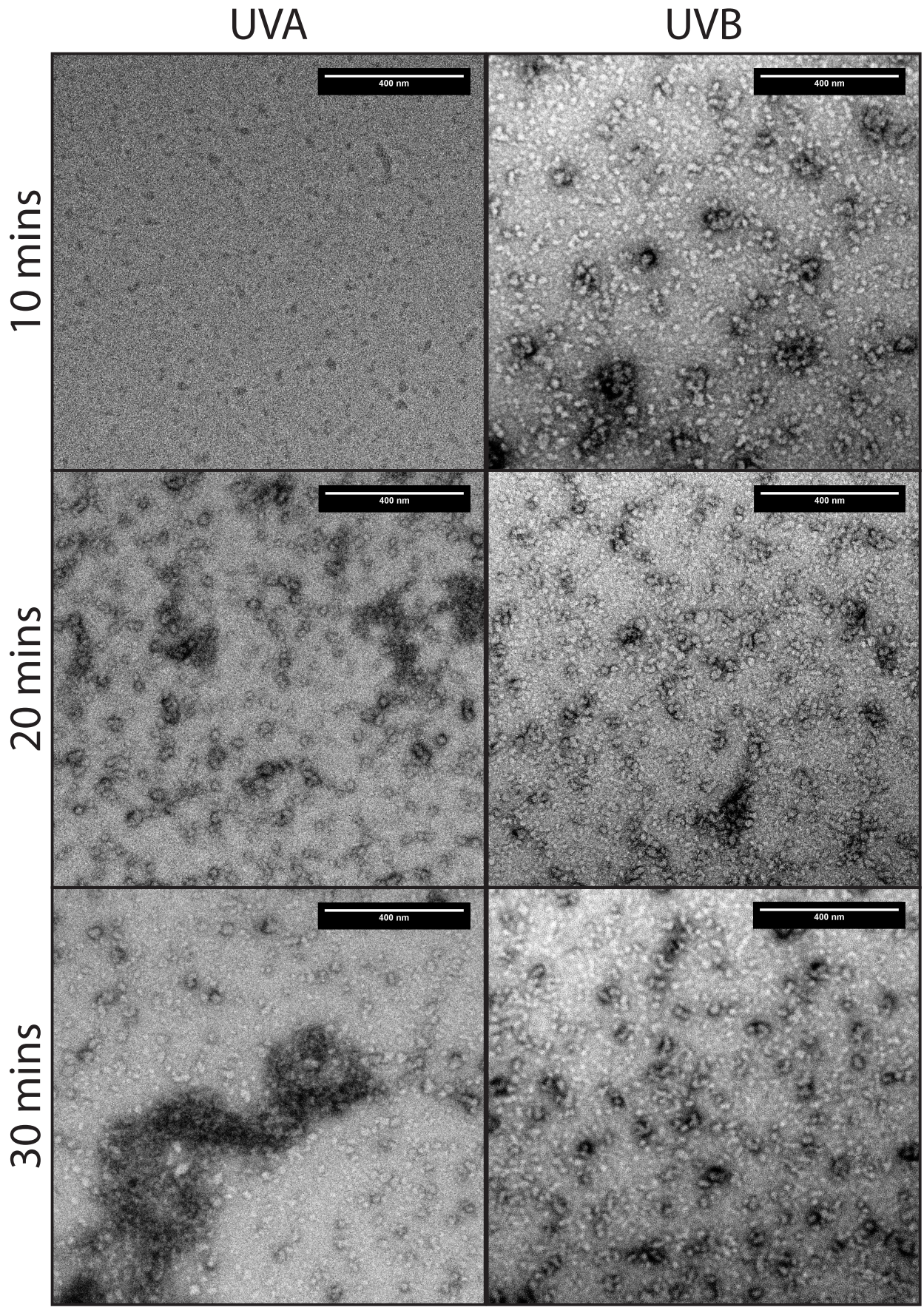

Figure A.3: γS-WT irradiated using UVA or UVB radiation for 10 (0.5 kJ/cm^2, 34.8 J/cm^2), 20 (1.1 kJ/cm^2, 69.6 J/cm^2), and 30 minutes (1.6 kJ/cm^2, 104.4 J/cm^2). Under both treatments, globular aggregates form and these constituents associate to generate larger aggre-

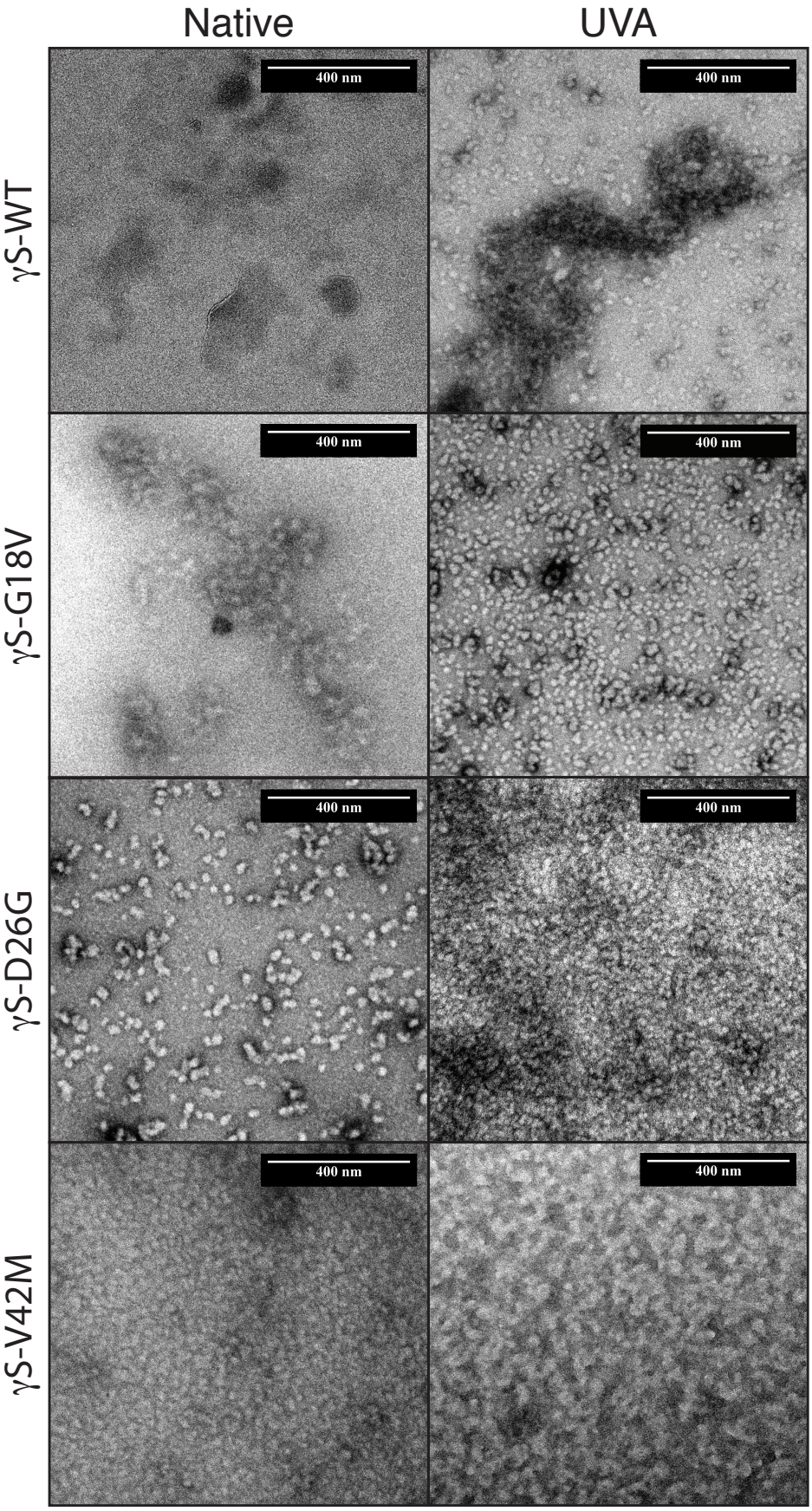

Figure A.4: Native aggregates resulting from cataractous mutations are highly similar in size and morphology to those formed via UVA photodamage.

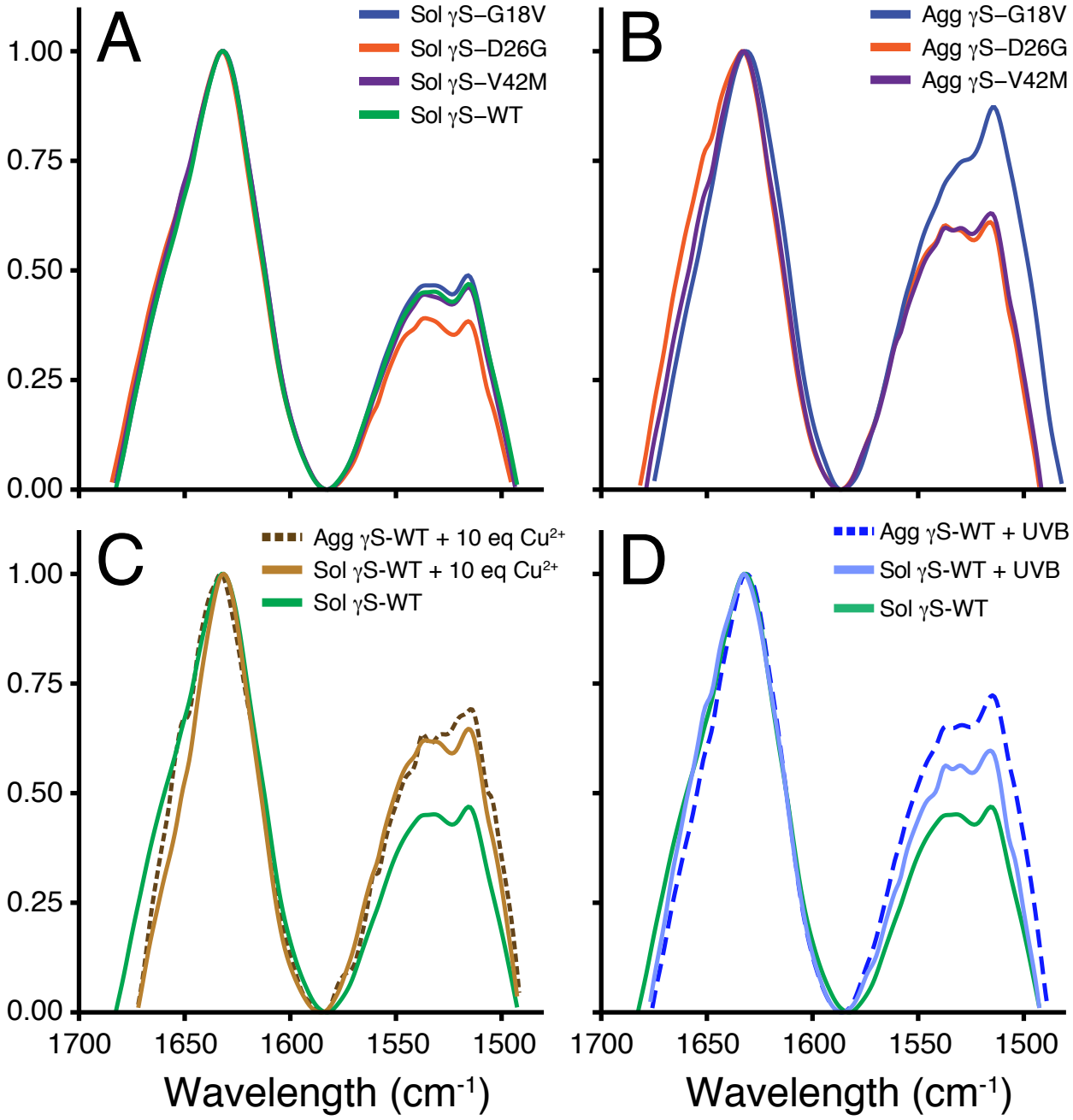

Figure A.5: The amide I and II band absorbances of

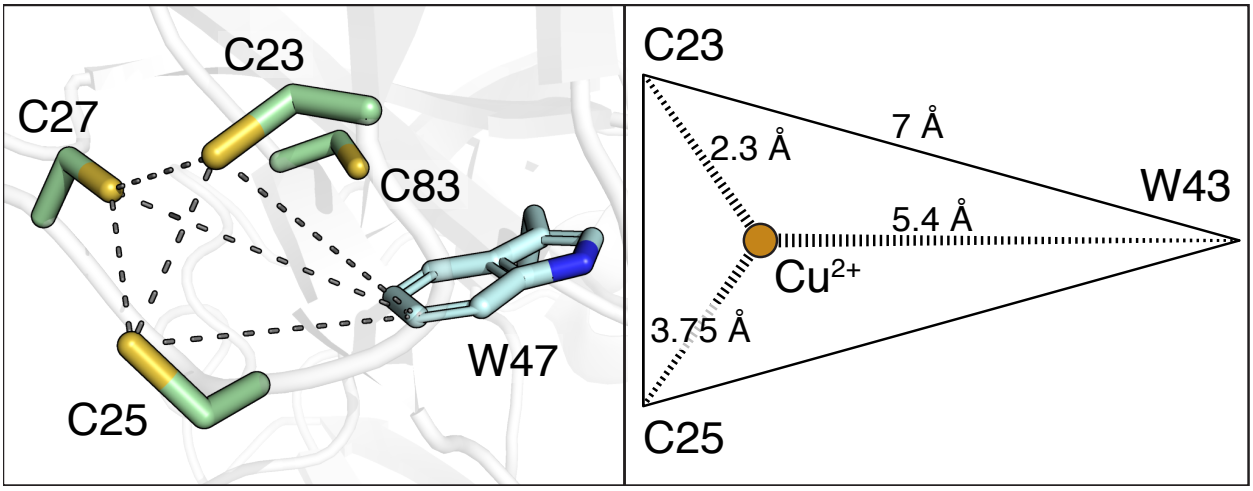

Figure A.6: The cysteine rich loop between the second and third β-strands of the N-terminal in γS-crystallin is a potential binding site for copper ions. Assuming a tetrahedral geometry with bond angles of 109.45° and binding distances of 2.3 $\mathring{A}$ for Cu^{2+} binding, the resulting interatomic distances of the C23, C25, and C27 sulfurs are 3.75 $\mathring{A}$. Imparting these distances on the γ-crystallin structure (PDBID: 2M3T[85]) yields symmetric 7 $\mathring{A}$ distances to the C6 atom of W43. The resulting distance between the copper ion and $W43_{C6}$, assuming coordination of the ion in a concave manner, generates a 5.4 $\mathring{A}$ distance.

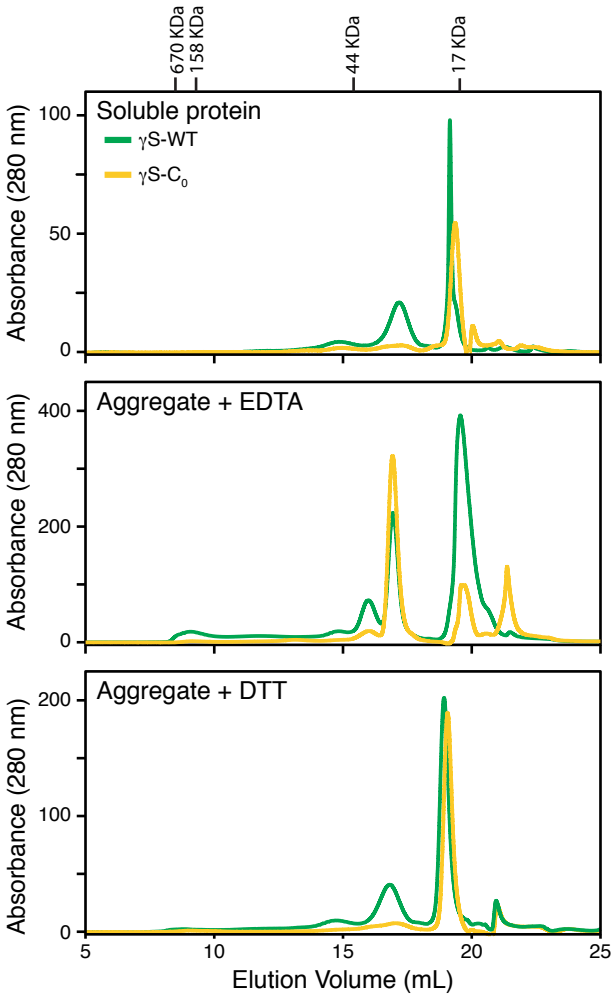

Figure A.7: Analytical SEC measurements of γS-WT and γS-C_0 collected separately following Cu^{2+} treatment. All samples were treated with EDTA and DTT after collection, prior to measurement.

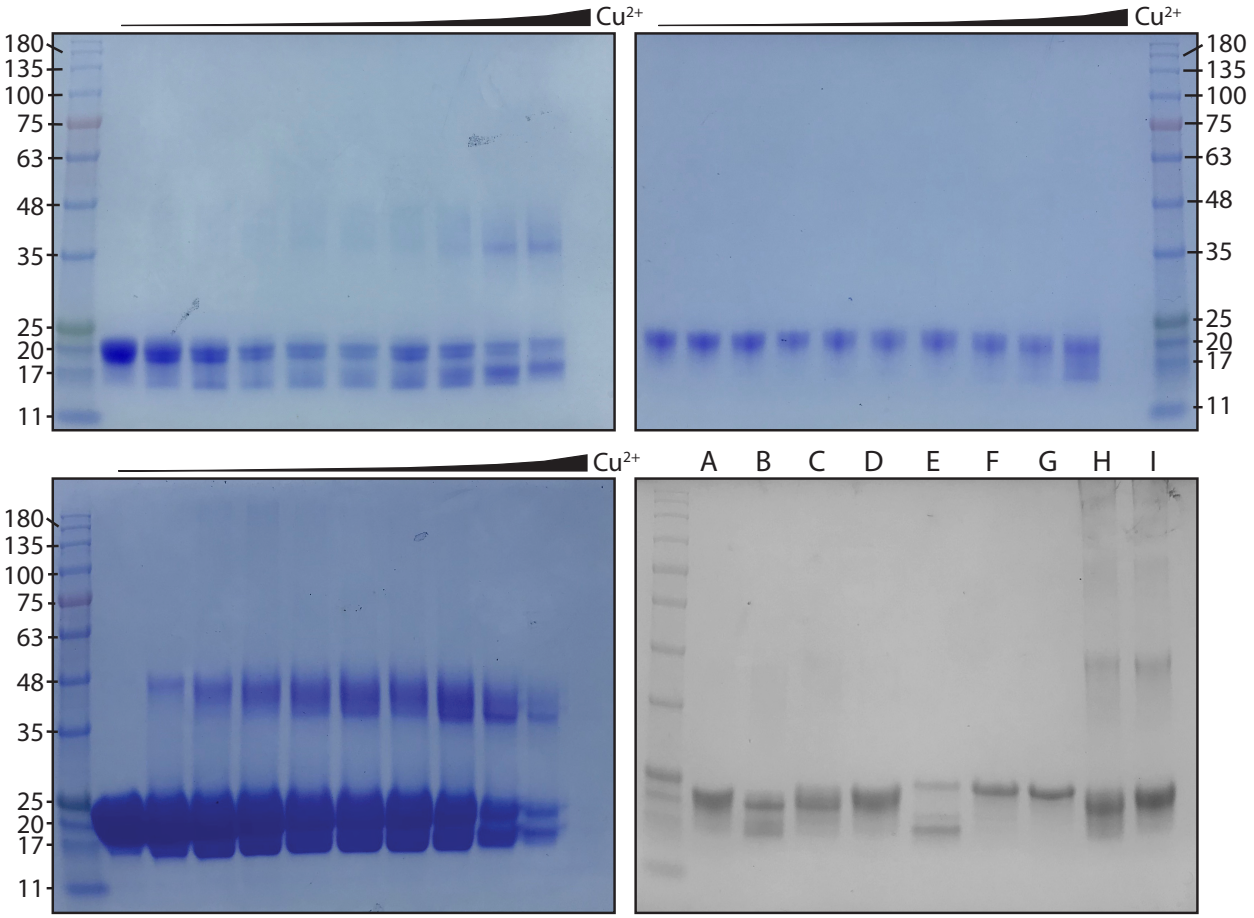

Figure A.8: SDS-PAGE analysis of γS-crystallin. (Top left) Soluble γS-WT after incubation with 0, 0.1, 0.2, 0.4, 0.6, 0.8, 1, 1.5, 2, 3, and 5 equiv of Cu^{2+}. Each sample contained equal protein concentrations, with the exception of the 5 equivalents sample which contained trace soluble protein. (Top right) Soluble γS-WT after incubation with 0, 0.1, 0.2, 0.4, 0.6, 0.8, 1, 1.5, 2, 3, and 5 equiv of Cu^{2+} and reduction with BME. Each sample contained equal protein concentrations, with the exception of the 5 equivalents sample which contained trace soluble protein. (Bottom left) Soluble γS-WT after incubation with 0, 0.1, 0.2, 0.4, 0.6, 0.8, 1, 1.5, 2, 3, and 5 equiv of Cu^{2+}. The samples were prepared with equal volumes of the remaining soluble protein such that the observed loss of protein is representative of increased aggregation. (Bottom right) A: γS-WT, B-D: γS-WT treated 1 equiv Cu^{2+} alone (B), with EDTA (C), or with EDTA and BME (D), E-G: γS-C_0 treated 1 equiv Cu^{2+} alone (E), with EDTA (F), or with EDTA and BME (G), H: soluble UV-B treated γS, I: soluble UV-B treated γS with BME.

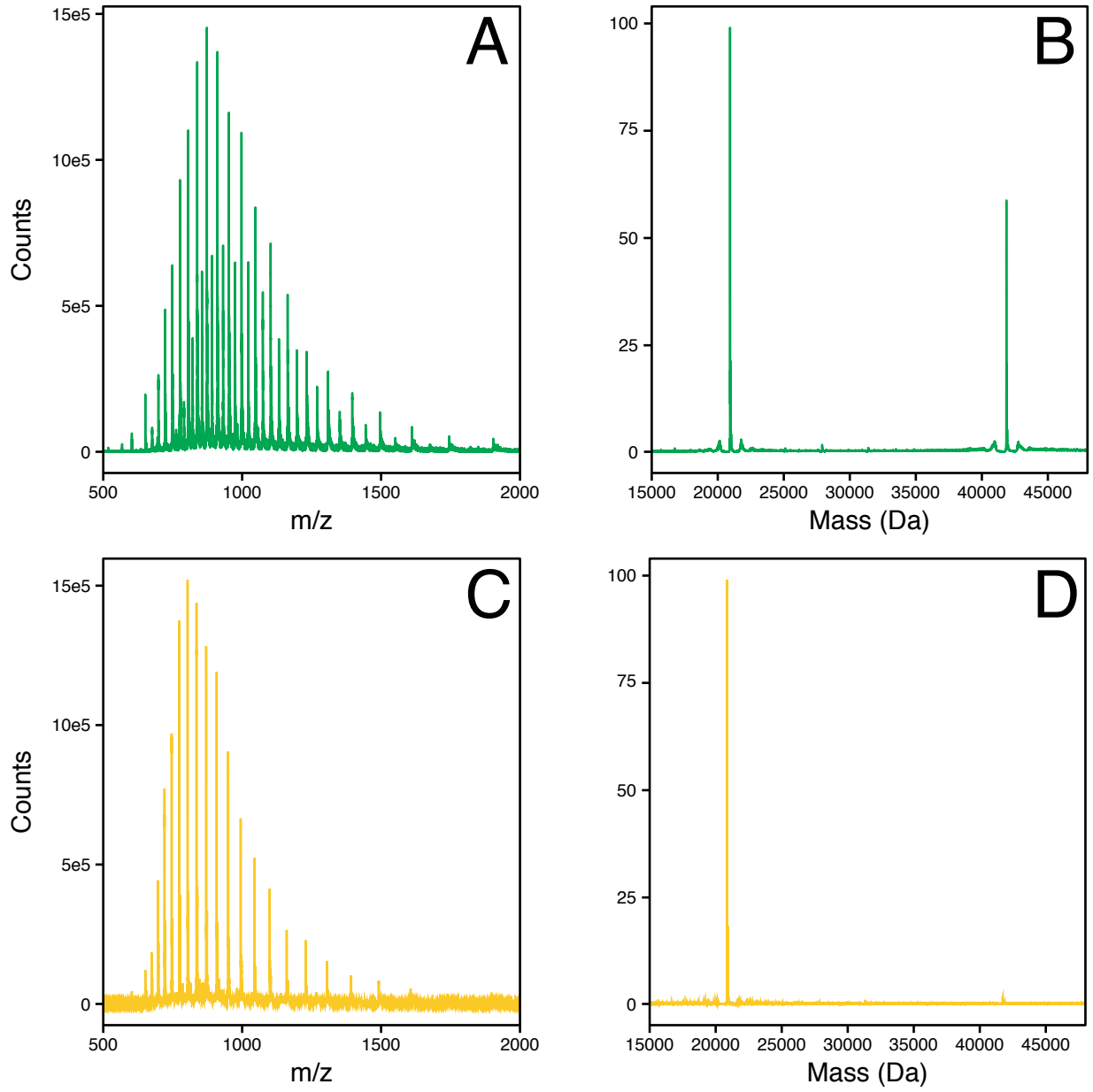

Figure A.9: The spectra and reconstructed masses of γS-WT (A, B) and γS-C_0 (C,D) taken for the soluble fractions following incubation with 2 equivalents of Cu^{2+}. Dimeric species are evidenced as a doubly charge species in the raw mass spectrum of γS-WT and the resulting mass reconstruction. In contrast, minimal levels of dimer are observed for γS-C_0.

Appendix D

4: Supplementary material for Multiple Aggregation Pathways in Human γS-Crystallin and Its Aggregation-Prone G18V Variant.

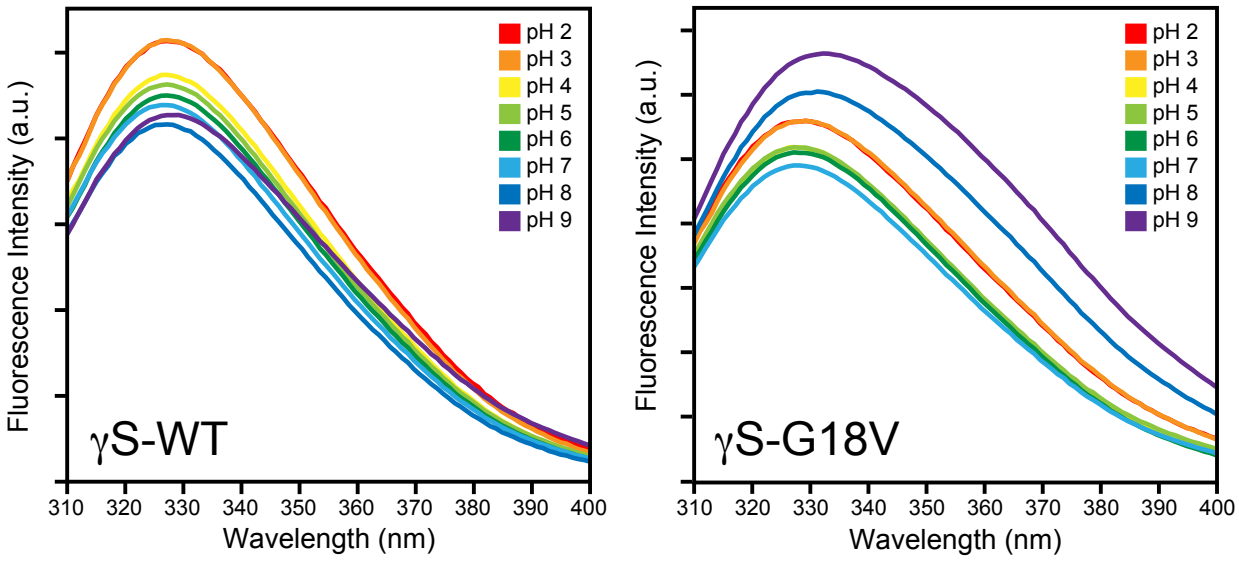

Figure A.1: Trp Fluorescence of γS-WT (left panel) and γS-G18V (right panel) for a range of pH values. Basic conditions result in both red shifting and reduced fluorescence quenching. The total fluorescence in both proteins decreases from acidic to neutral conditions. The largest red shifting of γS-G18V Trp fluorescence occurs under basic conditions, while smaller red shifts occur at pH 2 and 3. The Trp fluorescence of γS-G18V is significantly greater at pH 8 and 9 than under any other conditions.

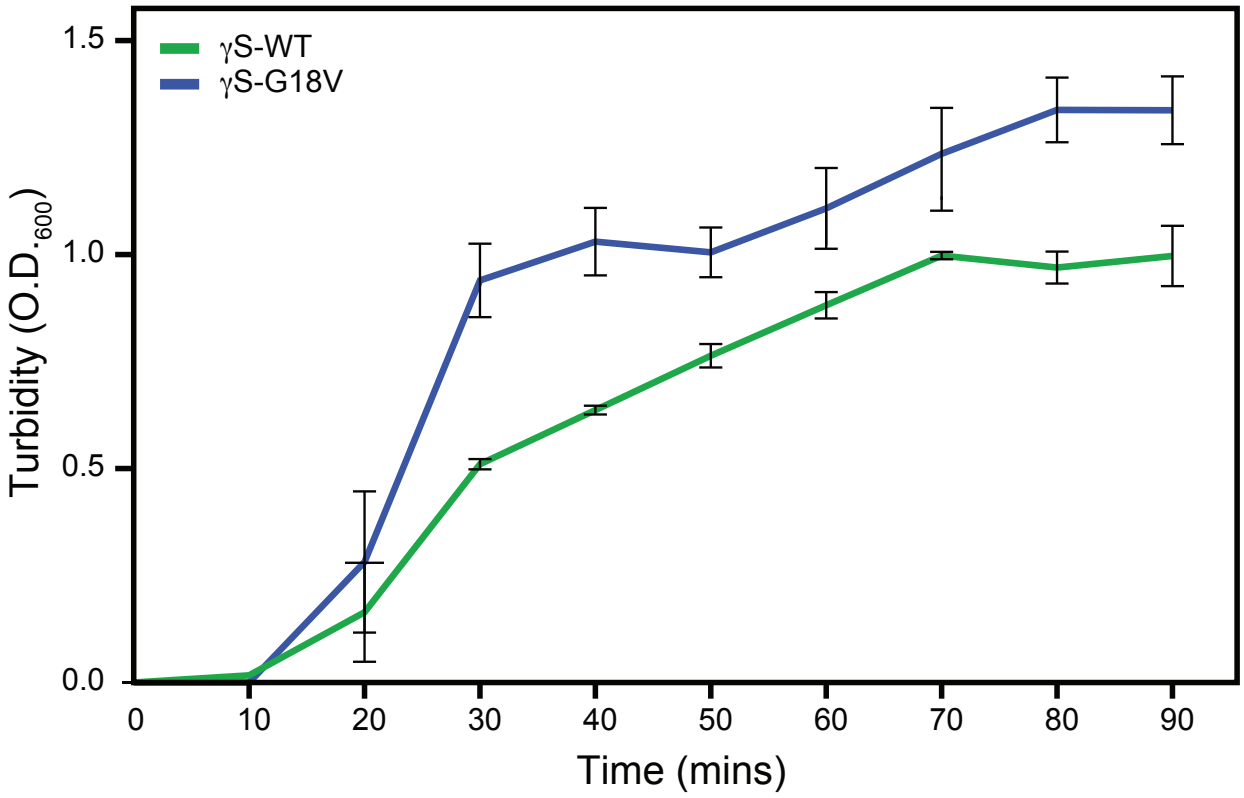

Figure A.2: Turbidity measurements for UV-irradiated samples of γS-WT (green) and γS-G18V (blue) (6 mg/mL concentration, pH 7). The solution temperature was held between 22 °C and 24 °C to prevent thermal aggregation. γS-G18V is consistently more turbid than γS-WT, with both proteins displaying the greatest increase aggregation between 10 and 30 minutes of exposure.